DISS. ETH NO. 30840

INTERFEROMETRIC AND POLARIMETRIC SAR MEASUREMENTS FOR SNOW WATER EQUIVALENT ESTIMATION

A thesis submitted to attain the degree of

DOCTOR OF SCIENCES
(Dr. sc. ETH Zurich)

presented by

KRISTINA BELINSKA
M.Sc. Physics, University of Bremen

born on 11.12.1994

accepted on the recommendation of

Prof. Dr. Irena Hajnsek
Dr. Juha Lemmetyinen
Dr. Georg Fischer
Prof. Dr. Laurent Ferro-Famil
Prof. Dr. Matthias Braun
Prof. Dr. Helmut Rott

2025

Abstract

Snow is an essential variable in climate models as snow cover on the land surface affects the climate of the Earth. Moreover, it is an important input for hydrological models since estimates on the amount of water stored within the snow pack are required to accurately predict runoff and thus enable water resource planning and flood forecasting. Increasing temperatures are affecting the snow cover, which has an important impact on ecology, economy and society. Thus, accurately estimating snow properties is a current scientific question of high relevance.

A parameter which can be used to describe the snow pack is the Snow Water Equivalent (SWE). SWE describes the amount of liquid water stored in a snow pack and is the depth of water that is obtained when the snow pack melts completely.

Remote sensing of the Earth's surface offers the possibility to continuously monitor large snow-covered areas at high temporal resolution. In particular, Synthetic Aperture Radar (SAR) is able to acquire data at a spatial resolution on the meter-scale and is almost independent from weather and illumination conditions. Moreover, the SAR signal is sensitive to snow properties, as it is capable of penetrating the snowpack. Differential Interferometric SAR (DInSAR) is a promising tool for the retrieval of snow properties, as the DInSAR phase between two repeat-pass complex SAR images can be directly related to the SWE change between both measurements. Even though this method can potentially achieve accurate results, it still has some limitations affecting its performance. One important issue are phase wraps of the interferometric phase. As a consequence, only a limited range of SWE change values can be retrieved unambiguously.

The goal of this thesis is the improvement of the DInSAR SWE change retrieval by exploiting the additional information content provided by multifrequency and polarimetric SAR data.

The first part of this work focuses on the analysis of the performance of spaceborne SAR datasets in terms of their suitability for the retrieval of SWE changes based on an existing DInSAR algorithm. The analysis includes the investigations of datasets in X-, C- and L-band from the spaceborne SAR missions TanDEM-X, Sentinel-1 and ALOS-2. It can be highlighted, that one limitation of the DInSAR SWE retrieval results from phase wraps of the interferometric phase when the SWE change between the SAR acquisitions exceeds a frequency dependent threshold. This threshold is lower for higher frequencies, which is why they are particularly affected by phase wraps. A possibility to solve the phase wraps is presented by using ground-based measurements of SWE. Furthermore, a multifrequency approach is investigated, which utilizes SWE change estimates from different frequencies to correct for missing phase cycles. Both approaches increase the accuracy of the SWE change retrieval. While the former achieves the highest accuracy, the latter has the advantage that it does not depend on ground measurements and is thus more suitable for large-scale analyses.

In the second part of this thesis, the aim is to include polarimetric information in the DInSAR SWE change retrieval. For this investigation, polarimetric airborne SAR data is used. An established model, which can relate the Copolar Phase Difference (CPD) between the horizontal and vertical channel to the snow depth, is applied with the goal to derive DInSAR SWE change estimates with a phase cycle correction based on the CPD change between two observations. It can be observed that even though some limitations affect the phase wraps correction, such as required assumptions on snow density and anisotropy, the overall accuracy can be increased compared to no phase wrap correction.

The last contribution of this thesis proposes to combine DInSAR and PolSAR observables into a unified Differential Polarimetric InSAR (DPolInSAR) approach to jointly exploit the information delivered by both. For that, a theoretical framework is established to model temporal polarimetric coherences for different snow depth and anisotropy changes. The effect on the phase and coherence region extent is analyzed for different snow changes. This study revealed that a snow depth change has a high impact on the absolute phase, while an anisotropy change mainly increases the phase diversity of different polarization states. Furthermore, the DPolInSAR model is used to estimate snow changes from the airborne SAR measurements by retrieving the parameters for snow depth, density, and anisotropy, which minimize the difference between measured and modeled coherences for different polarization states. The results improve compared to the single polarization DInSAR SWE change retrieval, demonstrating the potential of exploiting the information of different polarization states.

Zusammenfassung

Schnee ist eine essentielle Variable in Klimamodellen, da die Schneebedeckung auf der Landoberfläche das Klima auf der Erde beeinflusst. Außerdem ist Schnee ein wichtiger Inputparameter für hydrologische Modelle, da Schätzungen über die Wassermenge, die im Schnee gespeichert ist, erforderlich sind, um den Abfluss genau vorherzusagen und so die Planung von Wasserressourcen und die Vorhersage von Überschwemmungen zu ermöglichen. Steigende Temperaturen im Zuge der globalen Erwärmung haben einen Einfluss auf den Schnee und in Folge dessen erhebliche Auswirkungen auf die Ökologie, Wirtschaft und Gesellschaft. Daher ist die genaue Bestimmung von Schneeparametern eine aktuelle und relevante Forschungsfrage.

Ein Parameter, der zur Beschreibung von Schnee verwendet werden kann, ist das Schneewasseräquivalent (Snow Water Equivalent, SWE). SWE beschreibt die Menge an flüssigem Wasser, die in einer Schneedecke gespeichert ist, und ist somit die Höhe der Wassersäule, die sich ergibt, wenn die Schneedecke vollständig schmilzt.

Fernerkundung der Erdoberfläche ermöglicht es, kontinuierlich und großflächig schneebedeckte Gebiete mit einer hohen zeitlichen Auflösung aufzunehmen. Insbesondere Radar mit synthetischer Apertur (Synthetic Aperture Radar, SAR) ist in der Lage, Daten mit einer räumlichen Auflösung im Meterbereich zu erfassen und ist nahezu unabhängig von Wetter- und Beleuchtungsbedingungen. Außerdem besitzen SAR-Signale eine Sensitivität gegenüber Schneeeigenschaften, da diese in die Schneedecke eindringen können. Differentielles interferometrisches SAR (DInSAR) ist eine vielversprechende Methode für die Ermittlung von Schneeparametern, da die DInSAR-Phase zwischen zwei zu unterschiedlichen Zeitpunkten aufgenommen komplexen SAR-Bildern direkt mit der SWE-Änderung zwischen den beiden Messungen in Verbindung gebracht werden kann. Mit dieser Methode können präzise SWE-Änderungen bestimmt werden. Es gibt jedoch einige Einschränkungen, die die Genauigkeit dieser Methode beeinträchtigen. Eine davon sind Phase-Wraps der interferometrischen Phase. Diese treten auf, wenn die SWE-Änderung einen frequenzabhängigen Schwellenwert überschreitet. Infolgedessen kann nur ein begrenzter Bereich von SWE-Änderungen eindeutig bestimmt werden.

Das Ziel dieser Arbeit ist die Verbesserung der DInSAR SWE-Änderungsbestimmung durch die Nutzung von multifrequenten und polarimetrischen SAR-Daten.

Der erste Teil der Arbeit beschäftigt sich mit der Analyse von weltraumgestützten SAR-Datensätzen im Hinblick auf ihre Eignung zur Bestimmung von SWE-Änderungen mit einer bestehenden DInSAR-Methode. Die Analyse umfasst die Untersuchung von Datensätzen im X-, C- und L-Band aus den weltraumgestützten SAR-Missionen TanDEM-X, Sentinel-1 und ALOS-2. Die Untersuchungen bestätigen, dass Phase-Wraps eine wesentliche Einschränkung bei der DInSAR-SWE-Bestimmung sind und dass der Schwellenwert für deren Auftreten

frequenzabhängig ist. Er liegt bei höheren Frequenzen niedriger, weshalb diese besonders stark von Phase-Wraps betroffen sind. Es wird eine Möglichkeit vorgestellt, Phase-Wraps mit Hilfe von bodengestützten SWE-Messungen zu korrigieren. Darüber hinaus wird ein Multifrequenz-Ansatz präsentiert, der die berechneten SWE-Änderungen von verschiedenen Frequenzen verwendet, um fehlende Phasenzyklen zu korrigieren. Beide Ansätze erhöhen die Genauigkeit der ermittelten SWE-Änderungen. Während der erste Ansatz eine höhere Genauigkeit erzielt, hat der zweite den Vorteil, dass er nicht von Bodenmessungen abhängt und daher für großflächige Analysen besser geeignet ist.

Der zweite Teil dieser Arbeit widmet sich der Einbeziehung polarimetrischer SAR (PolSAR) Informationen in die DInSAR SWE-Änderungsbestimmung. Für diese Analyse werden polarimetrische flugzeuggestützte SAR-Daten verwendet. Es wird ein Modell verwendet, welches die copolare Phasendifferenz (Copolar Phase Difference, CPD) zwischen dem horizontal und vertikal polarisiertem SAR-Signal mit der Schneehöhe in Verbindung bringen kann. Dieses wird angewendet um eine Phasenzykluskorrektur auf der Grundlage der CPD-Änderung zwischen zwei Beobachtungen durchzuführen. Trotz einiger Einschränkungen, wie etwa erforderlicher Annahmen zur Schneedichte und Anisotropie, lässt sich feststellen, dass sich die Gesamtgenauigkeit im Vergleich zu einer unkorrigierten Phase erhöht.

Im letzten Teil dieser Arbeit wird vorgeschlagen, DInSAR- und PolSAR-Daten zu einem differentiellen polarimetrischen interferometrischen SAR (DPolInSAR) Ansatz zu kombinieren, um den von beiden Messungen gelieferten Informationsgehalt zu nutzen. Zu diesem Zweck wird eine theoretische Formulierung vorgestellt, um die DPolInSAR-Kohärenzen verschiedener Polarisationszustände für unterschiedliche Schneehöhen- und Anisotropieänderungen zu modellieren. Die Auswirkungen verschiedener Schneeänderungen auf die Phase und die Ausdehnung der Kohärenzregion werden analysiert. So hat eine Änderung der Schneehöhe einen großen Einfluss auf die absolute Phase, während eine Anisotropieänderung vor allem die Phasendiversität der verschiedenen Polarisationszustände erhöht. Darüber hinaus wird das DPolInSAR-Modell verwendet, um Schneeänderungen von flugzeuggestützten SAR-Messungen zu berechnen, indem die Parameter für Schneetiefe, Schneedichte und Anisotropie ermittelt werden, die den Unterschied zwischen gemessenen und modellierten Kohärenzen minimieren. Die Ergebnisse der SWE-Änderungen verbessern sich im Vergleich zum DInSAR-Ansatz mit nur einer Polarisation und zeigen somit das Potenzial der Nutzung des Informationsgehalts verschiedener Polarisationszustände.

Acknowledgements

I would to thank everyone who supported me during my PhD journey!

First of all, I would like to thank Irena to give me the opportunity to pursue my PhD in her group. I really appreciate all the discussions, her supervision and guidance. I am very thankful that I had the opportunity to travel to many conferences in different countries and participate in field campaigns.

I also want to thank Gerhard Krieger and Alberto Moreira for enabling me to work in the Radar Concepts department of the Microwaves and Radar Institute at DLR.

I would like to thank Helmut Rott, Juha Lemmetyinen, Laurent Ferro-Famil and Matthias Braun for agreeing to be co-examiners of this thesis.

I want to thank Giuseppe for being a great supervisor in the beginning of my PhD. I thank Georg for taking over. Thanks for all the discussions, suggestions and for motivating me in challenging times. I really appreciate all the time you invested to read all my abstracts and papers.

Thanks to Kostas for all his ideas and for taking time to review my paper.

I would like to thank all members of the PolInSAR and Information retrieval group: Alessandro, Ben, Islam, Jun Su, Klemens, Lea, Matteo, Nikita, Noelia, Paloma, Patricia, Roman, Thomas and all the former members I met during my time at DLR. Thanks for the nice lunch breaks, dinners, conferences and trips.

I am thankful that I had the opportunity to collect SWE data for two airborne SAR campaigns. I would like to thank all the people that participated in the planning of the campaigns. Big thanks to Georg, Patricia, Andi, Philipp, Jorit, Celia, and Matthias. Without you, the measurements wouldn’t have been possible.

I want to thank my parents, Alla and Gevork, my family, and my friends for all their support and Jonas, for always being there for me.

Contents

List of Abbreviations

ALOS-2	Advanced Land Observing Satellite, L-band, JAXA
ASAR	Advanced Synthetic Aperture Radar, C-band, ESA
C-band	Wavelength between 4 cm and 8 cm
CPD	Copolar Phase Difference
DEM	Digital Elevation Model
DLR	Deutsches Zentrum für Luft- und Raumfahrt (German Aerospace Center)
DInSAR	Differential Synthetic Aperture Radar Interferometry
DPolInSAR	Differential Polarimetric Synthetic Aperture Radar Interferometry
ERS	European Remote-Sensing Satellite, C-band, ESA
F-SAR	Airborne SAR system, DLR
HH	Horizontal receive, Horizontal transmit
HV	Horizontal receive, Vertical transmit
IOA	Intensive Observation Area
InSAR	Synthetic Aperture Radar Interferometry
Ku-band	Wavelength between 1.7 cm and 2.5 cm
L-band	Wavelength between 15 cm and 30 cm
LiDAR	Light Detection and Ranging
LWC	Liquid Water Content
NISAR	NASA-ISRO SAR, L-band and S-band, NASA and ISRO
PAZ	SAR satellite, X-band, Hisdesat
PolSAR	Polarimetric Synthetic Aperture Radar
PolInSAR	Polarimetric Synthetic Aperture Radar Interferometry
Radar	Radio Detection and Ranging
RMSE	Root Mean Square Error
ROSE-L	Radar Observing System for Europe in L-band, ESA
S-band	Wavelength between 8 cm and 15 cm
SAR	Synthetic Aperture Radar
Sentinel-1	SAR satellite, C-band, ESA
SNR	Signal to Noise Ratio
SWE	Snow Water Equivalent
TanDEM-X	SAR satellite, X-band, DLR
TAXI	TanDEM-X interferometric Processor
TerraSAR-X	SAR satellite, X-band, DLR
UAVSAR	Uninhabited Aerial Vehicle Synthetic Aperture Radar, NASA
VH	Vertical receive, Horizontal transmit
VV	Vertical receive, Vertical transmit
X-band	Wavelength between 2.5 cm and 4 cm

List of Symbols

α	Alpha angle
γ	Complex coherence
$\gamma(\vec{w})$	Complex DPolInSAR coherence at polarization state $\vec{w}$
γ_{CPD}	Complex polarimetric coherence
γ_{Inf}	Complex interferometric coherence
γ_{SNR}	Noise decorrelation
γ_t	Temporal decorrelation
ε	Permittivity of snow
ε_{air}	Permittivity of air
$\varepsilon_{eff,i}$	Effective permittivity of dimension $i \in [x, y, z]$
$\varepsilon_{H \text{ or } V}$	Permittivity of horizontal or vertical polarization
ε_{ice}	Permittivity of ice
Θ	Incidence angle
$\kappa_{H \text{ or } V}$	Wavenumber of the horizontal or vertical polarization
λ	Wavelength
ρ	Density of snow
ρ_w	Density of water
σ_Φ	Phase Noise
σ_s	Standard deviation snow depth
Φ_{CPD}	Copolar phase difference
$\Phi_{HH \text{ or } VV}$	Phase of the horizontal or vertical polarization
Φ_{scat}	Stochastic scattering phase
$\Delta\Phi$	Phase difference
$\Delta\Phi_{CPD}$	Copolar phase difference change
$\Delta\Phi_{Inf}$	Interferometric phase difference
$\Delta\Phi_S$	Interferometric phase difference induced by snow
$[\Omega_L]$	DPolInSAR matrix in lexicographic basis
$[\Omega_{0L}]$	DPolInSAR matrix in lexicographic basis of scattering mechanism below the snow
a_i	Dimension $i \in [x, y, z]$ of the ice grains
A	Anisotropy
$[C]$	Polarimetric covariance matrix
$[C_0]$	Polarimetric covariance matrix of scattering mechanism below the snow
f	Ice volume fraction
k	Wavenumber
$\overrightarrow{k_L}$	Scattering vector in lexicographic basis

$\overrightarrow{k_{0L}}$	Scattering vector in lexicographic basis of scattering mechanism below the snow
$\overrightarrow{k_P}$	Scattering vector in Pauli basis
n_{air}	Refractive index of air
$n_{H \text{ or } V}$	Refractive index of the horizontal or vertical polarization
n_i	Refractive index of dimension $i \in [x, y, z]$
N	Number of looks
N_i	Depolarization factor of dimension $i \in [x, y, z]$
$[P_2]$	Propagation matrix
pdf	Probability density function
r	Path length in range direction
Δr	Path length difference in range direction
$RMSE_a$	Root Mean Square Error after phase wrap correction
$RMSE_b$	Root Mean Square Error before phase wrap correction
$RMSE_{rel}$	Relative Root Mean Square Error
s_{ij}	Scattering matrix element at polarization ij with $i, j \in [H, V]$
S	SAR acquisition
$[S]$	Scattering matrix
$[S_0]$	Scattering matrix of scattering mechanism below the snow
ΔSWE	Snow Water Equivalent change
ΔSWE_{CPD}	Polarimetric Snow Water Equivalent change estimate
$\Delta SWE_{HH \text{ or } VV}$	Snow Water Equivalent change using horizontal or vertical polarized radar waves
$[T]$	Polarimetric coherency matrix
$\vec{w}$	Polarization state
$\vec{w}_{HH \text{ or } VV}$	Polarization state at horizontal or vertical polarization
Z	Snow depth
ΔZ	Snow depth change
$(\cdot)^T$	Transpose
$(\cdot)^*$	Complex conjugate
$(\cdot)^+$	Complex conjugate transpose
$\langle \cdot \rangle$	Expectation value
$\lvert \cdot \rvert$	Magnitude

1 Introduction

1.1 Motivation and State of the Art

Around 50 percent of the land surface in the Northern hemisphere is covered with snow in midwinter [1]. The seasonal snow cover thus represents an important parameter in climate models [2] due to a variety of snow-related processes: The high reflectivity of snow leads to a high surface albedo. In combination with the fact that snow has a higher thermal emissivity than other natural surfaces, snow cover affects the energy budget of the Earth and thus the global climate [3]. Furthermore, seasonal snow cover also affects polar and alpine ecosystems by influencing environmental variables such as soil temperature and, in turn, the growth of vegetation [4]. Snow melt is a source of fresh water for over one billion people [5], [6] and is therefore an essential hydrological parameter. Hydrological models rely on information on the amount of water stored within the snow pack [7]. This is required to make runoff predictions [8] and forecast floods [9].

However, the current rise in temperatures [10] affects seasonal snowfall and snow melt and thus results in an alteration of runoff regimes, leading to an earlier runoff in spring or winter. This has consequences for areas in particular where the population relies on snowmelt for their water supply and water storage capabilities are limited [8]. Therefore, accurate measurements of snow parameters are vital for resource planning in, e.g. agriculture, transportation, and power generation.

A parameter that provides information on the snow pack is the Snow Water Equivalent (SWE). The SWE describes the amount of liquid water contained within the snow pack. Precise information on SWE can be obtained with ground measurements. This can be done either by manual measurements [11] or by automated measurement stations [12], [13]. However, manual measurements and ground stations are typically limited to small study areas and few locations. This is also exacerbated by the fact that snow covered areas are often characterized by harsh weather conditions and are located in remote regions with challenging access. The spatial interpolation of sparsely sampled in situ data allows for a wider coverage, but introduces significant uncertainties and a coarse spatial resolution.

Remote sensing offers the possibility to continuously monitor larger areas at high temporal and spatial resolutions. Particularly sensors operating at microwave frequencies can acquire measurements that are almost independent of weather and illumination conditions, making them suitable for cryosphere applications, as regions covered with snow are often affected by polar darkness and a high cloud coverage [14].

In this context, a widely used sensor type are passive microwave sensors. For the estimation of snow products like SWE, a link between the brightness temperature and the snow layer is established [15], [16], [17], [18], [19], [20]. There are global products available that can provide snow parameters on a daily basis [17], [18]. However, for snow with a depth of above 1 meter, a saturation effect of the signal can be observed [19]. Furthermore, the spatial resolution lies on the

kilometer-scale [20] so that these products are not accurate in complex terrain such as mountain ranges.

In comparison, active radar sensors like Synthetic Aperture Radars (SARs) have the advantage to be able to monitor the Earth at a high spatial resolution on a meter-scale [21], making it an important sensor for cryosphere applications. Active microwave signals are able to penetrate into dry snow [22], [23]. Therefore, they are sensitive to snow parameters and different techniques and algorithms have been developed to retrieve these from SAR data. There are methods which are based on radiative transfer models [24], [25]. However, these models require a priori information as input parameters. Other approaches also include information of polarimetric SAR (PolSAR) for the retrieval of snow properties [26], where the backscatter of two frequencies at two different polarizations are combined in a radiative transfer model.

It was shown that it is possible to relate the backscatter of the co and cross polarized channels in VV and VH to the snow depth and to establish an empirical relation [27], [28]. However, research on the underlying scattering mechanism and its impact is still ongoing with the goal to explain this empirical relation [29]. Another proposed technique to retrieve snow depth differences two digital elevation models (DEMs) at different times, but this method requires the presence of wet snow and suffers from the weak backscatter signal [30].

A promising approach has been proposed in [31] based on repeat-pass SAR measurements, which are measurements of the same location separated by a temporal baseline. The key observable of repeat-pass SAR is the interferometric phase, which is essentially the difference in travel time or path length of the microwave signals between the two acquisitions. The authors demonstrated that there is a relation between the interferometric phase between two SAR acquisitions and the SWE change between the measurements. Using C-band (wavelength $\lambda \approx 4 - 8\ cm$) European Remote-Sensing Satellite (ERS) data over a test site in Norway, the authors showed that the interferometric phase is affected by a snow change, yielding a height difference in DEMs. This was explained by the refraction of the radar waves inside the snow pack. The observation made and the relationship discovered between a SWE change and the interferometric phase is fundamental for this thesis. Hence, the state-of-the-art of research in this context shall be elaborated in more detail.

A tower-based radar in Finland with measurements in Ku ($\lambda \approx 1.7 - 2.5$ cm) and X-band ($\lambda \approx 2.5 - 4$ cm) was used in [32] to further exploit the relationship between SWE change and interferometric phase. The authors demonstrated an extension to the formulation found in [31] to make it valid for a wider span of densities. It was possible to reduce the effect of temporal decorrelation by acquiring a time series with a temporal baseline of 4 hours. The results had a high agreement with the validation data, showing the potential of the proposed method. However, phase wraps of the interferometric phase were observed, because it is only possible to measure the interferometric phase in a 2π interval. This phase wrap limitation was already mentioned in [31]. A recent tower-based experiment in Finland investigated the decorrelation of the interferometric measurements and the SWE retrieval for X-, C-, S- ($\lambda \approx 8 - 15$ cm) and L-band

($\lambda \approx 15 - 30$ cm). It was shown that shorter wavelengths experience faster decorrelation than longer wavelengths. The main reason for decorrelation is temperatures above zero, causing melting of the snow. However, a high precipitation intensity and wind can also be a cause for decorrelation, adversely affecting the results of the SWE change retrieval. It was shown that the SWE profiles could be estimated with the highest accuracy for long wavelengths and small temporal baselines, while the error increased for shorter wavelengths and longer temporal baselines [33].

To achieve a larger spatial coverage for the SWE change retrieval, repeat-pass airborne SAR measurements can be used. Recently, campaigns were conducted to test the SWE change retrieval, using for example the Uninhabited Aerial Vehicle SAR (UAVSAR) over a test site in North America [34], [35], [36], [37], [38]. The results in [34] showed the potential for the L-band SWE retrieval by qualitatively comparing the UAVSAR retrieval to Light Detection and Ranging (LiDAR) measurements. However, the authors also mentioned the unknown phase offset of the interferometric phase, which requires a reference phase. In [35] the retrieved SWE from the UAVSAR data shows accurate results, which depend on the timing of the measurements, the reference phase, and also the characteristics of the snowpack. The UAVSAR dataset was also applied to retrieve the SWE over a shallow prairie snow pack. It showed that the highest discrepancy between the InSAR and LiDAR SWE estimates are obtained for a high snow depth variability inside a resolution cell [36]. In [37] a reference phase was calculated based on the in situ data and the results were compared to a snow model, showing good results for areas with no snow melt and little vegetation. The UAVSAR data set was additionally validated using ground-penetrating radar and LiDAR measurements further demonstrating the potential of interferometric repeat-pass SAR for SWE retrieval. However, land cover was affecting the SWE change retrieval with lower SWE estimations over forested areas [38]. A different airborne SAR campaign using the DLR's F-SAR system was performed over a valley in the Austrian Alps in C- and L-band. The first analysis indicated good results for the SWE maps based on L-band measurements. For C-band, decorrelation during a bigger snow fall event was observed and the constraint of the 2π phase ambiguity, which has a higher impact on C-band compared to L-band, was mentioned [39]. Data acquired during this campaign will be also used in this thesis.

Spaceborne SAR measurements have also been utilized successfully to retrieve the SWE change between two acquisitions. Different frequencies were utilized for that purpose. Many studies have been performed using C-band sensors, such as [40], [41], [42], [43], [44], [45]. In [40], the temporal decorrelation due to snow changes inside the resolution cell, which may be caused by snow accumulation or a redistribution due to wind, was found to be a limitation. The C-band data measured with ERS proved to be affected by temporal decorrelation more than L-band data from an airborne sensor. The authors also mentioned the importance of having accurate DEM information, which is needed for phase calibration, as well as the more limited range of SWE change values that can be retrieved for C-band. In [41] Envisat ASAR data was used to retrieve the SWE over a mountainous area, which required the presence of dry snow. The authors in [42] utilized Sentinel-1 data and removed the atmospheric phase contribution with a numerical

weather model showing results with a high accuracy, but also described the limitation of this method which is due to the limited range of values which can be retrieved without phase unwrapping. Sentinel-1 data was used in [43] for SWE retrieval, where the authors modelled the snow density and SWE from interferometric data. This study relied on the assumptions that the snow is dry, and, accordingly the restrictions due to the presence of wet snow were mentioned. In [44], in addition to the interferometric SWE change retrieval, also the topographic variation of the scene was taken into account to estimate the absolute SWE change. Furthermore, in [45] it was demonstrated using Sentinel-1 C-band data that it is essential to correct for the atmospheric phase delay. A high correlation with in situ data was achieved but it was also shown that strong decorrelation contributed to a lower performance of the SWE change retrieval. In addition to the already mentioned decorrelation sources it was demonstrated that changes in the permittivity of dry snow can lead to decorrelation [46]. Spaceborne Advanced Land Observing Satellite (ALOS-2) L-band data was utilized in [47], where also the backscattering contribution from the roughness of the snow surface was taken into account, which contributed to 4% of the SWE retrieval error. Here a known reference phase was used to calibrate the interferometric phase. The results for the ALOS-2 SWE change retrieval were also compared to modeled SWE changes to increase the amount of validation data. The SWE change estimates had a high accuracy, which, however, decreased for forested areas when the temperature was close to zero degrees. It was assumed that these temperatures resulted in a higher permittivity of the canopy. This, in turn, led to a higher contribution to the interferometric phase, which may have caused errors in the retrieval [48].

In contrast to polarimetric backscatter measurements, it is also possible to correlate the Copolar Phase Difference (CPD) to the snow depth [49], [50]. It was shown in [49] using TerraSAR-X and TanDEM-X X-band data that the CPD increases by around 5-15 degrees per 10 cm of fresh snow, due to its anisotropic structure. When no snow accumulation occurred, the CPD started to decrease by 3-7 degrees per 11 days, due to snow metamorphism. In [50], also ground-based radar measurements were used and similar trends as for the TerraSAR-X measurements were observed. A model has been proposed to relate the CPD to the snow properties which is based on the different dielectric properties for vertically and horizontally polarized radar waves. The CPD depends on the density, depth and anisotropy of the snow pack and can therefore be used to invert the snow depth or SWE [49], [50]. The link between CPD and fresh snow depth was also observed in [51] and [52]. The model relating the CPD to the snow depth was recently applied using TanDEM-X data in the Himalayas, showing that in such mountainous terrain the multilook window size plays a role. As input parameters, the density from the average of ground stations and an assumed anisotropy were required [53]. Another study applying the CPD model to retrieve SWE using TerraSAR-X data was presented in [54], showing the best accuracy in dry snow. The CPD model cannot only be applied to fresh snow, but also for the retrieval of the firn thickness when negative anisotropies are used, for example using L-band data in [55]. The CPD is more robust to phase wraps than the interferometric phase. However, using radar measurements at short wavelengths, such as Ku-band, phase wraps of the CPD can be observed [56]. These studies show that information on the snow depth can be derived from the CPD.

In conclusion, using the interferometric phase, highly accurate SWE change values can potentially be achieved. However, temporal decorrelation, the need of a reference phase, and the fact that only a limited range of SWE change values can be retrieved unambiguously, are all factors which limit the potential of using the interferometric phase to retrieve SWE change values. Particularly the last restriction will be the focus of this thesis. Potential solutions for phase wraps lie, firstly, in the inclusion of multiple frequencies for SWE change retrieval, and secondly, in the use of polarimetric information and the CPD. Both approaches will be investigated in this thesis. For that purpose, the following chapter introduces the technical background of SAR remote sensing and the methods that will be used in this study, followed by the research objectives and questions.

1.2 Background on SAR

The acronym Radar stands for Radio detection and ranging. Radar sensors are used to detect and locate objects by emitting energy in the microwave frequency range of the electromagnetic spectrum. Imaging radars are able to generate two-dimensional images of a scene [57]. SARs are side looking imaging radars that are located on moving platforms. Being active radar systems, SARs emit an electromagnetic wave and then receive a backscattered signal. The time between the transmitted and received signal can be related to the locations of the scatterers [21]. The distance to the scatterer is measured in range direction and the direction of the movement of the platform is the azimuth direction [58].

Special processing of the signals allows to form a synthetic aperture that is longer than the real antenna. This has the advantage of increasing the spatial resolution [59], making SARs important sensors for various applications in Earth observation [60].

SARs measure the complex reflectivity of the surface, meaning a complex signal that contains amplitude and phase information [58]. How an emitted radar wave interacts with a scatterer depends, among other factors, on the frequency of the wave. Thus, SAR sensors emitting waves in different frequency spectra have different application foci. Typical frequency bands for the radar signals used in cryosphere contexts, which will be also used in this thesis, are displayed in Table I [57].

The received signal also depends on the underlying scatterers. Using the amplitude, backscatter information of the scene can be obtained [58]. The backscatter intensity can be used to characterize surfaces, for example for wet snow mapping [61]. The phase information of a single SAR image is characterized by a noise-like signal due to speckle. The effect arises from the fact that a resolution cell contains a superposition of distributed scatterers, each contributing

Table I
Frequency Bands

Band	X	C	L
Frequency [GHz]	12–8	8–4	2–1
Wavelength [cm]	2.5–4	4–8	15–30

to the phase term. The phase of the scatterers located in different parts of the resolution cell may be very different and is independent of the amplitude signal [58]. Nevertheless, there are techniques which can be used in order to still exploit the phase information of the SAR image, by using interferometric and polarimetric phase differences. These techniques will be described in the following sections, as the phase is an essential observable in this thesis.

1.2.1 Interferometric SAR

Differential SAR Interferometry (DInSAR) is a SAR technique that requires two complex SAR images that are separated by a temporal baseline, with the goal to measure temporal changes using the phase information of an electromagnetic wave [62]. An example is displayed in Fig. 1. At the time t_1, the SAR sensor is measuring a pixel located in the scene after traveling the path r_1. After a temporal baseline $\Delta t = t_2 - t_1$ the same location is measured again with the second acquisition. However, the distance has now changed to r_2. The interferogram between the image S_1 and S_2 can be calculated with:

$$S_1 S_2^* = |S_1||S_2|\exp(i(\Phi_1 - \Phi_2)). \tag{1}$$

The phase of the acquired signal S_1 is given by:

$$\Phi_1 = \arg(S_1) = -\frac{4\pi}{\lambda} r_1 + \Phi_{scat,1}, \tag{2}$$

Where $\Phi_{scat,1}$ describes a stochastic scattering phase term for the first acquisitions. For the second image the corresponding phase is accordingly:

$$\Phi_2 = \arg(S_2) = -\frac{4\pi}{\lambda} r_2 + \Phi_{scat,2}. \tag{3}$$

The phase of a single SAR image cannot be used for information retrieval as it contains the stochastic phase term due to speckle. However, it can be assumed that if the measurements are acquired from the same location and the scatterers have not changed between the acquisitions, the stochastic term in the first and second acquisition agree with $\Phi_{scat,1} \approx \Phi_{scat,2}$. The interferometric phase for the measured pixel can be written as:

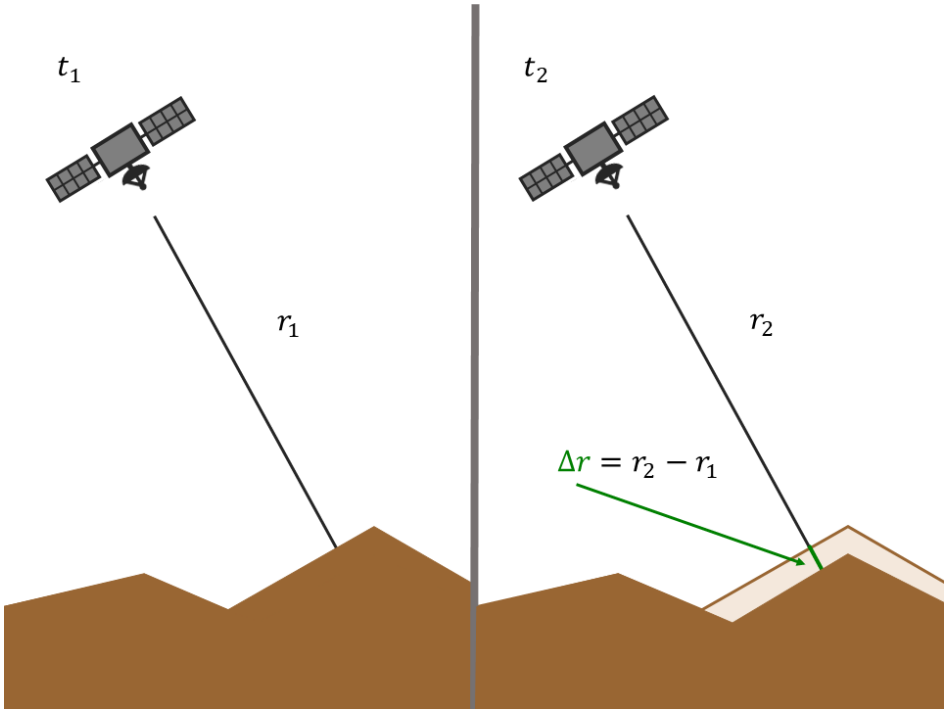

Fig. 1. Example of a repeat-pass interferometric measurement. (Left) The sensor is measuring the scatterer at the time t_1 with a distance r_1. (Right) At time t_2 the sensor performs the measurement at the same location. Due to a change, the distance is now r_2. The difference $\Delta r = r_2 - r_1$ can be measured with the interferometric phase.

$$\Delta\Phi_{Inf,P} = \Phi_1 - \Phi_2 = \frac{4\pi}{\lambda}\Delta r \,. \tag{4}$$

Δr is the change between the measurements which can be obtained with a high accuracy. According to (4), one phase cycle of 2π corresponds to a change of half the wavelength [63]. A zero spatial baseline would be ideal for DInSAR measurements [21]. Otherwise, the sensor might see the scatterers from different angles and the condition that the stochastic scattering phase term is the same might not hold, having an effect on the measured Δr.

By forming the complex cross correlation between the signals at the first acquisition S_1 and at the second acquisition S_2, the complex interferometric coherence γ_{Inf} is obtained with:

$$\gamma_{Inf} = \frac{\langle S_1 S_2^* \rangle}{\sqrt{\langle S_1 S_1^* \rangle \langle S_2 S_2^* \rangle}}. \tag{5}$$

$\langle\cdot\rangle$ stands for the expectation value which is achieved by multilooking over a certain spatial window. The absolute value of the interferometric coherence γ_{Inf} is ranging from 0 to 1, having a high correlation at 1 and being completely decorrelated at 0. The multilooked interferometric phase $\Delta\Phi_{Inf}$ can be obtained from the complex interferometric coherence γ_{Inf}:

$$\Delta\Phi_{Inf} = \arg(\gamma_{Inf}). \tag{6}$$

The complex interferometric coherence γ_{Inf} can be used as an approximation of the phase noise [64]. For that, the probability density function pdf of the phase can be calculated with [63]:

$$pdf(\Delta\Phi_{Inf}, N) = \frac{\Gamma\left(N+\frac{1}{2}\right)\left(1-\left|\gamma_{Inf}\right|^2\right)^N \left|\gamma_{Inf}\right| \cos(\Delta\Phi_{Inf} - \Delta\Phi_0)}{2\sqrt{\pi}\Gamma(N)\left(1-\left|\gamma_{Inf}\right|^2 \cos^2(\Delta\Phi_{Inf} - \Delta\Phi_0)\right)^{N+\frac{1}{2}}} + \frac{\left(1-\left|\gamma_{Inf}\right|^2\right)^N}{2\pi} 2F_1\left(N, 1, \frac{1}{2}, \left|\gamma_{Inf}\right|^2 \cos^2(\Delta\Phi_{Inf} - \Delta\Phi_0)\right). \tag{7}$$

$\Delta\Phi_0$ is the noise-free phase and N are the number of looks of the estimation window. By applying the pdf it can be calculated that the phase standard deviation increases for lower coherences. The standard deviation of the interferometric phase can be decreased by increasing the number of looks. However, that would result in a coarser spatial resolution.

The interferometric phase can be generally separated into the following contributions:

$$\Delta\Phi_{Inf} = \Delta\Phi_{\text{topo}} + \Delta\Phi_{disp} + \Delta\Phi_{atm} + \Delta\Phi_{noise} + \Delta\Phi_s. \tag{8}$$

The topographic component is denoted as $\Delta\Phi_{topo}$ and can be removed using a DEM. In case of a line of sight displacement, for example because of subsidence, a phase contribution in $\Delta\Phi_{disp}$ is obtained. $\Delta\Phi_{atm}$ is the atmospheric component, and $\Delta\Phi_{noise}$ is the phase noise [21]. In case of snow, there will be also an additional phase component due to the snow $\Delta\Phi_s$ because of refraction inside the snow pack [31]. This phase term depends on the SWE change and is a key observable in this thesis. The relation will be used to retrieve the SWE change, see Section 1.5.1. Note that the interferometric phase can only be measured in an interval between [-π, π] [63].

1.2.2 Polarimetric SAR

In addition to the phase, another property which can be used to characterize an electromagnetic wave is its polarization. The polarization describes the time varying orientation and magnitude of the electric field vector of electromagnetic waves relative to the direction of propagation [65].

In order to be able to describe the polarization of the wave, a coordinate system is needed. Most SAR systems are acquiring data in the Horizontal-Vertical (H-V) basis. This means that the sensor is transmitting Vertically V and/or Horizontally H polarized waves and is receiving data in V and/or H polarization [21]. A way to describe this is using the Jones vector $\vec{E}$, which can be represented as a linear combination of two polarization states and can be described in the H-V basis [65].

A way to characterize the polarization is the scattering matrix $[S]$, which is a measure of how the transmitted wave $\vec{E}^t$ is changed due to the scatterer into the received wave $\vec{E}^r$:

$$\vec{E}^r = \frac{\exp(-ikr)}{r}[S]\vec{E}^{t^*}. \tag{9}$$

$k = 2\pi/\lambda$ is the wavenumber and r is the distance between the antenna and the scatterer. The factor $\frac{\exp(-ikr)}{r}$ accounts for the phase shift and attenuation of the wave travelling from the antenna to the scatterer [21].

The scattering matrix $[S]$ is given by:

$$[S] = \begin{bmatrix} S_{HH} & S_{HV} \\ S_{VH} & S_{VV} \end{bmatrix}. \tag{10}$$

The four elements of the scattering matrix are the complex scattering amplitudes in the different polarization channels. The subscripts are denoting the polarization of the received and transmitted polarization [66].

The scattering matrix can be vectorized using the scattering vector $\overrightarrow{k_L}$ in the lexicographic bases with:

$$\overrightarrow{k_L} = [s_{HH}, s_{HV}, s_{VH}, s_{VV}]^T. \tag{11}$$

The advantage of the lexicographic basis is that the elements of the scattering matrix can be directly related to the measured observables.

Another possibility to vectorize the scattering matrix in (10) is the use of the Pauli scattering vector $\overrightarrow{k_P}$ which is obtained with:

$$\overrightarrow{k_P} = \frac{1}{\sqrt{2}}[s_{HH} + s_{VV}, s_{HH} - s_{VV}, s_{HV} + s_{VH}, i(s_{HV} - s_{VH})]^T \tag{12}$$

An advantage of the Pauli basis is that it offers the possibility to interpret the elements in terms of scattering mechanisms. The first element, HH+VV, can be interpreted as single scattering from surfaces. The second element, HH-VV, stands for dihedral scattering. The third element corresponds to dihedrals with a line of sight rotation of π/4 and the last element describes a helix-type scattering, where the incident wave is transformed into its orthogonal circular polarization state [65].

The scattering matrices can be used for point-like scatterers, but are not able to describe polarization effects of distributed scatters, which are a superposition of multiple scatterers inside a resolution cell. Therefore, second-order statistics are required.

By forming the outer product of the lexicographic scattering vector $\overrightarrow{k_L}$, the polarimetric covariance matrix $[C]$ is obtained:

$$[C] = \langle \overrightarrow{k_L} \cdot \overrightarrow{k_L}^{*} \rangle, \tag{13}$$

By forming the outer product of the Pauli scattering vector $\overrightarrow{k_P}$, the polarimetric coherency matrix $[T]$ is obtained:

$$[T] = \langle \overrightarrow{k_P} \cdot \overrightarrow{k_P}^{*} \rangle. \tag{14}$$

The elements of these matrices are spatially averaged [21].

Another polarimetric variable is the complex polarimetric coherence γ_{CPD}. It can be calculated from the cross correlation between the vertical polarized signal s_{VV} and the horizontal polarized signal s_{HH}:

$$\gamma_{CPD} = \frac{\langle s_{VV} s_{HH}^{*} \rangle}{\sqrt{\langle s_{VV} s_{HH}^{*} \rangle \langle s_{VV} s_{HH}^{*} \rangle}}. \tag{15}$$

The angle of the complex polarimetric coherence γ_{CPD} is the CPD and can be calculated with:

$$\Phi_{CPD} = \arg(\gamma_{CPD}) = \Phi_{VV} - \Phi_{HH}. \tag{16}$$

The CPD Φ_{CPD} can be also represented by the difference between the phase in VV Φ_{VV} and HH Φ_{HH} [49]. This is another key observable of this thesis and the relation between the Φ_{CPD} and snow is described in Section 1.5.2.

1.2.3 Polarimetric SAR Interferometry

Polarimetric SAR Interferometry (PolInSAR) is a technique which combines interferometric and polarimetric data. As seen in Section 1.2.1, repeat-pass interferometry is sensitive to changes in the SAR image, for instance to a snow-induced phase change. Meanwhile, polarimetry allows to obtain information on the scattering mechanism and on differences between vertical and horizontal polarizations, see Section 1.2.2. Both techniques can be combined into Differential PolInSAR (DPolInSAR) by using multitemporal polarimetric data. The basics of DPolInSAR will be introduced in the following.

The temporal DPolInSAR matrix Ω_{L} is formed from the lexicographic scattering vectors of two SAR measurements acquired at two different times:

$$[\Omega_{\mathrm{L}}] = \langle \overrightarrow{k_{L,1}} \cdot \overrightarrow{k_{L,2}}^{*} \rangle \tag{17}$$

The DPolInSAR matrix contains polarimetric and interferometric information. It can be used to calculate the temporal DPolInSAR coherence at polarization $\vec{w}$ with [67]:

$$\gamma(\vec{\mathrm{w}}) = \frac{\vec{\mathrm{w}}^{+}[\Omega_L]\vec{\mathrm{w}}}{\sqrt{(\vec{\mathrm{w}}^{+}[C_1]\vec{\mathrm{w}})(\vec{\mathrm{w}}^{+}[C_2]\vec{\mathrm{w}})}}. \tag{18}$$

$[C_1]$ and $[C_2]$ are the polarimetric covariance matrices of two acquisitions at different times and can be calculated with (13). $\vec{w}$ are the unitary vectors of the polarization states. The absolute coherence describes the correlation between the two acquisitions whereas its angle denotes the DPolInSAR phase for each polarization state.

When the lexicographic basis is used, the polarization state $\overrightarrow{w_{HH}} = [1,0,0,0]^T$ corresponds to the HH polarization and the VV polarization can be obtained using $\overrightarrow{w_{VV}} = [0,0,0,1]^T$. This can be shown by projecting the scattering vector from (11) on the polarization state as can be seen in the following:

$$\overrightarrow{w_{HH}}^{+} \cdot \overrightarrow{k_L} = s_{HH} \tag{19}$$

$$\overrightarrow{w_{VV}}^{+} \cdot \overrightarrow{k_L} = s_{VV} \tag{20}$$

When using these polarization states in (18), the DInSAR coherence in HH and VV can be obtained. Beyond these standard polarization states, the unitary vector $\vec{w}$ allows to compute DPolInSAR coherences for any polarization state that is a complex combination of all polarizations.

The polarization state $\vec{w}$ is characterized by the α angle which can be directly estimated from the scattering matrix with:

$$\alpha = arccos\left(\frac{|s_{HH} + s_{VV}|}{\sqrt{2}\sqrt{|s_{HH}|^2 + |s_{HV}|^2 + |s_{VH}|^2 + |s_{VV}|^2}}\right), \qquad 0° \leq \alpha \leq 90°. \tag{21}$$

An α angle of zero degrees corresponds to surface like scattering. In comparison, an α angle of 90° corresponds to dihedral scattering [66].

It is worth highlighting again that this thesis is concerned with repeat-pass DPolInSAR, with ideally zero spatial baseline, focusing on temporal changes. This is in contrast to the more common across track PolInSAR approaches, where images of a scene are acquired from two slightly different locations but at the same time, being sensitive to the height [68]. In across-track PolInSAR, the goal is to obtain information on the vertical distribution of different scattering mechanisms [64]. This method is widely used for the estimation of forest parameters [64], [69] and also for the characterization of crop parameters [70], [71].

1.3 Physical Quantities of Snow

Snow on the ground can be described as a porous medium of ice particles in air [72]. An important physical property of snow, which is investigated in this thesis, is the SWE. It combines the information of two physical quantities of snow: the snow depth Z and snow density ρ. Z describes the vertical height of the snow pack relative to the ground surface. ρ is a measurement of the snow mass in a known reference volume [73]. Accordingly, the SWE is calculated with:

$$SWE = \frac{1}{\rho_w} \int_0^Z \rho(Z)\, dZ \approx Z\rho/\rho_w, \tag{22}$$

where ρ_w is the density of water [32]. SWE is usually measured in the units of mm and corresponds to the depth of water over a given area if the snow pack melted instantaneously [73].

1.4 Microwave Interaction with Snow

The interactions of microwaves with snow are governed by the dielectric properties of the snow [74]. Microwaves are able to penetrate into dry snow and thus are able to measure snow parameters. The ability to penetrate into the snow pack depends on the frequency, imaging geometry and also on the snow conditions. Even in firn, penetration depths of up to 9 m in C-band and 14 m in L-band have been observed in Greenland [22] and 20 m for C-band and 8 m for X-band in Antarctica [75].

One issue affecting the penetration depth is the presence of liquid water inside the snow pack. It is therefore possible to differentiate between dry and wet snow. The Liquid Water Content (LWC) is close to zero in dry snow, while wet snow is characterized by an increased LWC of $>$ 1% [76]. The presence of water in wet snow leads to an increased loss of energy inside the snow pack [77]. As it is important for this thesis that the radar wave is able to penetrate through the entire snowpack, only dry snow is considered.

Volume scattering may also have an impact on the penetration depth. However, when the ice inclusions in the snow volume are much smaller than the used radar wavelengths, volume scattering can be neglected. This is the case for frequencies below 20 GHz [78], which are used in this study. However, for higher frequencies such as Ku-band, volume scattering effects become more important and require consideration [79], [80].

The permittivity of the snow pack depends on the permittivity of air ε_{air} and ice ε_{ice}, as dry snow can be described as a mixture of ice and air. For microwave frequencies, the real part of ε_{ice} does not depend on the frequency or temperature. Therefore, the same applies to the permittivity of snow, which can be characterized by the ice volume fraction and thus depends on the snow density [81].

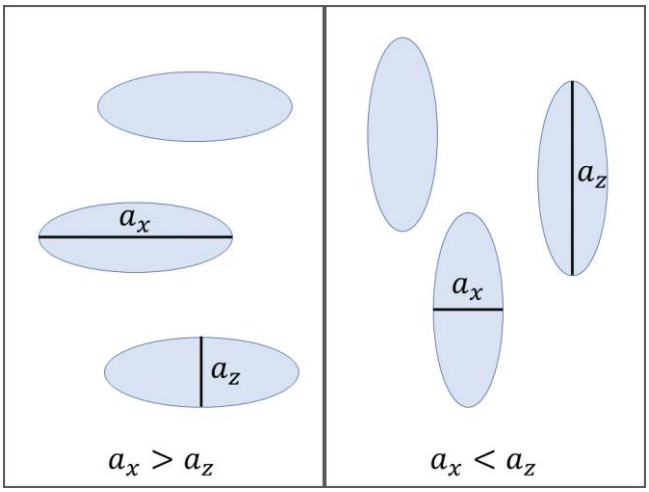

Fig. 2. Structural anisotropy: oblate particles (left), prolate particles (right).

The permittivity is a complex variable. The real part of permittivity can generally be approximated for dry snow with densities below $\rho < 0.4 g/cm^3$ and for frequencies below 10GHz with [78]:

$$\varepsilon = 1 + 1.6\rho + 1.86\rho^3 \tag{23}$$

The imaginary part is related to absorption and can be neglected for dry snow [81].

Snow densities from freshly fallen snow have been measured in a range from $0.01 - 0.25\ g/cm^3$ [82]. Older and more settled snow is associated with densities above $0.3\ g/cm^3$ [83].

The microstructure of the snow pack also has an impact on the interaction with microwaves. Computer micro tomogram scanners can be used to measure the 3-dimensional structure of a snow sample. It can be observed that snow is an anisotropic medium, so that the structure of the particles of the ice-air-mixture differs depending on the observation direction. The measurements show also that the anisotropy changes over time [84].

A parameter which describes the anisotropic structure of the snow pack is the structural anisotropy. It is the normalized difference of the x and z dimension of the ice grains a_x and a_z [50]:

$$\mathrm{A} = \frac{a_x - a_z}{0.5 * (a_x + a_z)} \tag{24}$$

The structural anisotropy becomes positive for oblate spheroids, as in the case of fresh snow, (see Fig. 2, left) and negative for prolate particles for older snow (see Fig. 2, right).

Using the structural anisotropy, the snow is modelled as ellipsoidal ice inclusions, that have the permittivity ε_{ice}, within an air background, that has the permittivity ε_{air} [50]. The effective permittivity for each axis can be calculated using the Maxwell-Garnett mixing formula [85]:

$$\varepsilon_{eff,i} = \varepsilon_{air} + f\varepsilon_{air}\frac{\varepsilon_{ice}-\varepsilon_{air}}{\varepsilon_{air}+(1-f)N_i(\varepsilon_{ice}-\varepsilon_{air})}. \quad (25)$$

i can be replaced with x, y, z for each dimension. f describes the volume fraction of the ice, which depends on the snow density. N_i is the depolarization factor, that can be calculated for each axis of the ellipsoid by integrating over the variable s, which has a squared distance unit, with:

$$N_i = \frac{a_x a_y a_z}{2}\int_0^\infty \frac{\mathrm{d}s}{(s+a_i^2)\sqrt{(s+a_x^2)(s+a_y^2)(s+a_z^2)}}. \quad (26)$$

For oblate spheroids, as in the case of fresh snow, the condition $a_x = a_y > a_z$ holds. The solutions of the integral in this case are:

$$N_x = N_y = \frac{1}{2}(1 - N_z), \quad (27)$$

$$N_z = \frac{1+e^2}{e^3}(e - \arctan e). \quad (28)$$

The parameter e is related to the anisotropy A with:

$$e = \sqrt{\left(\frac{2+A}{2-A}\right)^2 - 1}. \quad (29)$$

Prolate spheroids, which can be associated with older snow or firn, have the condition $a_x > a_y = a_z$. In this case, the integral can be solved with:

$$N_x = \frac{1-e^2}{2e^3}\left(\ln\frac{1+e}{1-e} - 2e\right), \quad (30)$$

$$N_y = N_z = \frac{1}{2}(1 - N_x). \quad (31)$$

The depolarization factors can be inserted in (25) to obtain the effective anisotropic permittivities. This way, the permittivity depending on the polarization can be obtained. However, compared to (23), assumptions on the anisotropy of the snow pack are required.

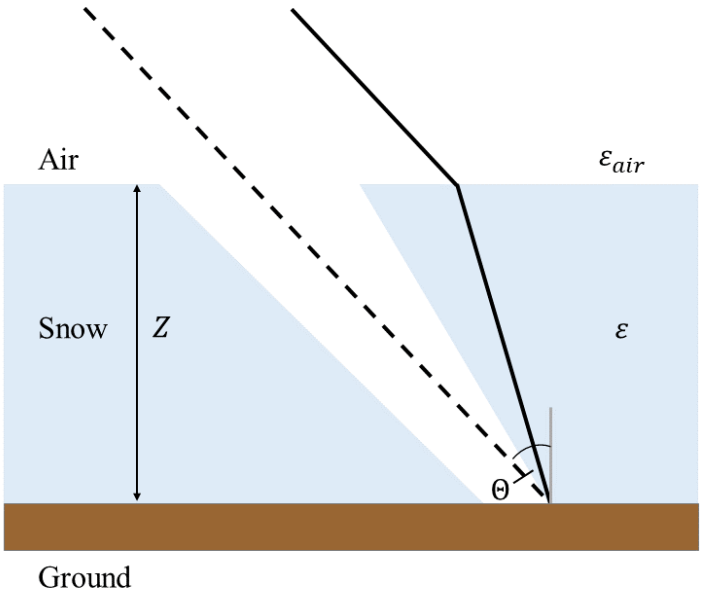

Fig. 3. Refraction of a radar wave inside a snow pack. In snow free conditions, the radar wave would travel to the ground without being refracted (dashed line). When the ground is covered by snow of the height Z, the wave is refracted inside the snow pack, because the dielectric constant of snow ε is different than the dielectric constant of air $\varepsilon_{\mathrm{air}}$ (solid line). The difference in optical path length can be related to the SWE.

1.5 SAR Phase Difference Techniques for Snow Parameter Retrieval

1.5.1 Interferometry

The interferometric phase between two repeat-pass SAR measurements can be used to estimate the SWE change between them [31]. When radar waves travel through a boundary of two mediums with different permittivities, such as snow and air, they are refracted [86]. Thus, when a radar wave travels from the sensor through air and reaches the snow pack, it is refracted and changes its direction and propagation speed, see Fig. 3. This results in a change in optical path length that depends on the amount of snow and can be measured by the phase of the radar wave. When the snow pack changes between two measurements, e.g. due to snow fall, the resulting path delay can be measured with the interferometric phase $\Delta\Phi_S$:

$$\Delta\Phi_S = -2\,k\Delta Z\left(\cos\Theta - \sqrt{\varepsilon - \sin\Theta^2}\right) \tag{32}$$

$k = 2\pi/\lambda$ is the wavenumber depending on the wavelength λ, ΔZ is the depth of the snow depth change and Θ is the incidence angle of the radar wave [31]. The part in the parentheses depends on the density (see (23)).

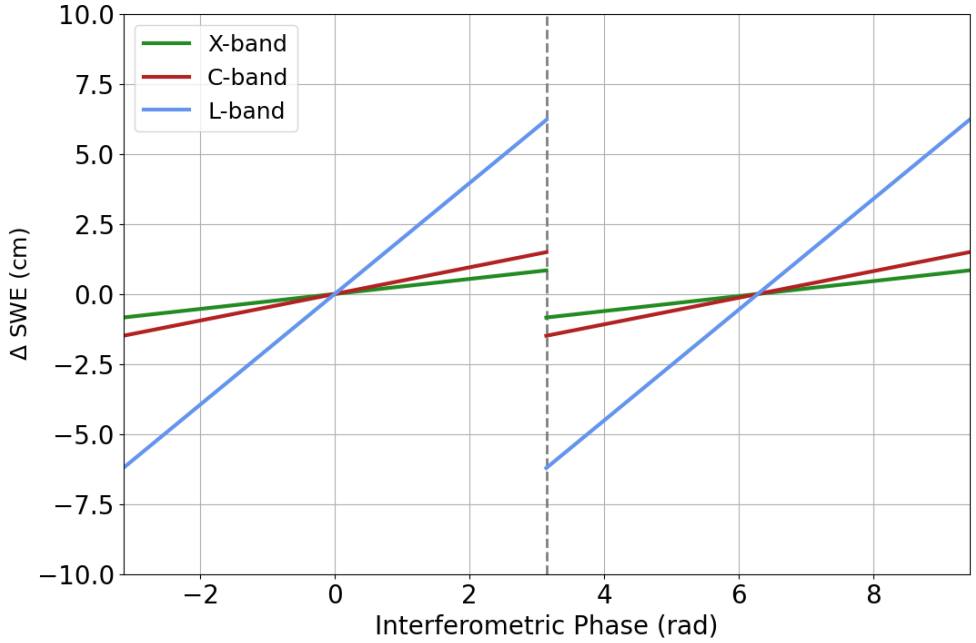

Fig. 4. ΔSWE in dependence of the interferometric phase for X-, C- and L-band for $\Theta = 34°$. At an interferometric phase of $\Delta\Phi_s = \pi$ the phase wrap threshold is reached.

A numerical approximation for the density related part of (32) has been presented, in order to model a linear relation between the interferometric phase difference and the SWE change, which can be calculated with [32]:

$$\Delta\Phi_S = 2\,k\,\frac{\alpha}{2}\left(1.59 + \Theta^{\frac{5}{2}}\right)\Delta SWE. \tag{33}$$

α is a parameter close to 1. It can be adapted for different ρ and Θ in order to reduce the Root Mean Square Error (RMSE) between the numerical approximation and the exact solution. For a fixed $\alpha = 1$, the maximum error obtained for incidence angles smaller than 40° lies below 3%.

However, one limitation of the retrieval is the fact that the interferometric phase lies in an interval between [-π, π]. This means that only a limited range of SWE change values can be retrieved unambiguously, as has been reported for example in [31], [32], [40]. An example for different frequencies is shown in Fig. 4 using (33). It can be seen that the interval in which the SWE change can be estimated unambiguously depends on the wavelength and is greater for longer wavelengths. However, for smaller SWE changes shorter wavelengths provide a higher sensitivity.

1.5.2 Polarimetry

The CPD between the VV and HH polarimetric channels can be correlated to the depth of freshly accumulated snow. Since snow has an anisotropic structure, the signal delay of the radar wave differs for VV and HH polarizations, see Fig. 5. When snow is accumulating, it aligns

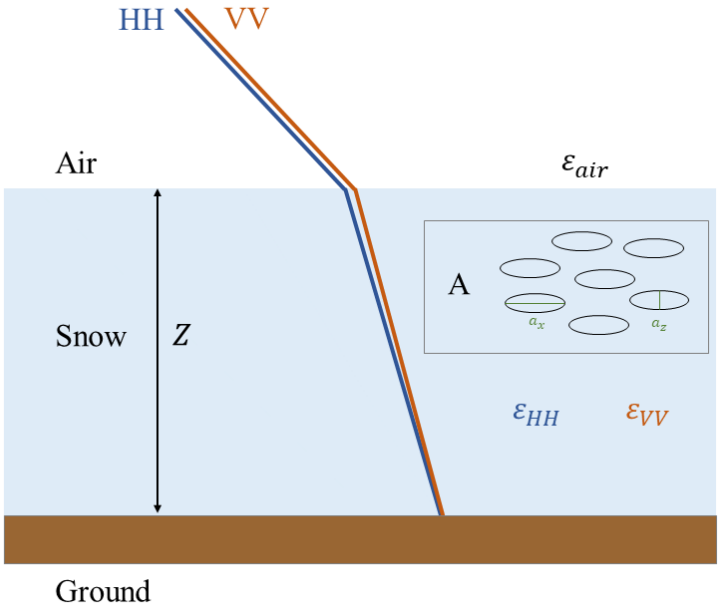

Fig. 5. Refraction of a polarized radar wave in a snow pack. When the ground is covered by snow of the height Z, the radar wave is refracted in the snow pack, because the dielectric constant of snow ε is different than the dielectric constant of air ε_{air}. Due to the fact that snow is an anisotropic medium, the dielectric constant of the snow is different for HH and VV, depending on the anisotropy A of the snow pack. This results from the orientation of the ice inclusions in air. Therefore, the refraction is different for HH and VV polarized radar waves.

horizontally because the particles are compressed by their weight. The horizontal alignment leads to a slower propagation speed of the horizontally polarized radar wave. Over time, the ice grains align more vertically due to temperature gradients. This slows down the propagation velocity of the vertically polarized radar waves. Therefore, the CPD becomes positive for fresh snow and negative for older snow packs [49].

In order to exploit the information of the CPD, it is essential to describe how the permittivity differs for each polarization. Therefore, the permittivities for each axis are calculated using (25)-(31), which can be linked to the refractive indices with:

$$n_{x,y}^2 = \varepsilon_{eff,x} = \varepsilon_{eff,y}, \tag{34}$$

$$n_z^2 = \varepsilon_{eff,z}. \tag{35}$$

These refractive indices in *x, y, z* dimension need to be translated into the radar geometry, which uses the horizontal and vertical polarization basis. This can be done by the following equations [50]:

$$n_H = n_{x,y}, \tag{36}$$

$$n_V = \sqrt{n_{x,y}^2 + \left(1 - \frac{n_{x,y}^2}{n_z^2}\right) n_{air}^2 \sin^2 \Theta}. \quad (37)$$

The refractive indices n_H of the H-polarized wave and n_V of the V-polarized wave are then used to calculate the CPD Φ_{CPD} [50]:

$$\Phi_{CPD} = (-1)2kZ\left(\sqrt{n_V^2 - \sin^2 \Theta} - \sqrt{n_H^2 - \sin^2 \Theta}\right). \quad (38)$$

This equation can be used to estimate the thickness of the fresh snow layer by assuming the anisotropy and density of the snow pack.

1.6 Research Objectives and Questions

The main research objective of this thesis is the improvement of the SWE change retrieval using repeat-pass interferometric and polarimetric SAR data.

The first key aspect is solving the phase wraps of the interferometric phase, which has a significant impact on the results, especially when high SWE changes occur and for measurements with short wavelengths. In the easiest case, phase wraps can be solved using ground-based measurements, if available. To reduce/eliminate the dependency on ground-based data, two approaches are proposed: The first uses multiple SAR frequencies, while the second relies on copolar phase differences to solve the phase wrap ambiguity.

A second key aspect is the combination of interferometric and polarimetric techniques with the goal to make use of their respective advantages and mitigate their weaknesses. This includes the exploitation of the anisotropic structure of the snow, which affects different polarizations in a different way. The goal of this approach is to take this feature into account and use polarimetric phase differences to improve the interferometric SWE change estimates.

A third key aspect is establishing a theoretical modelling framework that allows a direct consideration of polarimetric interferometric measurements into one unified DPolInSAR model that enables a DPolInSAR-based SWE retrieval. In this framework, the influence of changes of snow parameters such as depth and anisotropy on the modeled DPolInSAR parameters are investigated and utilized for an improved SWE retrieval.

The main research objective can be achieved by answering the following research questions:

- What are the performance tradeoffs of the DInSAR SWE change retrieval algorithm between different spaceborne SAR sensors with different frequencies?

- Are there ways to solve the interferometric phase wrap problem in the DInSAR SWE retrieval and which data dimensions are required for this?

- How can interferometric and polarimetric SAR measurements be combined in a unified DPolInSAR model?

- What is the added value of polarimetric phase information in the DInSAR SWE change algorithm?

- Can the DPolInSAR model improve the SWE change retrieval?

1.7 Organization of the Thesis

In the beginning of this thesis, the motivation and introduction of the topic are presented in Chapter 1 *'Introduction'*. The relevant background on SAR measurements for the scope of this thesis is described, followed by an introduction into SAR techniques for the retrieval of snow parameters. This chapter includes the research objectives and questions in Section 1.6, which will be addressed in the Chapters 2 to 4.

Chapter 2 *'The Potential of Multifrequency Spaceborne DInSAR Measurements for the Retrieval of Snow Water Equivalent'* describes the SWE change retrieval using SAR acquisitions in different frequencies. Furthermore, an approach is presented that uses multifrequency SWE change estimates in order to improve the retrieval.

Chapter 3 *'Combining Differential SAR Interferometry and Copolar Phase Differences for Snow Water Equivalent Estimation'* shows how the use of the CPD change between the measurements can help to improve the SWE change estimates.

In Chapter 4 *'Exploring DPolInSAR Coherence Regions for Snow Water Equivalent Estimation'* an approach is presented to combine interferometric and polarimetric measurements in a DPolInSAR model.

Finally, in Chapter 5 *'Conclusions'* the results of this thesis are summarized and concluded, followed by and outlook for future research.

1.8 References

[1] P. Lemke *et al.*, "Observations: Changes in Snow, Ice and Frozen Ground, in: Cli- mate Change 2007: The Physical Science Basis. Contribution of Working Group I to the Fourth Assessment Report of the Inter- governmental Panel on Climate Change," 2007.

[2] S. Marshall, R. J. Oglesby, K. A. Maasch, and G. T. Bates, "Improving climate model representations of snow hydrology," *Environ. Model.*, vol. 14, pp. 327–334, 1999.

[3] J. Cohen, "Snow cover and climate," *Weather*, vol. 49, no. 5, Art. no. 5, 1994, doi: 10.1002/j.1477-8696.1994.tb05997.x.

[4] S. Wipf and C. Rixen, "A review of snow manipulation experiments in Arctic and alpine tundra ecosystems," *Polar Res.*, vol. 29, no. 1, Art. no. 1, Jan. 2010, doi: 10.1111/j.1751-8369.2010.00153.x.

[5] K. J. Bormann, R. D. Brown, C. Derksen, and T. H. Painter, "Estimating snow-cover trends from space," *Nat. Clim. Change*, vol. 8, no. 11, pp. 924–928, 2018, doi: 10.1038/s41558-018-0318-3.

[6] T. Stillinger, C. Costello, R. C. Bales, and J. Dozier, "Reservoir Operators React to Uncertainty in Snowmelt Runoff Forecasts," *J. Water Resour. Plan. Manag.*, vol. 147, no. 10, Art. no. 10, Oct. 2021, doi: 10.1061/(ASCE)WR.1943-5452.0001437.

[7] S. Jörg-Hess, N. Griessinger, and M. Zappa, "Probabilistic Forecasts of Snow Water Equivalent and Runoff in Mountainous Areas," *J. Hydrometeorol.*, vol. 16, no. 5, Art. no. 5, Oct. 2015, doi: 10.1175/JHM-D-14-0193.1.

[8] T. P. Barnett, J. C. Adam, and D. P. Lettenmaier, "Potential impacts of a warming climate on water availability in snow-dominated regions," *Nature*, vol. 438, no. 7066, pp. 303–309, Nov. 2005, doi: 10.1038/nature04141.

[9] S. S. Carroll, G. N. Day, N. Cressie, and T. R. Carroll, "Spatial modelling of snow water equivalent using airborne and ground-based snow data," *Environmetrics*, vol. 6, no. 2, pp. 127–139, Mar. 1995, doi: 10.1002/env.3170060204.

[10] Core Writing Team, H. Lee, and J. Romero (eds.), "IPCC, 2023: Sections. In: Climate Change 2023: Synthesis Report. Contribution of Working Groups I, II and III to the Sixth Assessment Report of the Intergovernmental Panel on Climate Change," IPCC, Geneva, Switzerland. [Online]. Available: doi: 10.59327/IPCC/AR6-9789291691647

[11] L. Leppänen, A. Kontu, H.-R. Hannula, H. Sjöblom, and J. Pulliainen, "Sodankylä manual snow survey program," *Geosci. Instrum. Methods Data Syst.*, vol. 5, no. 1, pp. 163–179, 2016, doi: https://doi.org/10.5194/gi-5-163-2016.

[12] Jentzsch, Katharina *et al.*, "Automated in situ measurements of snow water equivalent, snow depth, snow temperature and snow dielectric constant, at the high Arctic Bayelva site during the winter period 2019/2020." PANGAEA - Data Publisher for Earth & Environmental Science, p. 189129 data points, 2020. doi: 10.1594/PANGAEA.925357.

[13] L. Leppänen, A. Kontu, and J. Pulliainen, "Automated Measurements of Snow on the Ground in Sodankylä," *Geophysica*, vol. 53, no. 1, pp. 45–64, 2018.

[14] J. C. Comiso, "Satellite remote sensing of the Polar Oceans," *J. Mar. Syst.*, vol. 2, no. 3–4, pp. 395–434, Aug. 1991, doi: 10.1016/0924-7963(91)90044-U.

[15] R. L. Armstrong, A. Chang, A. Rango, and E. Josberger, "Snow depths and grain-size relationships with relevance for passive microwave studies," *Ann. Glaciol.*, vol. 17, pp. 171–176, 1993, doi: 10.3189/S0260305500012799.

[16] A. T. C. Chang, J. L. Foster, and D. K. Hall, "Nimbus-7 SMMR Derived Global Snow Cover Parameters," *Ann. Glaciol.*, vol. 9, pp. 39–44, 1987, doi: 10.3189/S0260305500200736.

[17] R. Kelly, "The AMSR-E Snow Depth Algorithm: Description and Initial Results," *J. Remote Sens. Soc. Jpn.*, vol. 29, no. 1, Art. no. 1, 2009, doi: 10.11440/rssj.29.307.

[18] M. Takala *et al.*, “Estimating northern hemisphere snow water equivalent for climate research through assimilation of space-borne radiometer data and ground-based measurements,” *Remote Sens. Environ.*, vol. 115, no. 12, Art. no. 12, Dec. 2011, doi: 10.1016/j.rse.2011.08.014.

[19] B. J. Vander Jagt, M. T. Durand, S. A. Margulis, E. J. Kim, and N. P. Molotch, “The effect of spatial variability on the sensitivity of passive microwave measurements to snow water equivalent,” *Remote Sens. Environ.*, vol. 136, pp. 163–179, Sep. 2013, doi: 10.1016/j.rse.2013.05.002.

[20] D. Li, M. Durand, and S. A. Margulis, “Potential for hydrologic characterization of deep mountain snowpack via passive microwave remote sensing in the Kern River basin, Sierra Nevada, USA,” *Remote Sens. Environ.*, vol. 125, pp. 34–48, Oct. 2012, doi: 10.1016/j.rse.2012.06.027.

[21] A. Moreira, P. Prats-Iraola, M. Younis, G. Krieger, I. Hajnsek, and K. P. Papathanassiou, “A tutorial on synthetic aperture radar,” *IEEE Geosci. Remote Sens. Mag.*, vol. 1, no. 1, Art. no. 1, Mar. 2013, doi: 10.1109/MGRS.2013.2248301.

[22] E. Rignot, K. Echelmeyer, and W. Krabill, “Penetration depth of interferometric synthetic-aperture radar signals in snow and ice,” *Geophys Res Lett*, vol. 28, pp. 3501–3504, Sep. 2001, doi: https://doi.org/10.1029/2000GL012484.

[23] C. Mätzler, “Microwave permittivity of dry snow,” *IEEE Trans. Geosci. Remote Sens.*, vol. 34, no. 2, Art. no. 2, Mar. 1996, doi: 10.1109/36.485133.

[24] J. Zhu, S. Tan, J. King, C. Derksen, J. Lemmetyinen, and L. Tsang, “Forward and Inverse Radar Modeling of Terrestrial Snow Using SnowSAR Data,” *IEEE Trans. Geosci. Remote Sens.*, vol. 56, no. 12, pp. 7122–7132, Dec. 2018, doi: 10.1109/TGRS.2018.2848642.

[25] L. D. Gregorio *et al.*, “SWE retrieval by exploiting COSMO-SkyMed X-band SAR imagery and ground data through a machine learning approach,” in *Active and Passive Microwave Remote Sensing for Environmental Monitoring III*, F. Bovenga, C. Notarnicola, N. Pierdicca, and E. Santi, Eds., SPIE, 2019, pp. 38–48. doi: 10.1117/12.2550824.

[26] H. Rott *et al.*, “Cold Regions Hydrology High-Resolution Observatory for Snow and Cold Land Processes,” *Proc. IEEE*, vol. 98, no. 5, pp. 752–765, 2010, doi: 10.1109/JPROC.2009.2038947.

[27] H. Lievens *et al.*, “Snow depth variability in the Northern Hemisphere mountains observed from space,” *Nat. Commun.*, vol. 10, pp. 1–12, 2019, doi: 10.1038/s41467-019-12566-y.

[28] H. Lievens, I. Brangers, H.-P. Marshall, T. Jonas, M. Olefs, and G. D. Lannoy, “Sentinel-1 snow depth retrieval at sub-kilometer resolution over the European Alps,” *The Cryosphere*, vol. 16, no. 1, pp. 159–177, 2022, doi: 10.5194/tc-16-159-2022.

[29] L. Tsang *et al.*, “Review article: Global monitoring of snow water equivalent using high-frequency radar remote sensing,” *The Cryosphere*, vol. 16, no. 9, pp. 3531–3573, Sep. 2022, doi: 10.5194/tc-16-3531-2022.

[30] S. Leinss, O. Antropov, J. Vehvilaeinen, J. Lemmetyinen, I. Hajnsek, and J. Praks, “Wet Snow Depth from Tandem-X Single-Pass Insar Dem Differencing,” in *IGARSS 2018 - 2018 IEEE International Geoscience and Remote Sensing Symposium*, Jul. 2018, pp. 8500–8503. doi: 10.1109/IGARSS.2018.8518661.

[31] T. Guneriussen, K. A. Hogda, H. Johnsen, and I. Lauknes, “InSAR for estimation of changes in snow water equivalent of dry snow,” *IEEE Trans. Geosci. Remote Sens.*, vol. 39, no. 10, Art. no. 10, Oct. 2001, doi: 10.1109/36.957273.

[32] S. Leinss, A. Wiesmann, J. Lemmetyinen, and I. Hajnsek, “Snow Water Equivalent of Dry Snow Measured by Differential Interferometry,” *IEEE J. Sel. Top. Appl. Earth Obs. Remote Sens.*, vol. 8, no. 8, Art. no. 8, Aug. 2015, doi: 10.1109/JSTARS.2015.2432031.

[33] J. J. Ruiz *et al.*, "Investigation of Environmental Effects on Coherence Loss in SAR Interferometry for Snow Water Equivalent Retrieval," *IEEE Trans. Geosci. Remote Sens.*, vol. 60, pp. 1–15, 2022, doi: 10.1109/TGRS.2022.3223760.

[34] H. P. Marshall *et al.*, "L-Band InSAR Depth Retrieval During the NASA SnowEx 2020 Campaign: Grand Mesa, Colorado," in *2021 IEEE International Geoscience and Remote Sensing Symposium IGARSS*, Brussels, Belgium: IEEE, Jul. 2021, pp. 625–627. doi: 10.1109/IGARSS47720.2021.9553852.

[35] J. Tarricone, R. W. Webb, H.-P. Marshall, A. W. Nolin, and F. J. Meyer, "Estimating snow accumulation and ablation with L-band interferometric synthetic aperture radar (InSAR)," *The Cryosphere*, vol. 17, pp. 1997–2019, 2023, doi: 10.5194/tc-17-1997-2023.

[36] R. T. Palomaki and E. A. Sproles, "Assessment of L-band InSAR snow estimation techniques over a shallow, heterogeneous prairie snowpack," *Remote Sens. Environ.*, vol. 296, no. 113744, pp. 1–17, 2023, doi: 10.1016/j.rse.2023.113744.

[37] Z. Hoppinen, S. Oveisgharan, H.-P. Marshall, R. Mower, K. Elder, and C. Vuyovich, "Snow water equivalent retrieval over Idaho – Part 2: Using L-band UAVSAR repeat-pass interferometry," *The Cryosphere*, vol. 18, pp. 575–592, 2024, doi: 10.5194/tc-18-575-2024.

[38] R. Bonnell *et al.*, "Evaluating L-band InSAR snow water equivalent retrievals with repeat ground-penetrating radar and terrestrial lidar surveys in northern Colorado," *The Cryosphere*, vol. 18, no. 8, pp. 3765–3785, 2024, doi: 10.5194/tc-18-3765-2024.

[39] T. Nagler *et al.*, "Airborne Experiment on Insar Snow Mass Retrieval in Alpine Environment," *IGARSS 2022-2022 IEEE Int. Geosci. Remote Sens. Symp.*, pp. 4549–4552, Jul. 2022, doi: 10.1109/IGARSS46834.2022.9883809.

[40] H. Rott, T. Nagler, and R. Scheiber, "Snow Mass Retrieval by Means of SAR Interferometry," in *Proc. of FRINGE 2003 Workshop*, Italy, 2003, pp. 1–6.

[41] H. Li, Z. Wang, G. He, and W. Man, "Estimating Snow Depth and Snow Water Equivalence Using Repeat-Pass Interferometric SAR in the Northern Piedmont Region of the Tianshan Mountains," *J. Sens.*, vol. 2017, pp. 1–17, 2017, doi: 10.1155/2017/8739598.

[42] V. Conde, C. Nico, P. Mateus, J. Catalao, A. Kontu, and M. Gritsevich, "On the estimation of temporal changes of snow water equivalent by spaceborne SAR interferometry: a new application for the Sentinel-1 mission," *J. Hydrol. Hydromech.*, vol. 67, no. 1, Art. no. 1, 2019, doi: 10.2478/johh-2018-0003.

[43] A. B. Mahmoodzada, "Capability assessment of Sentinel-1 data for estimation of snow hydrological potential in the Khanabad watershed in the Hindu Kush Himalayas of Afghanistan," *Remote Sens. Appl. Soc. Environ.*, vol. 26, no. 100758, pp. 1–11, 2022, doi: 10.1016/j.rsase.2022.100758.

[44] J. Eppler, B. Rabus, and P. Morse, "Snow water equivalent change mapping from slope-correlated synthetic aperture radar interferometry (InSAR) phase variations," *The Cryosphere*, vol. 16, no. 4, pp. 1497–1521, 2022, doi: 10.5194/tc-16-1497-2022.

[45] S. Oveisgharan, R. Zinke, Z. Hoppinen, and H. P. Marshall, "Snow water equivalent retrieval over Idaho – Part 1: Using Sentinel-1 repeat-pass interferometry," *The Cryosphere*, vol. 18, no. 2, pp. 559–574, 2024, doi: 10.5194/tc-18-559-2024.

[46] A. Benedikter, M. Rodriguez-Cassola, P. Prats-Iraola, K. Belinska, and G. Krieger, "On the Decorrelation Effect of Dry Snow in Differential SAR Interferometry," *IGARSS 2023-2023 IEEE Int. Geosci. Remote Sens. Symp.*, pp. 8323–8326, 2023, doi: 10.1109/IGARSS52108.2023.10282149.

[47] P. N. Dagurov, T. N. Chimitdorzhiev, A. V. Dmitriev, and S. I. Dobrynin, "Estimation of snow water equivalent from L-band radar interferometry: simulation and experiment," *Int. J. Remote Sens.*, vol. 41, no. 24, pp. 9328–9359, Dec. 2020, doi: 10.1080/01431161.2020.1798551.

[48] J. J. Ruiz, J. Lemmetyinen, J. Cohen, A. Kontu, T. Nagler, and J. Pulliainen, “Comparing InSAR Snow Water Equivalent Retrieval Using ALOS2 With In Situ Observations and SnowModel Over the Boreal Forest Area,” *IEEE Trans. Geosci. Remote Sens.*, vol. 62, pp. 1–14, 2024, doi: 10.1109/TGRS.2024.3439855.

[49] S. Leinss, G. Parrella, and I. Hajnsek, “Snow Height Determination by Polarimetric Phase Differences in X-Band SAR Data,” *IEEE J. Sel. Top. Appl. Earth Obs. Remote Sens.*, vol. 7, no. 9, Art. no. 9, Sep. 2014, doi: 10.1109/JSTARS.2014.2323199.

[50] S. Leinss, H. Löwe, M. Proksch, J. Lemmetyinen, A. Wiesmann, and I. Hajnsek, “Anisotropy of seasonal snow measured by polarimetric phase differences in radar time series,” *The Cryosphere*, vol. 10, no. 4, Art. no. 4, Aug. 2016, doi: 10.5194/tc-10-1771-2016.

[51] JP. Dedieu *et al.*, “Improvement of snow physical parameters retrieval using SAR data in the Arctic (Svalbard),” ISSW, Oct. 2018.

[52] J. Voglimacci-Stephanopoli *et al.*, “Potential of X-band polarimetric synthetic aperture radar co-polar phase difference for arctic snow depth estimation,” *The Cryosphere*, vol. 16, pp. 2163–2181, 2022, doi: 10.5194/tc-16-2163-2022.

[53] S. Majumdar, P. K. Thakur, L. Chang, and S. Kumar, “X-Band Polarimetric Sar Copolar Phase Difference for Fresh Snow Depth Estimation in the Northwestern Himalayan Watershed,” in *IGARSS 2019 - 2019 IEEE International Geoscience and Remote Sensing Symposium*, Yokohama, Japan: IEEE, Jul. 2019, pp. 4102–4105. doi: 10.1109/IGARSS.2019.8898884.

[54] A. Patil, G. Singh, and C. Rüdiger, “Retrieval of Snow Depth and Snow Water Equivalent Using Dual Polarization SAR Data,” *Remote Sens.*, vol. 12, no. 7, Art. no. 7, Apr. 2020, doi: 10.3390/rs12071183.

[55] G. Parrella, I. Hajnsek, and K. P. Papathanassiou, “Retrieval of Firn Thickness by Means of Polarisation Phase Differences in L-Band SAR Data,” *Remote Sens.*, vol. 13, no. 4448, pp. 1–9, 2021, doi: 10.3390/rs13214448.

[56] M. Stefko, P. Bernhard, O. Frey, and I. Hajnsek, “Polarimetric Analysis of Biseasonal Monostatic and Bistatic Radar Observations of a Glacier Accumulation Zone at Ku-Band,” *IEEE J. Sel. Top. Appl. Earth Obs. Remote Sens.*, vol. 17, pp. 9706–9727, 2024, doi: 10.1109/JSTARS.2024.3374051.

[57] M. I. Skolnik, *Radar handbook*, 3rd ed. New York: McGraw-Hill, 2008.

[58] C. Oliver and S. Quegan, *Understanding Synthetic Aperture Radar Images*. in SciTech radar and defense series. SciTech Publ., 2004. [Online]. Available: https://books.google.de/books?id=IeGKe40S77AC

[59] L. Cutrona, *Synthetic aperture radar*, vol. 2. in Radar handbook, vol. 2. New York: McGraw-Hill New York, 1990.

[60] C. Palmann, S. Mavromatis, M. Hernandez, J. Sequeira, and B. Brisco, “Earth observation using radar data: an overview of applications and challenges,” *Int. J. Digit. Earth*, vol. 1, no. 2, pp. 171–195, 2008, doi: 10.1080/17538940802038317.

[61] T. Nagler and H. Rott, “Retrieval of wet snow by means of multitemporal SAR data,” *IEEE Trans. Geosci. Remote Sens.*, vol. 38, no. 2, pp. 754–765, 2000, doi: 10.1109/36.842004.

[62] M. Crosetto, B. Crippa, E. Biescas, O. Monserrat, and M. Agudo, “State of the art of land deformation monitoring using differential SAR interferometry,” *ISPRS Hann. Workshop*, pp. 17–20, 2005.

[63] R. Bamler and P. Hartl, “Synthetic aperture radar interferometry,” *Inverse Probl.*, vol. 14, no. 4, Art. no. 4, Aug. 1998, doi: 10.1088/0266-5611/14/4/001.

[64] S. R. Cloude and K. P. Papathanassiou, “Polarimetric SAR interferometry,” *IEEE Trans. Geosci. Remote Sens.*, vol. 36, no. 5, Art. no. 5, Sep. 1998, doi: 10.1109/36.718859.

[65] C. Lopez-Martinez and E. Pottier, “Basic Principles of SAR Polarimetry,” in *Hajnsek, I., Desnos, YL. (eds) Polarimetric Synthetic Aperture Radar. Remote Sensing and Digital Image Processing*, Springer International Publishing, 2021, pp. 1–58. [Online]. Available: 10.1007/978-3-030-56504-6_1

[66] S. Cloude, *Polarisation: applications in remote sensing*, 1st ed. Oxford ; New York: Oxford University Press, 2010.

[67] J. Ni, C. Lopez-Martinez, Z. Hu, and F. Zhang, “Multitemporal SAR and Polarimetric SAR Optimization and Classification: Reinterpreting Temporal Coherence,” *IEEE Trans. Geosci. Remote Sens.*, vol. 60, pp. 1–17, 2022, doi: 10.1109/TGRS.2022.3214097.

[68] R. Gens and J. L. van Genderen, “Review Article SAR interferometry—issues, techniques, applications,” *Int. J. Remote Sens.*, vol. 17, no. 10, pp. 1803–1835, 1996, doi: 10.1080/01431169608948741.

[69] K. P. Papathanassiou and S. R. Cloude, “Single-baseline polarimetric SAR interferometry,” *IEEE Trans. Geosci. Remote Sens.*, vol. 39, no. 11, pp. 2352–2363, 2001, doi: 10.1109/36.964971.

[70] J. M. Lopez-Sanchez, I. Hajnsek, and J. D. Ballester-Berman, “First Demonstration of Agriculture Height Retrieval With PolInSAR Airborne Data,” *IEEE Geosci. Remote Sens. Lett.*, vol. 9, no. 2, pp. 242–246, 2012, doi: 10.1109/LGRS.2011.2165272.

[71] N. Romero-Puig, J. M. Lopez-Sanchez, and M. Busquier, “Evaluation of PolInSAR Observables for Crop-Type Mapping Using Bistatic TanDEM-X Data,” *IEEE Geosci. Remote Sens. Lett.*, vol. 19, pp. 1–5, 2022, doi: 10.1109/LGRS.2022.3175689.

[72] C. Fierz *et al.*, “The International Classification for Seasonal Snow on the Ground.,” IHP-VII Technical Documents in Hydrology N° 83, UNESCO-IHP, Paris, 2009.

[73] N. J. Kinar and J. W. Pomeroy, “Measurement of the physical properties of the snowpack,” *Rev. Geophys.*, vol. 53, pp. 481–544, 2015, doi: doi:10.1002/2015RG000481.

[74] C. Mätzler, “Applications of the interaction of microwaves with the natural snow cover,” *Remote Sens. Rev.*, vol. 2, no. 2, pp. 259–387, 1987, doi: 10.1080/02757258709532086.

[75] H. Rott, K. Sturm, and H. Miller, “Active and passive microwave signatures of Antarctic firn by means of field measurements and satellite data.,” *Ann. Glaciol.*, vol. 17, pp. 337–343, 1993, doi: 10.3189/S0260305500013070.

[76] D. Varade, O. Dikshit, and S. Manickam, “Dry/wet snow mapping based on the synergistic use of dual polarimetric SAR and multispectral data,” *J. Mt. Sci.*, vol. 16, no. 6, pp. 1435–1451, 2019, doi: 10.1007/s11629-019-5373-3.

[77] F. Koch *et al.*, “Retrieval of Snow Water Equivalent, Liquid Water Content, and Snow Height of Dry and Wet Snow by Combining GPS Signal Attenuation and Time Delay,” *Water Resour. Res.*, vol. 55, no. 5, pp. 4465–4487, 2019, doi: https://doi.org/10.1029/2018WR024431.

[78] A. Wiesmann and C. Mätzler, “Microwave Emission Model of Layered Snowpacks,” *Remote Sens. Environ.*, vol. 70, no. 3, Art. no. 3, 1999, doi: https://doi.org/10.1016/S0034-4257(99)00046-2.

[79] K. Veijola, J. Cohen, M. Mäkynen, J. Lemmetyinen, J. Praks, and B. Cheng, “X- and Ku-Band SAR Backscattering Signatures of Snow-Covered Lake Ice and Sea Ice,” vol. 16, no. 2, 2024, doi: 10.3390/rs16020369.

[80] B. Montpetit *et al.*, “Retrieval of snow and soil properties for forward radiative transfer modeling of airborne Ku-band SAR to estimate snow water equivalent: the Trail Valley Creek 2018/19 snow experiment,” *The Cryosphere*, vol. 18, pp. 3857–3874, 2024, doi: 10.5194/tc-18-3857-2024.

[81] M. Hallikainen, F. Ulaby, and M. Abdelrazik, “Dielectric properties of snow in the 3 to 37 GHz range,” *IEEE Trans. Antennas Propag.*, vol. 34, no. 11, pp. 1329–1340, Nov. 1986, doi: 10.1109/TAP.1986.1143757.

[82] A. Judson and N. Doesken, “Density of Freshly Fallen Snow in the Central Rocky Mountains,” *Bull. Am. Meteorol. Soc.*, vol. 8, no. 7, pp. 1577–1588, 2000, doi: 10.1175/1520-0477(2000)081<1577:DOFFSI>2.3.CO;2.

[83] C. F. Bohren and R. L. Beschta, “Snowpack Albedo and Density,” *Cold Reg. Sci. Technol.*, vol. 1, no. 1, pp. 47–50, 1979, doi: 10.1016/0165-232X(79)90018-1.

[84] M. Schneebeli and S. A. Sokratov, “Tomography of temperature gradient metamorphism of snow and associated changes in heat conductivity,” *Hydrol Process*, vol. 28, pp. 3655–3665, 2004, doi: 10.1002/hyp.5800.

[85] A. Sihvola, “Mixing Rules with Complex Dielectric Coefficients,” *Subsurf. Sens. Technol. Appl.*, vol. 1, no. 4, pp. 393–415, 2000, doi: https://doi.org/10.1023/A:1026511515005.

[86] M. Born and E. Wolf, *Principles of optics: electromagnetic theory of propagation, interference and diffraction of light*. Elsevier, 2013.

2 The Potential of Multifrequency Spaceborne DInSAR Measurements for the Retrieval of Snow Water Equivalent

K. Belinska, G. Fischer, G. Parrella and I. Hajnsek

IEEE Journal of Selected Topics in Applied Earth Observations and Remote Sensing

Published in vol. 17, pp. 2950 – 2962, December 2023, DOI: 10.1109/JSTARS.2023.3345139

This chapter is a post-print, differing from the published paper only in terms of layout and formatting.

The author's contributions:

- Interferometric processing of the SAR data.
- Implementation of the SWE retrieval algorithm.
- Conceptualization and implementation of the phase wrap correction.
- Analysis and interpretation of the results.
- Writing of the manuscript.

The co-authors' contributions:

- G. Fischer, G. Parrella and I. Hajnsek supervised the research.
- G. Fischer, G. Parrella and I. Hajnsek contributed to the main ideas, the discussion of the results, and reviewed the manuscript.

THE POTENTIAL OF MULTIFREQUENCY SPACEBORNE DINSAR MEASUREMENTS FOR THE RETRIEVAL OF SNOW WATER EQUIVALENT

Kristina Belinska[1,2], Georg Fischer[1], Giuseppe Parrella[3], and Irena Hajnsek[1,2]
[1] German Aerospace Center, Microwaves and Radar Institute, Wessling, Germany
[2] ETH Zurich, Institute of Environmental Engineering, Zurich, Switzerland
[3] European Space Agency (ESA), Frascati, Italy

Abstract

The snow water equivalent (SWE) is the amount of water contained in a snow pack and is, therefore, an important variable for hydrological and climate models. Differential interferometric synthetic aperture radar (DInSAR) techniques can relate the interferometric phase of two repeat-pass SAR acquisitions to the SWE change between them. However, only a limited interval of SWE change can be retrieved unambiguously due to phase wraps of the interferometric phase. This interval strongly depends on the wavelength of the radar wave. Additional information, for instance ground measurements of SWE, is required to identify whether the SWE change exceeded that interval and to correct the phase wraps. In the study, the performance of X-, C- and L-band spaceborne SAR acquisitions for SWE estimation is analyzed, demonstrating the advantages and limitations of different frequencies. Shorter wavelengths show a higher accuracy for SWE estimations, while longer wavelengths are less affected by phase wraps. A multifrequency approach is proposed where L-band acquisitions are used to correct the phase wraps in the C-band SWE retrieval. The accuracy decreases slightly, but this approach allows a more robust SWE retrieval without the need of additional ground measurements. For current spaceborne SAR missions, temporal decorrelation and phase calibration are limiting factors.

2.1 Introduction

The seasonal snow cover is an essential variable for climate and hydrological models. While the high albedo and emissivity of snow have an important impact on the Earth's energy budget [1], increasing temperatures lead to accelerated melting of snow, and also of land ice, which results in a sea level rise [2],[3].

Rising temperatures also cause the alteration of runoff regimes in mountainous areas, which has a high impact on regions where people rely on snowmelt for their water supply and water storage capabilities are not sufficient [4].

A parameter which can be used to characterize this is the snow water equivalent (SWE), which describes the amount of liquid water stored in a snow pack and is thus an important variable in hydrological models for runoff predictions [5].

Ground-based measurements of SWE provide precise information but can typically cover only small areas and are performed on a limited number of locations, as snow covered areas are often characterized by extreme weather conditions and are located in remote regions which can be hard to access. A wider coverage is typically achieved by interpolation of sparsely sampled data, leading to large uncertainties and coarse spatial resolution.

However, the employment of remote sensing techniques enables a wide coverage and high temporal resolution. Microwave sensors offer the possibility to monitor the Earth's surface in a systematic way independently from sunlight illumination and weather conditions. This is particularly important for high latitude regions, which are affected by polar darkness [6] and often covered by clouds [7].

Passive microwave sensors like radiometers are able to deliver global snow products, including SWE, on a daily basis [8], [9]. The retrieval algorithms rely on the link between the brightness temperature and the presence of snow on the observed surface [10]. However, the snow signal measured by passive sensors saturates for deep snow packs [11]. In addition, the global daily coverage offered by such sensors is achieved at the cost of a spatial resolution on kilometer-scale [12].

Active microwave sensors, on the other hand, like synthetic aperture radars (SARs), offer a spatial resolution on meter-scale [13], which is required for an accurate mapping of mountainous areas and heterogeneous landscapes and could significantly enhance SWE information products.

The sensitivity of SAR measurements to snow properties has been already demonstrated in early studies [14], [15] opening the way towards the retrieval of relevant parameters, such as snow depth and SWE.

Different SWE retrieval models based on radiative transfer models have been established [16], [17], [18]. In cases of wet snow, the retrieval of snow depth has also been attempted with single-pass radar interferometry by differencing two digital elevation models (DEMs) [19]. Other studies have shown that the polarizations of radar waves can be utilized for the retrieval of snow parameters [20], [21].

A promising and straightforward approach to retrieve SWE has been proposed first in [22], and then, in [23], exploiting differential interferometry (DInSAR) between two temporally separated SAR acquisitions. It relies on the fact that microwaves are refracted in dry snow which has an effect on the interferometric phase. The theory shows that changes in SWE between two acquisitions cause a change in the path delay of the radar waves which provides a direct link between the temporal evolution of SWE and the interferometric phase measured by the SAR

system. The model proposed in [22] has been further refined in [23] in order to extend its applicability to a wider range of snow densities.

The method has been successfully demonstrated using time series data from a tower-based instrument measuring with a temporal baseline of 4 hours [23] and also with a multifrequency tower-based experiment, analyzing the influence of environmental effects on the coherence [24].

The transferability of such an approach to the spaceborne case has been already assessed in several studies [25],[26],[27], [28]. Some of which showed that the revisit time of current missions is one of the main limiting factors, as well as the lack of validation data. However, only single-frequency measurements were assessed.

This study aims to provide further insights into the SWE estimation from multifrequency spaceborne data using the approach of [23]. Datasets at different frequencies, X-, C- and L-band, acquired by operational satellite SAR missions (TanDEM-X, Sentinel-1 and ALOS-2) are jointly exploited to assess the main aspects determining the performance, such as the temporal resolution and the different interferometric sensitivities. The estimated SWE values are compared to ground-based measurements from a test site in Finland. Particular emphasis is put on the estimation error due to phase wrapping of the interferometric phase. This is analyzed by utilizing the ground measurements for the phase wrap correction. Furthermore, a multifrequency solution is presented, where measurements with different frequencies are exploited to correct for missing phase cycles. Such a multifrequency approach reduces the necessity for external SWE information to solve phase wrapping, which is essential for future large scale spaceborne applications.

The rest of this article is organized as follows. In Section 2.2, the model of [23] relating DInSAR measurements to SWE changes is described, and its frequency-dependent sensitivity analyzed. Section 2.3 presents the employed experimental ground measurements and spaceborne SAR datasets as well as the processing steps. The results of the SWE estimation, including the ground-based and multifrequency phase wrap corrections, are reported and discussed in Section 2.4. Finally, Section 2.5 concludes this article.

2.2 Theory and Methods

2.2.1 Relationship DInSAR Phase and SWE Change

The SWE parameter combines the information on snow density ρ_s and snow depth Z_s and refers to the theoretical depth of water which is obtained if the snow pack melted instantaneously. It can be expressed as

$$SWE = \frac{1}{\rho_w} \int_0^{Z_s} \rho_s(z)\, dz \approx Z_s \rho_s / \rho_w \tag{1}$$

where ρ_w is the density of water.

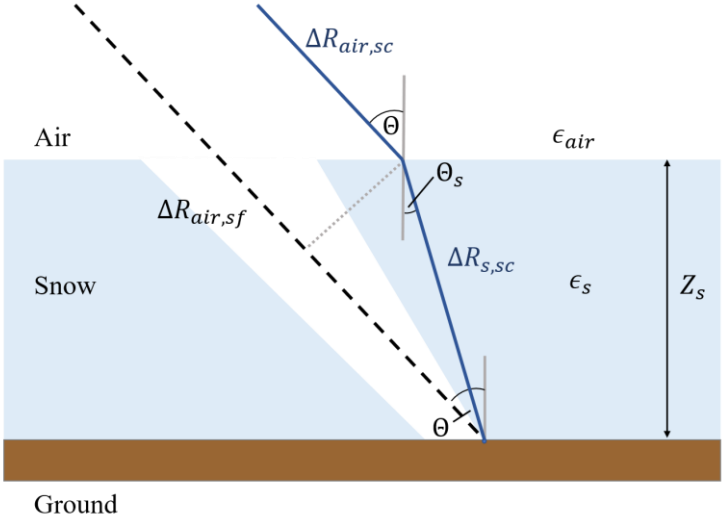

Fig. 1. Refraction of a radar wave in a snow pack. When the ground is covered by snow of the height Z_S, the radar wave travels first the distance $\Delta R_{air,sc}$ in air and is then refracted in the snow pack, because the dielectric constant of snow ϵ_s is different than the dielectric constant of air ϵ_{air}. After the distance $\Delta R_{s,sc}$, it reaches the ground. For snow-free conditions, the radar wave travels the distance $\Delta R_{air,sf}$.

The model proposed in [23] for SWE change estimation of dry snow using repeat-pass SAR interferometry is based on a nearly linear relationship between the SWE change and the differential interferometric phase between two SAR acquisitions [22].

The interaction between the radar waves and snow is governed by the dielectric properties of snow. Since snow has a different dielectric constant than air, a radar wave experiences refraction when propagating through a snow layer, as shown in Fig. 1. When comparing the optical path length of the wave for snow-free and snow-covered conditions, a path delay can be observed, which results from the different path length due to refraction in the snow pack and also from the different propagation speed of the radar wave in the snow. This path delay also occurs in the case of a snow depth change ΔZ_s between two measurements and is proportional to ΔZ_s. Such delay translates into a DInSAR phase difference which can be, in turn, linked to the snow depth change. By considering the geometry in Fig. 1, a nearly linear relationship between the SWE change and the differential interferometric phase between two SAR acquisitions can be obtained. The relation between the interferometric phase difference $\Delta\Phi_s$ and SWE change ΔSWE is then the following [23]:

$$\Delta\Phi_s = 2\,k\,\frac{\alpha}{2}\left(1.59 + \Theta^{\frac{5}{2}}\right)\Delta SWE, \tag{2}$$

where α is a parameter close to 1, which can be adjusted to reduce the root mean square error (RMSE) between the numerical approximation and the exact solution for different snow densities and incidence angles. For snow densities between $0.2\ g/cm^3$ and $0.4\ g/cm^3$ and incidence

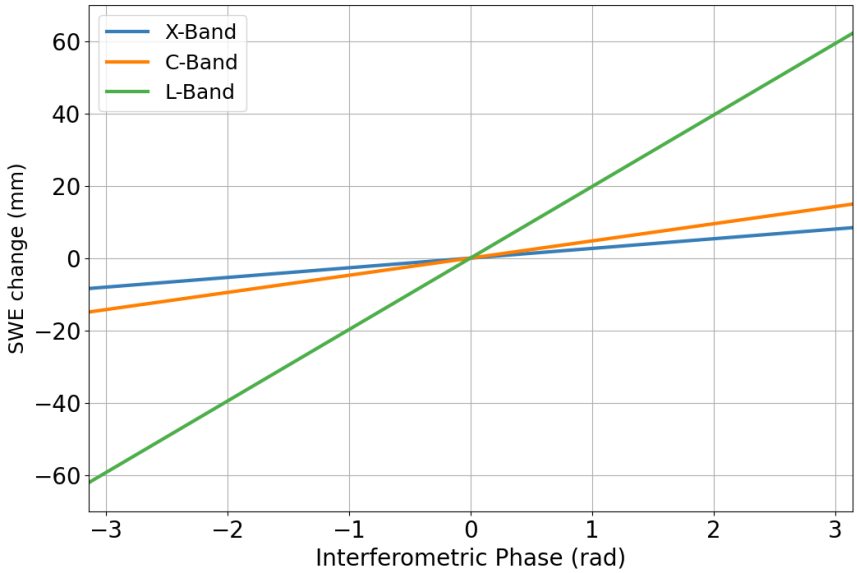

Fig. 2. SWE change in dependence of the interferometric phase for X-, C- and L-band. For a certain SWE change, smaller interferometric phases are measured for longer wavelengths.

angles between 30° and 40°, α is lying in the range from 0.98 to 1. However, when using a fixed value of $\alpha = 1$ the maximum error for incidence angles smaller 40° lies below 3% [23].

For dry snow, which is of interest for this study, the absorption is assumed to be negligible and is, therefore, not considered. Furthermore, volume scattering in the snow pack is not considered, as it can be neglected for dry snow and frequencies below 20 GHz [29].

It can be seen in (2) that the interferometric phase difference is positive if the SWE increases between the two acquisitions, due to the linear relation between ΔSWE and $\Delta\Phi_s$.

By rearranging (2) an expression for the SWE change ΔSWE is obtained

$$\Delta SWE = \frac{\Delta\Phi_s}{k\alpha\left(1.59 + \Theta^{\frac{5}{2}}\right)}, \tag{3}$$

In Fig. 2, ΔSWE is plotted against $\Delta\Phi_s$ for an incidence angle of $\Theta = 34°$ for different frequencies. The used frequencies are in X-band 9.65 GHz, in C-band 5.41 GHz and in L-band 1.26 GHz. It can be seen that the ΔSWE estimation has a strong dependence on the wavelength.

Moreover, since the DInSAR phase can only be used to calculate a SWE change between two acquisitions [see (3)], it just allows to monitor the differential SWE over time. The estimation of the total SWE requires a time series of measurements starting at snow-free conditions or an initial guess of SWE and a cumulative sum of the ΔSWE estimates.

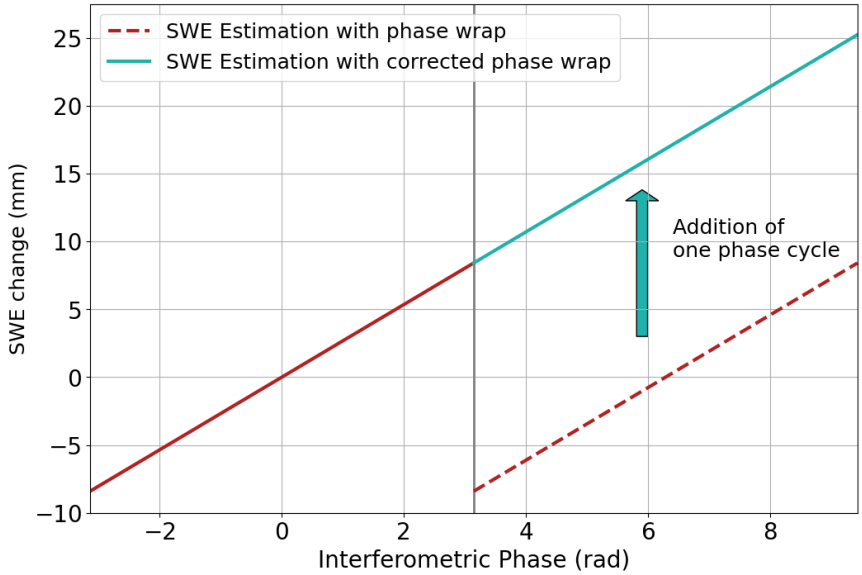

Fig. 3. SWE change in dependence of the interferometric phase. SWE change values above the phase wrap threshold suffer from phase wraps and will be underestimated (red dotted line), which can be corrected by adding a phase cycle (green line).

2.2.2 ΔSWE Estimation Threshold Due to Phase Wrapping

It has to be taken into consideration that only a limited range of ΔSWE can be retrieved unambiguously using (3) since the differential interferometric phase can be only measured in an interval between $[-\pi, \pi]$. An example for X-band is shown in Fig. 3 for an incidence angle of $\Theta = 34°$. The solid line represents the interval $[-\pi, \pi]$, which corresponds to a range of SWE changes of [-8.37 mm, 8.37 mm]. This is the interval which can be estimated unambiguously. For higher ΔSWE, the phase would exceed π. However, in that case, the phase wraps again to -π. Therefore, the results for ΔSWE values which would correspond to $\Delta\Phi_s$ values in the interval [π,3π], are the same as for the interval $[-\pi, \pi]$. The same occurs when a ΔSWE decrease exceeds the negative threshold of the interval.

The interval, in which ΔSWE values can be retrieved unambiguously, strongly depends on the wavelength and is approximately seven times larger for L-band than for X-band. Fig. 4 shows the upper boundary of this ΔSWE interval (before phase wrapping occurs) at X-, C- and L-band in dependence of the incidence angle. The interval generally decreases with larger incidence angles as the path length of the radar wave in the snow pack increases. Because ΔSWE values exceeding this interval result in phase wraps of $\Delta\phi_s$, they need to be detected and compensated for a correct ΔSWE estimation.

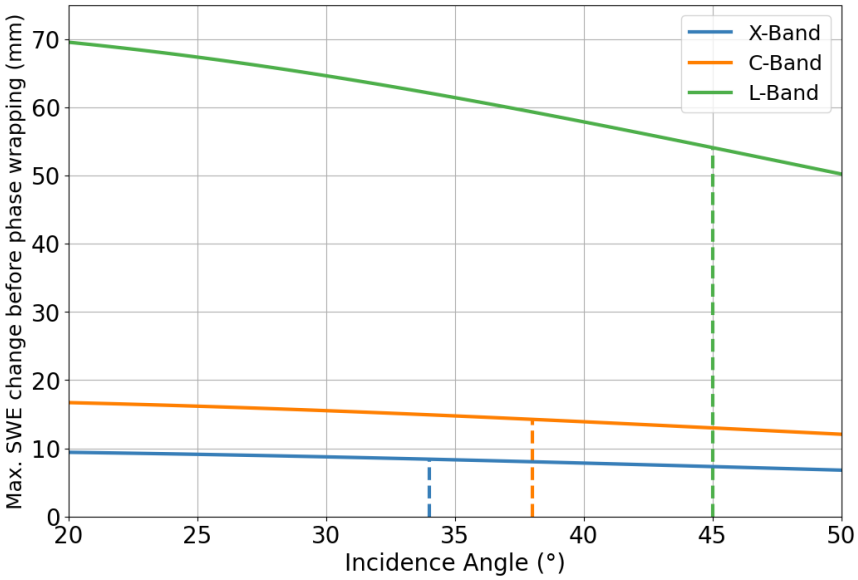

Fig. 4. SWE change between two acquisitions for a phase difference $\Delta\Phi_s = \pi$ in dependence of the incidence angle for X-, C- and L-band. Higher SWE changes suffer from phase wrapping. The equivalent thresholds apply for negative changes. The vertical lines indicate the incidence angles of the satellite data used in this study (blue: TanDEM-X, orange: Sentinel-1, and green: ALOS-2).

2.2.3 Ground-Based and Multifrequency DInSAR Phase Correction for ΔSWE Estimations

For the investigation of the phase wrapping issue, ground measurements of ΔSWE are used in this study to correct for phase wraps. It is assumed that the retrieved phase values suffer from phase wrapping errors in cases where the ground-based measurements lie outside the above-mentioned interval. The results are then corrected by adding a full phase cycle, as indicated by the green line in Fig. 3. This enables the retrieval of ΔSWE values outside of $[-\pi, \pi]$. The ground measurements also may contain measurement errors. Therefore, for ground measurements within +/- 5% of the boundary of the interval, it is checked whether a phase wrap correction needs to be applied in order to improve the results.

Another way to correct the phase wraps is a multifrequency approach, exploiting the fact that long wavelength measurements are less affected by phase wraps. In this study, ΔSWE estimates from SAR acquisitions with a longer wavelength (e.g. ALOS-2) are used to correct the ΔSWE estimates from shorter wavelength data (e.g. Sentinel-1). If the acquisitions are acquired at different dates, the SWE change estimates from the longer wavelength are linearly interpolated between the measurement dates. Phase wraps of the shorter wavelength data are corrected as follows. When the SWE change estimates including the standard deviation of the longer wavelength measurements are below the phase wrap threshold, no correction is performed. In the case that the threshold lies within the standard deviation of the SWE change estimate of the longer wavelength, it is calculated if adding a phase cycle decreases the difference between the SWE

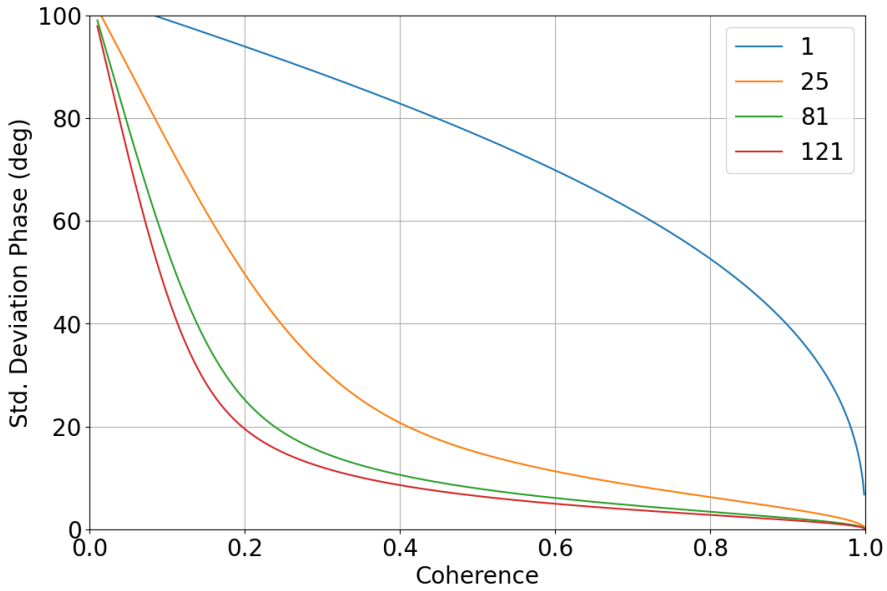

Fig. 5. Standard deviation of the phase in dependence of the coherence for $N = 1; 25; 81;$ and 121 samples. It can be observed, that the standard deviation decreases for higher coherence values and larger number of looks.

change estimates of the two frequencies. If so, a phase cycle is added. In the case that the SWE change estimate including the standard deviation lies above the threshold, a phase cycle is added.

2.2.4 *ΔSWE* Deviation Due to Phase Standard Deviation in Dependence of the Coherence

The interferometric phase is estimated from N interferogram samples to reduce phase noise. The probability density function pdf of the phase Φ is given by [30]

$$pdf(\Phi, N) = \frac{\Gamma\left(N+\frac{1}{2}\right)(1-|\gamma|^2)^N|\gamma|\cos(\Phi - \Phi_0)}{2\sqrt{\pi}\Gamma(N)(1-|\gamma|^2\cos^2(\Phi-\Phi_0))^{N+\frac{1}{2}}} + \frac{(1-|\gamma|^2)^N}{2\pi} 2F_1\left(N, 1, \frac{1}{2}, |\gamma|^2\cos^2(\Phi - \Phi_0)\right) \quad (4)$$

where γ is the complex coherence (see Section 2.3.3). The pdf is used to calculate the standard deviation of the phase in dependence of the coherence for different numbers of samples (i.e. looks). As can be seen in Fig. 5, the phase standard deviation significantly decreases for a higher number of samples.

Since the SWE change is calculated using the interferometric phase, the phase standard deviation can be converted into a ΔSWE estimation error with (3). The ΔSWE estimation errors for different frequencies are displayed in Fig. 6 for 1 and 81 looks. Since the error is proportional to the frequency, the ΔSWE estimation error is higher for the L-band than for the X-band.

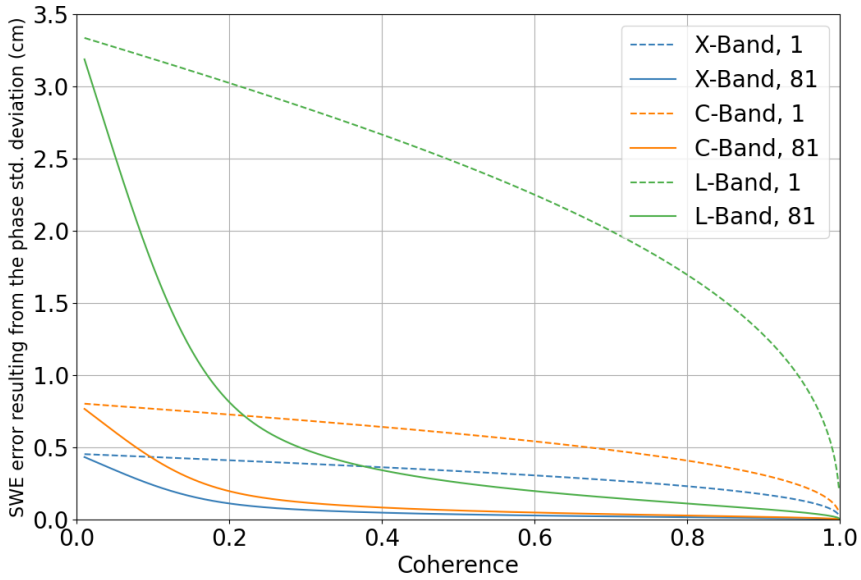

Fig. 6. ΔSWE error resulting from the standard deviation of the phase for X-, C-, and L-bands. For each band, the results for 1 and for 81 samples in a multilook window are compared. The obtained ΔSWE error is proportional to the frequency.

2.3 Experimental Data

2.3.1 SAR Data

A list of the utilized SAR data can be found in Table I.

The TanDEM-X (TDX) data set contains a time series for the winter 2010-2011 acquired in strip map mode. X-band data in VV and VH polarisations are available with a temporal baseline of 11 days. The incidence angle is 34°.

TABLE I
SATELLITE ACQUISITIONS

Satellite (frequency)	Dates		Incidence angle	Channel	Applied Multilook (rgxaz)
TDX (9.65 GHz)	2010-10-25 – 2011-03-17	Every 11 days	34°	VV, VH	9x9
Sentinel-1 (5.41 GHz)	2019-11-06 – 2020-03-17	Every 6 days	38°	VV, VH	7x3
ALOS-2 (1.26 GHz)	2019-12-30 – 2020-03-21	Every 14 days	45°	HH, HV	5x5

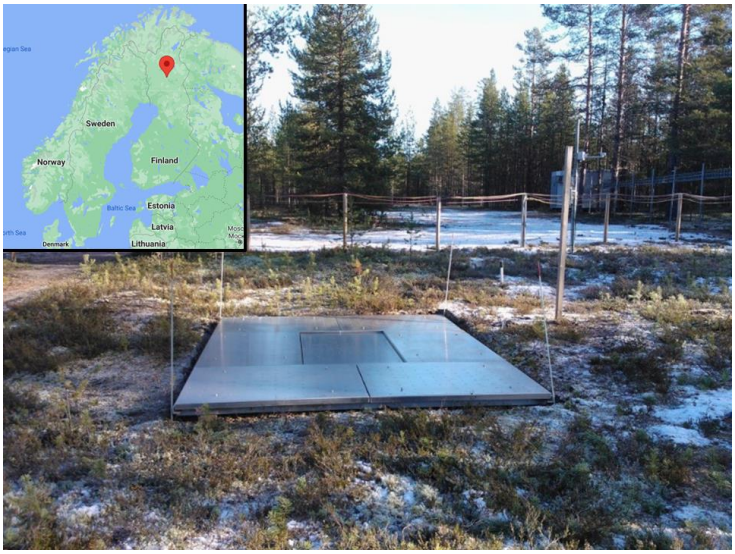

Fig. 7. Snow scale that measures the SWE of the snow pack at the IOA [31] with location on the map. The accumulated snow is weighted over the center plate.

To investigate C-band, Sentinel-1 data were chosen for the winter 2019-2020. Because there were two polar orbiting satellites, a repeat-pass time of 6 days can be achieved. The polarisations are VV and VH, with an incidence angle of 38°.

Additionally, ALOS-2 acquisitions in L-band are also available from the winter 2019-2020 with a temporal resolution of 14 days. HH and HV were acquired with an incidence angle of 45°.

Here, it has to be considered that due to data availability, the X-band data was acquired 9 years before the C- and L-bands data. However, the months which are covered are similar. Furthermore, due to the higher backscatter and coherence, the co-pol channel, either VV or HH, was used in this study.

2.3.2 Ground Data and Test Site

The Arctic Space Observation Centre lies close to the city of Sodankylae in northern Finland; see Fig. 7. The intensive observation area (IOA; N67.36183, E26.63415) is a test site where ground measurements are performed. It is located in a forest opening that is surrounded by a pine forest with about 15m high trees. The area is flat and lies approximately 175 m above sea level.

In the winter 2010-2011 manual measurements of snow properties, like SWE, depth and temperature were performed at the IOA. The measurement dates are not more than 3 days apart from the satellite acquisitions, and are therefore used for the validation of the satellite data.

Since 2015, daily automated SWE measurements [31] are performed using a snow scale at the IOA, where the snow accumulation is weighted over a centre panel (see Fig. 7). Weather parameters (i.e. temperature, snow depth, wind speed) are provided by an automated weather station (AWS) [32].

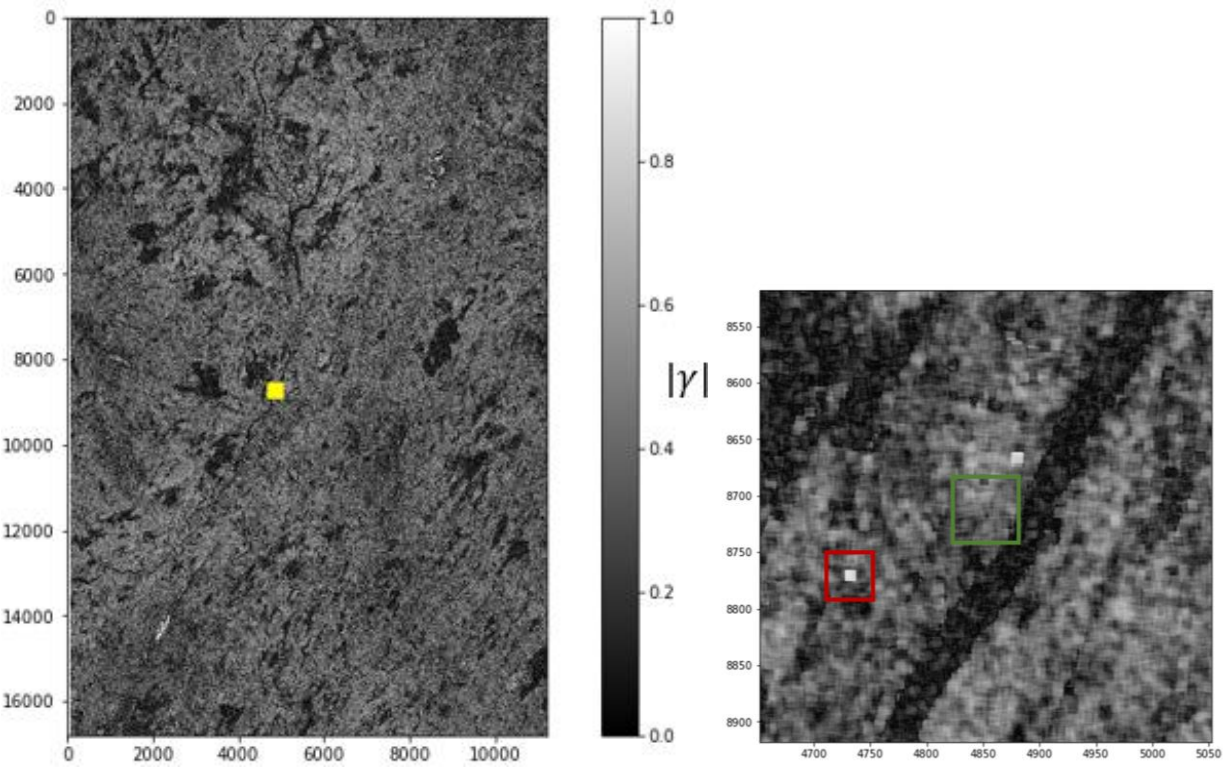

Fig. 8. Coherence of the HH channel for the L-band acquisition on the 09.03.2020/23.03.2020 in range and azimuth coordinates. (a) For the total SAR scene. The area of the test site is marked in yellow. (b) Zoom in to the test site. The test site and the calibration point are marked with green and red, respectively.

2.3.3 Interferometric Processing

The satellite radar data is processed using the TanDEM-X Interferometric processor (TAXI) by German Aerospace Center [33], which is adapted to ALOS-2 and Sentinel-1, for which the InSAR processing is performed on a burst by burst basis. For all satellites, the reference and secondary images were geometrically co-registered by using a DEM and orbit information, common band filtering was applied and the flat earth phase was compensated.

The complex coherence γ is calculated between two nearest-neighbor (consecutive) acquisitions, either for the VV or for the HH channel, with the shortest temporal baseline possible, using the cross correlation of both signals with

$$\gamma = \frac{\langle s_1 s_2^* \rangle}{\sqrt{\langle s_1 s_1^* \rangle \langle s_2 s_2^* \rangle}} \tag{5}$$

where s_1 and s_2 are the signals of the reference and secondary images, respectively, and $\langle \dots \rangle$ represents the expectation value. Appropriate multilooking is required to achieve sufficient theoretical ΔSWE estimation performance (see Section 2.2.4). The multilooking windows for the different frequencies can be found in Table I and are adapted to match the forest opening of the IOA.

One example of the L-band HH interferometric coherence $|\gamma|$ is shown in Fig. 8(a) for the image pair of the 09.03.2020 and 23.03.2020. Particularly low coherence values correspond to lakes and rivers. Fig. 8(b) shows a zoom in to the test site marked with green. In general, coherences are rather low, showing the challenging DInSAR scenario due to the large temporal baselines.

The interferometric phase is calculated from the coherence between the two acquisitions and the flat earth phase is removed. To obtain only the phase contribution from the snow pack, any atmospheric phase contributions have to be removed. This is achieved by a phase calibration at a stable scatterer in the vicinity of the test site. Due to the lack of proper calibration targets, a stable scatterer is identified by finding a resolution cell with particular high and temporally stable backscatter and coherence. The high coherence of the stable scatterer, corresponding to buildings, and its location near the test site is marked in red in Fig. 8(b) for an L-band example. More sophisticated atmospheric phase calibration methods, like, for example, [34] and [35], were investigated but failed due to the generally low coherence in the data.

2.4 Results

2.4.1 ΔSWE Estimation X-Band

The temperature and SWE data are displayed in Fig. 9 for the dates of the TDX acquisitions. Except for the first acquisition date, the temperature was below zero degrees and the SWE was increasing.

The time series of the coherence for the VV channel over the test site is displayed in Fig. 10. It shows that the coherences are rather small, but are especially low between the 19.12.2010 and 30.12.2010 and between the 30.12.2010 and 10.01.2010 reaching values below 0.2. The comparison with the ground measurements (see Fig. 9) reveals that for these measurements especially high temperature gradients were encountered. Including the only negative SWE change in the time series, this might explain the small coherences as a larger change in snow structure can be expected [36].

After calculating the coherence and the interferometric phase, (3) is applied for the ΔSWE estimation. Fig. 11(a) shows the ΔSWE ground measurements and the DInSAR-retrieved SWE changes between the acquisition dates. Since only SWE differences between two acquisitions can be retrieved from the ΔSWE estimation model, the values would have to be added over time to obtain a total SWE. However, a large discrepancy between the retrieved and measured SWE changes can be observed with an RMSE before the correction of phase wraps of $RMSE_{b,X}$ =13.12mm.

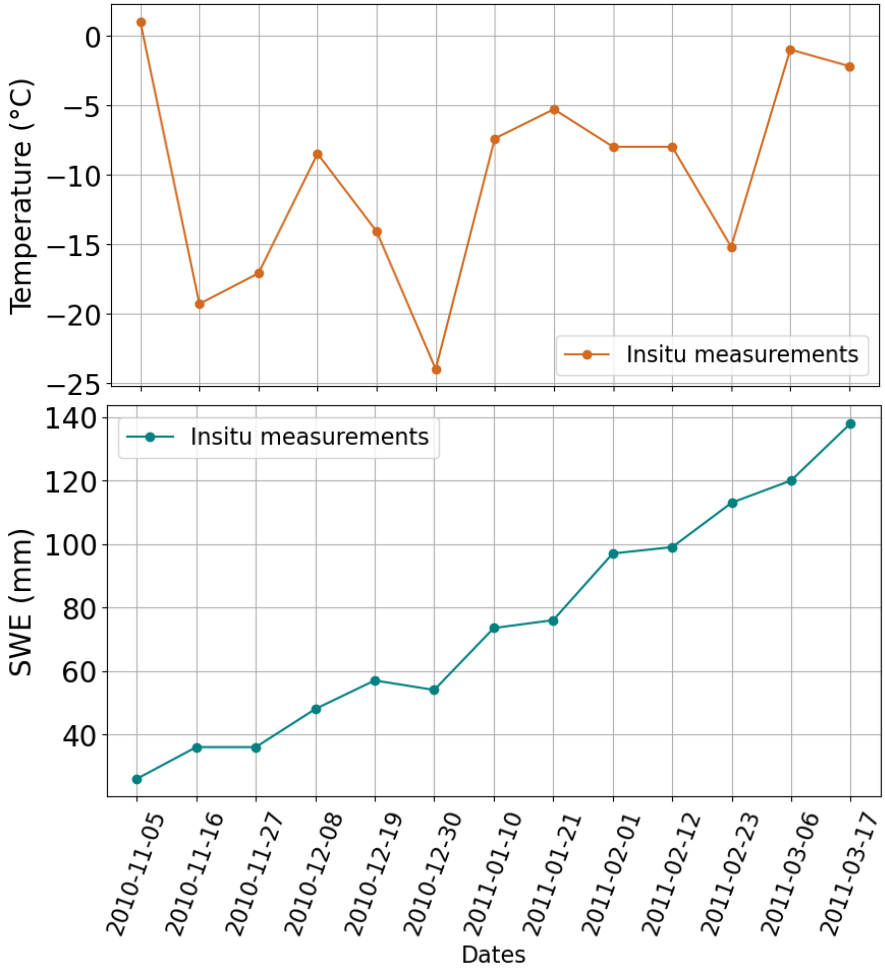

Fig. 9. (a) Air temperature and (b) Total SWE measurements at the TanDEM-X acquisition dates.

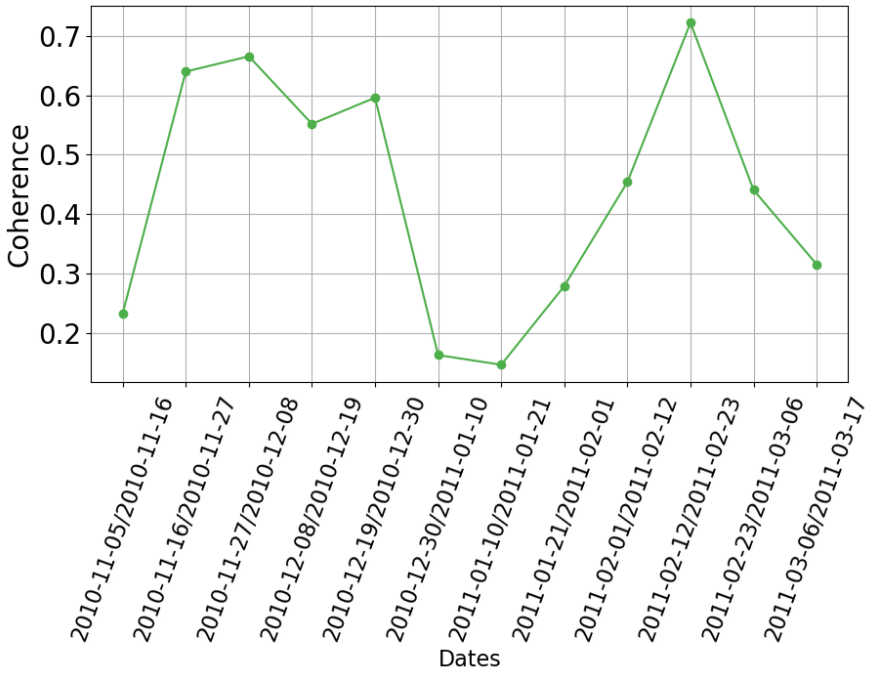

Fig. 10. Coherence for the X-band data. In the x-axis labels, the first date represents the reference acquisition and the second date the secondary acquisition of the interferogram.

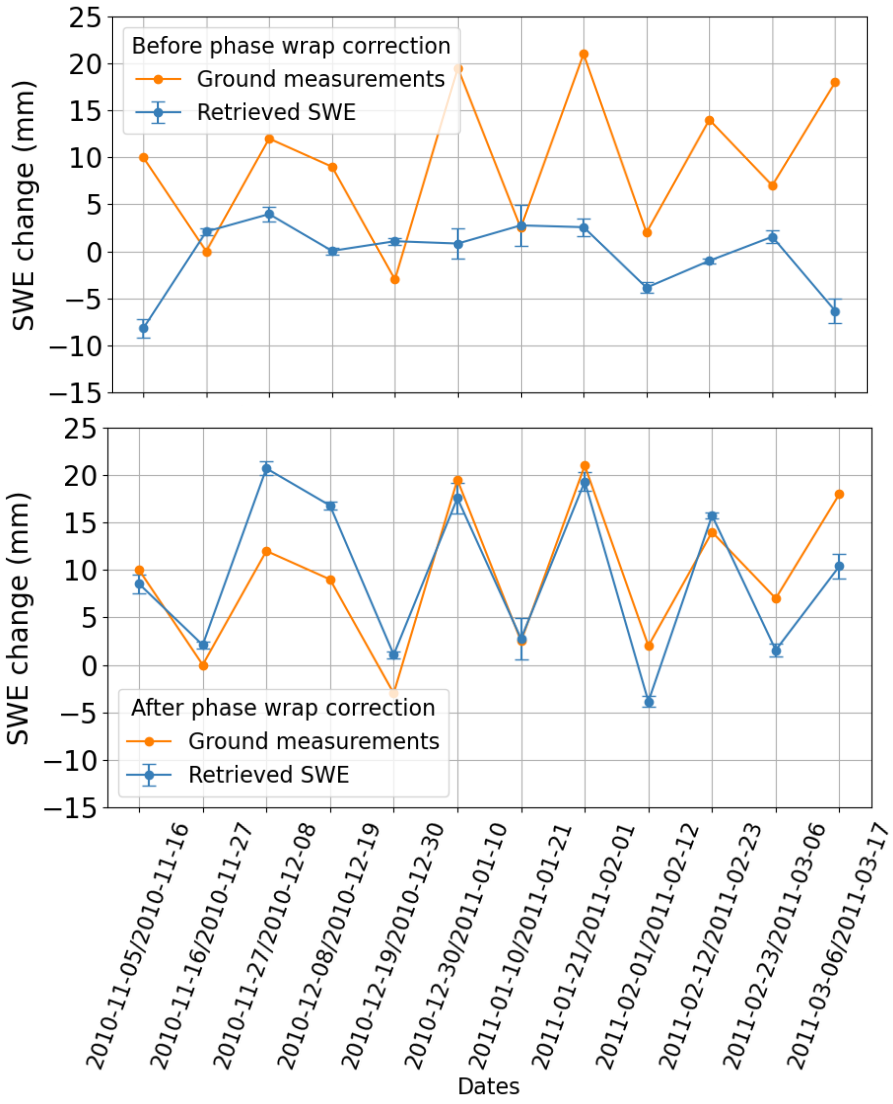

Fig. 11. Ground measured and from X-band data retrieved SWE change values. (a) Before phase wrap correction. (b) After phase wrap correction using the ground measurements.

As mentioned, since the DInSAR phase lies in a range between $[-\pi, \pi]$, SWE differences outside this interval cannot be retrieved from the satellite data due to phase wrapping. For the used frequency and incidence angle that interval corresponds to a SWE change in the range of [-8.37 mm, 8.37 mm]. The upper boundary is marked with a blue vertical line in Fig. 4. After using the ground measurements to detect phase wraps and to correct these by adding the appropriate amount of phase cycles, the ΔSWE estimations displayed in Fig. 11(b) are obtained, showing a better correlation between the measured and retrieved ΔSWE values with a RMSE after correction of $RMSE_{a,X}$=4.92 mm. There are some discrepancies, but the general trend is well represented with the retrieved and corrected ΔSWE values. Since the phase wrap correction has a big impact on the results particularly for short wavelengths, we calculated the RMSE relative to a full phase cycle (i.e. the ΔSWE change which corresponds to 2π phase) to have a better comparison between

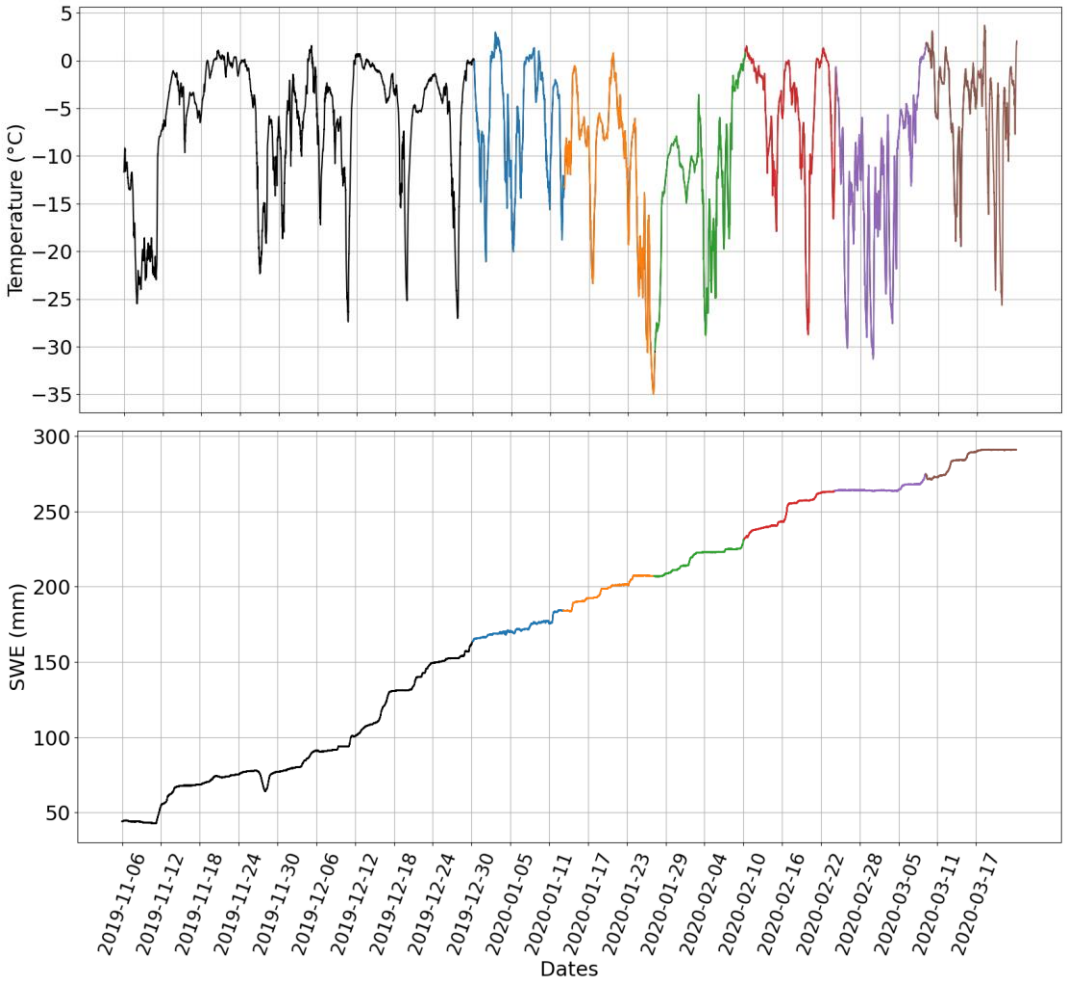

Fig. 12. (a) Air temperature and (b) total SWE measurements. The vertical grid lines correspond to the Sentinel-1 acquisitions. The colors mark the 14 days temporal baseline between the ALOS-2 acquisitions

frequencies, which is discussed in Section 2.4.4. Without the phase wrap correction, it is not possible to retrieve the SWE change correctly in this case because the ground measurements show that the threshold for phase wraps is often exceeded.

Therefore, it is important to correct for phase wraps when performing the ΔSWE retrieval using DInSAR X-band data with a temporal baseline of 11 days.

2.4.2 ΔSWE Estimation C-Band

In Fig. 12, the temperature and the total amount of SWE for the winter 2019-2020 are displayed. The vertical grid lines represent the 6 days between the Sentinel-1 acquisitions. Overall it can be seen, that for both investigated winters in this study, the SWE is almost steadily increasing, but especially in the 2019-2020 winter, the temperatures were sometimes above zero degrees.

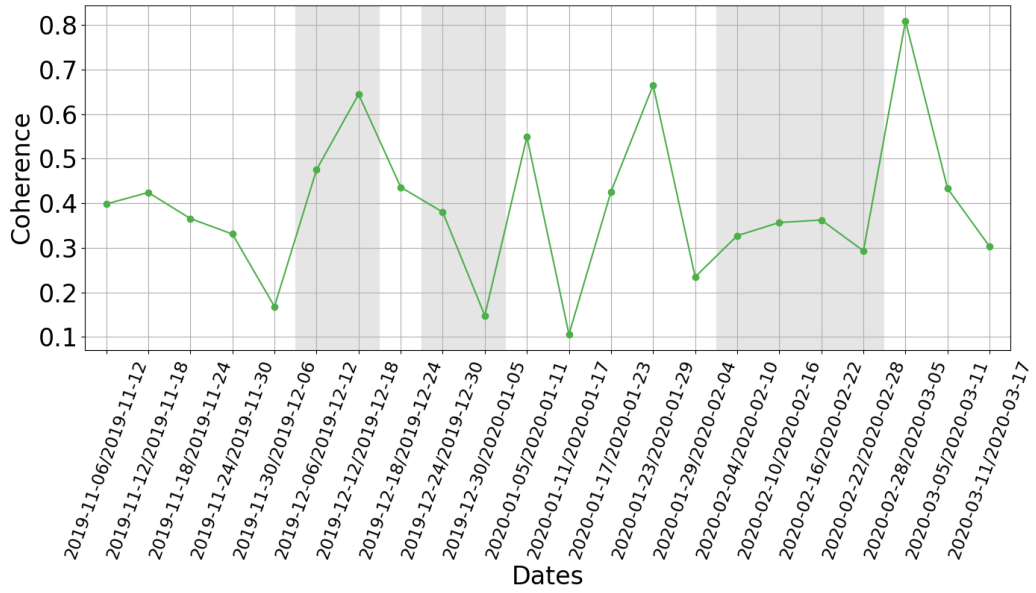

Fig. 13. Coherence for the C-band data. In the x-axis labels, the first date represents the reference acquisition and the second date the secondary acquisition of the interferogram. The gray background marks the measurements where the temperature was above zero degrees either at the first or second acquisition of the interferogram.

The coherences for the VV polarized C-band data are displayed in Fig. 13. In many cases, the coherences are very low. The coherences can be compared to the temperature data in Fig.12. It can be seen that in many cases, the air temperature rises above zero degrees likely resulting in snow melt, which causes the low coherences. The gray background colors mark the measurements where the temperature was above zero degrees either at the first or second acquisition of the interferogram. However, the coherence can also decrease if the temperature was above zero degrees between the acquisitions and the snow pack refroze again, resulting in a refrozen melt layer which might contribute to the backscattering and thus bias the ΔSWE retrieval. This may have been the cause for the low coherence 30.11.2019/06.12.2019.

The ΔSWE retrieval is also applied to the interferometric phase of the Sentinel-1 acquisitions. Note that in this case the investigated winter is 2019-2020, and thus, differs from the X-band estimations.

The interval in which the SWE change can be retrieved unambiguously is [-14.32 mm, 14.32 mm] (orange vertical line in Fig. 4). Fig. 14(a) shows the SWE differences for temporal baselines of 6 days with a RMSE before correction of $RMSE_{b,C}$ = 13.47 mm. Also here, the ground-measured SWE changes often exceed the phase wrap threshold and therefore the missing phase cycles need to be corrected. The obtained results are displayed in Fig. 14(b). The RMSE between the ground measurements and retrieved SWE changes is $RMSE_{a,C}$= 9.46 mm after correction. Although some similarities can be observed for the general trend, in many cases, the discrepancy is very high. A possible reason here may be again large temperature gradients, as, for example, on the 18.12. /24.12.2019 or the 23.01/29.01.2020 when a larger snow structure change can be expected which can have a not yet fully understood effect on the phase [24]. Another possible reason for that might be the positive temperature which occurred many times throughout the time series. This

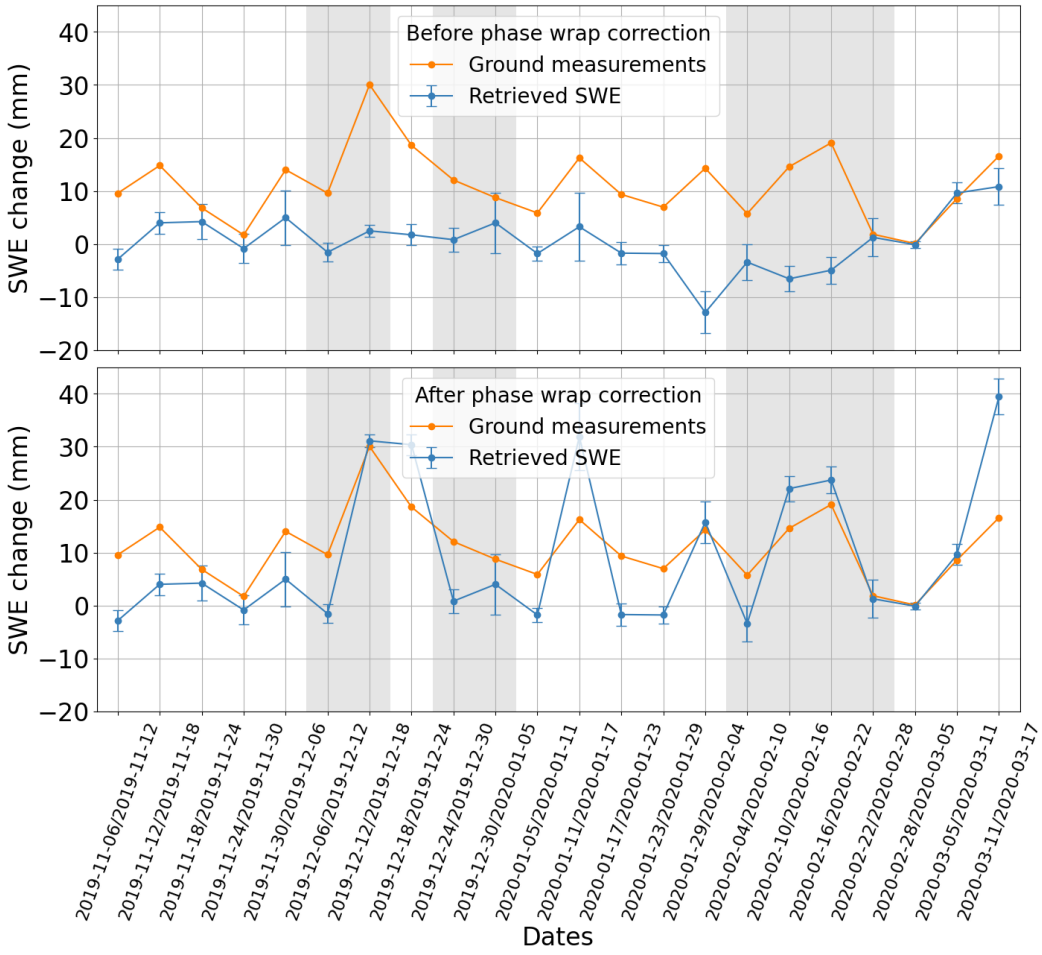

Fig. 14. Ground measured and from C-band data retrieved SWE change values. (a) Before phase wrap correction. (b) After phase wrap correction using the ground measurements. The gray background marks the measurements where the temperature was above zero degrees either at the first or second acquisition of the interferogram.

causes not only low coherences, resulting in large phase standard deviations, and thus, ΔSWE estimation errors, but also in potential systematic errors. Due to the resulting snowmelt, the radar wave will get attenuated in the snow pack [37] and is not able to penetrate to the ground when the temperature is above zero degrees at the acquisition time. This may be the reason for the following discrepancies: for the underestimations, because less snow is propagated by the radar wave, but it might be also seen as an overestimation in the plot, in case where the snow was significantly underestimated and the measured phase is, therefore, one phase cycle off. This shows, that the selected winter season, which was chosen due to its coincidence with the available ALOS-2 data, was not optimal due to the weather conditions. However, it is also clear that the phase wrapping issue plays an important role in the ΔSWE estimations using C-band data with a temporal baseline of 6 days. Nonetheless, some general trends can be represented with the retrieved SWE change.

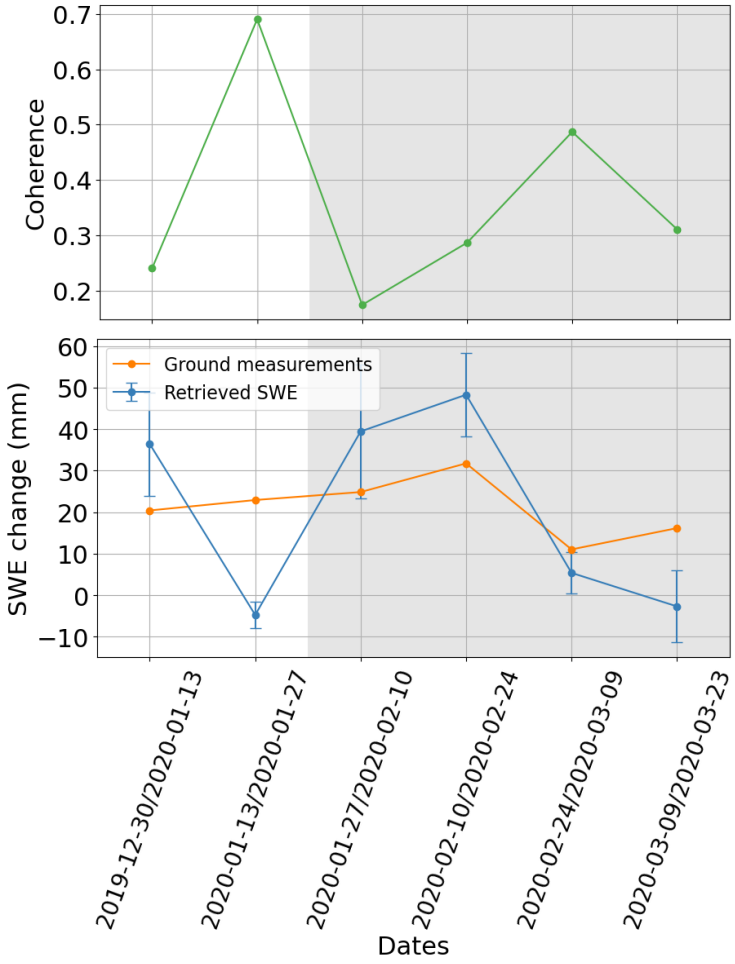

Fig. 15. (a) Coherence for the L-band data. In the x-axis labels, the first date represents the reference acquisition and the second date the secondary acquisition of the interferogram. (b) Ground measured and from L-band data retrieved SWE change values. The gray background marks the measurements where the temperature was above zero degrees either at the first or second acquisition of the interferogram.

2.4.3 *ΔSWE* Estimation L-Band

The ground measurements for the ALOS-2 acquisitions are also displayed in Fig. 12, which cover roughly the second half of the temporal coverage of Sentinel-1. The colours mark the 14 days temporal baseline between the dates of the ALOS-2 acquisitions.

Fig. 15(a) shows the ALOS-2 L-band coherences in the HH polarization. The coherences are often very low over the test site. Here, the same winter as for C-band was investigated. As it can be seen in Fig. 12, the temperatures at the acquisition times were often above zero degrees, causing low coherences as a result of snow melt.

For the ALOS-2 wavelength and incidence angle the calculated threshold for phase wrapping is outside the interval of [-54.4 mm, 54.4 mm]. This is always larger than the ground measured SWE changes. Therefore, phase wrap corrections do not have to be considered for the L-band data. The results for the ΔSWE retrieval are shown in Fig. 15(b) with the RMSE between the

retrieved and measured SWE change being $RMSE_{b,L}$ = 17.76 mm. Since it is the same winter as for the C-band measurements, the temperatures above zero degrees (Fig. 12) are a problem again. The general trend can be represented, but especially the second measurement point has a high discrepancy between the estimated ΔSWE from the ALOS-2 data and the ground measurements and the discrepancy is even higher than for the following interferograms, where the coherence was lower and the temperature higher. For this point, the temperature decreases by 35°C in the week before the second acquisition after being shortly above zero degrees. This high temperature gradient may have some influence on the snow structure. In [24], a decorrelation was observed for high temperature gradients, which may also be linked to changes in the snow properties. However, these effects need to be analyzed more, since this ALOS-2 interferogram has an unusually high coherence. Even if the snow cover can be seen as an isolating layer, high temperature changes may also have an influence on the ground. Since L-band measurements are also able to penetrate into frozen ground [38], this might also affect the interferometric phase.

2.4.4 Comparison of ΔSWE Estimation From Different Frequencies

The results of the different frequencies are compared directly in a scatter plot showing every SWE change estimation. Fig. 16(a) shows the estimated SWE changes compared to the ground measured values before phase wrap correction. Many points are underestimated, especially for the small wavelengths of X- and C-bands. This results from the smaller nonambiguous phase interval of retrievable SWE changes for shorter wavelengths.

After phase wrap correction, the results in Fig. 16(b) are obtained. The highest improvement can be observed for X-band. This underlines the fact that, for X-band SAR measurements, phase wraps of the interferometric phase after a SWE increase are important to correct for the used temporal baseline. For the X-band, the phase wrap correction has a large impact compared to the relatively small interval of unambiguous ΔSWE estimates. Nevertheless, the small wavelengths can contribute to higher ΔSWE estimation accuracies than larger wavelengths, but are rather only applicable for shorter temporal baselines or in a multifrequency approach (see Section 2.4.6). For the C-band, the points where the phase wraps were corrected according to the ground measurements are now slightly overestimated. In the case of the L-band measurements, no phase wrap correction was necessary. Even though one clear outlier can be observed at L-band, related to strong temperature changes, other points represent well the general trend. In order to allow for a better comparison between the frequencies, for each frequency, a relative RMSE ($RMSE_{rel}$) is calculated, by setting the RMSE after correction in relation to the 2π phase cycle interval ($\Delta SWE_{2\pi\_Interval}$) with:

$$RMSE_{rel} = \frac{RMSE_a}{\Delta SWE_{2\pi_{Interval}}}, \tag{7}$$

TABLE II
RMSE PHASE WRAP CORRECTION FROM GROUND MEASUREMENTS

Frequency	X band	C band	L band
$RMSE_b$ (mm)	13.12	13.47	17.76
$RMSE_a$ (mm)	4.92	9.46	17.76
$RMSE_{rel}$	0.29	0.33	0.16

shown in Table II. The performance of the L-band retrieval shows a smaller $RMSE_{rel}$ compared to the X- and C-bands results, meaning that here the retrieval performed the best in relation to the phase wrap interval. The individual errors after correction are however smaller for shorter wavelengths. Therefore, the sensitivity to retrieve smaller changes is higher for smaller wavelengths, even though the overall results are better for longer wavelengths. Note here, that this comparison is not optimal, as different temporal baselines and different winters are compared.

Across all frequencies, it can be observed in Fig. 16(b) that smaller SWE changes are mostly underestimated, while higher SWE changes are mostly overestimated. A factor influencing the ΔSWE retrieval is the phase calibration (see Section 2.3.3). Since the reference point is not ideal, a random error in the phase calibration could have been induced. Furthermore, as it is not known whether the stable point was covered by snow or not, the reference phase might contain some signal delay due to snow. When calibrating the phase over the test site according to this reference, an underestimation can be expected. However, this disagrees with the overestimations for higher SWE changes. A reason for the general differences is the likely wet snow in C- and L-bands, resulting in discrepancies between the estimated and measured SWE changes (see Section 2.4.2)

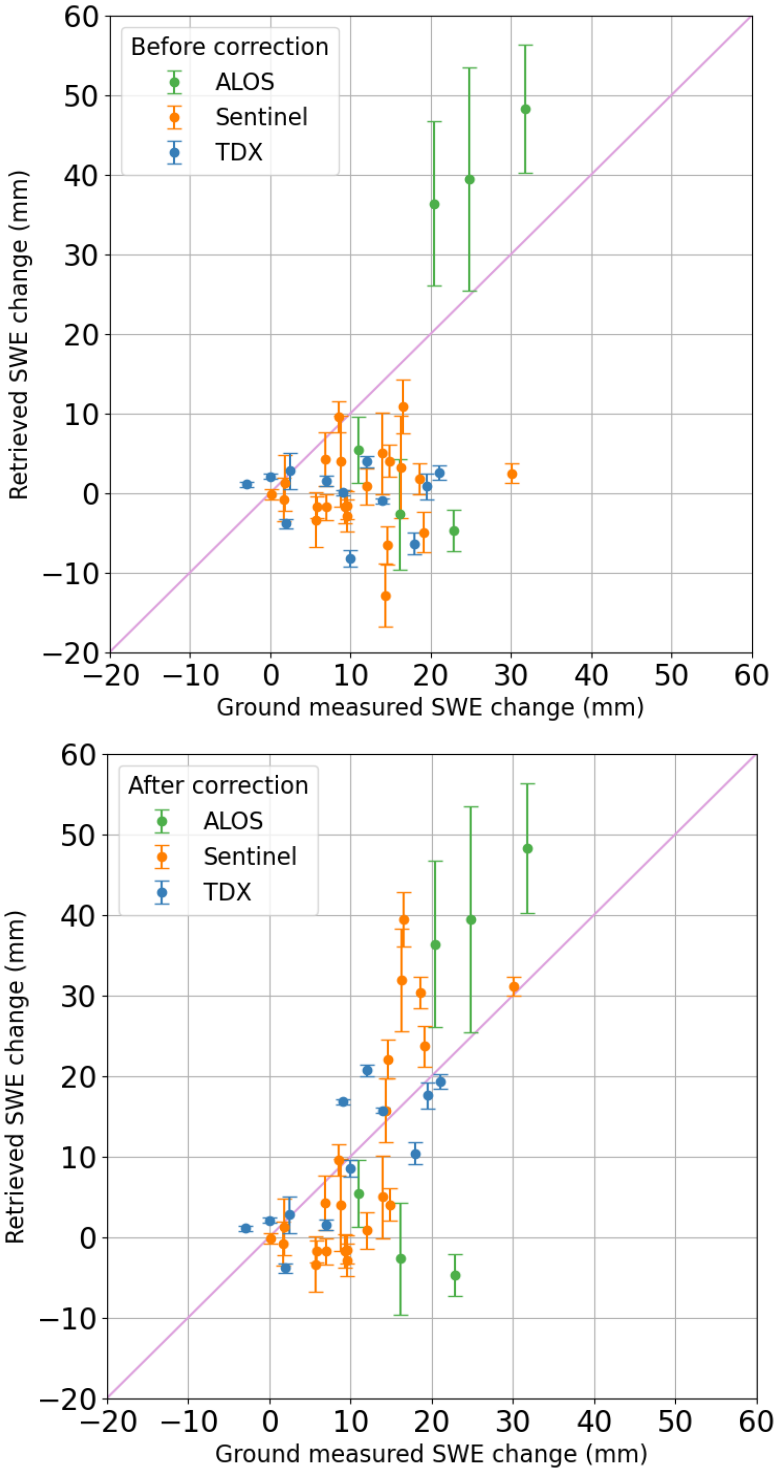

Fig. 16. Scatter plot of the retrieved SWE changes compared to the ground measured SWE changes for X-, C- and L-bands. (a) Before correcting the phase wraps based. (b) After correcting the phase wraps based on the ground measurements.

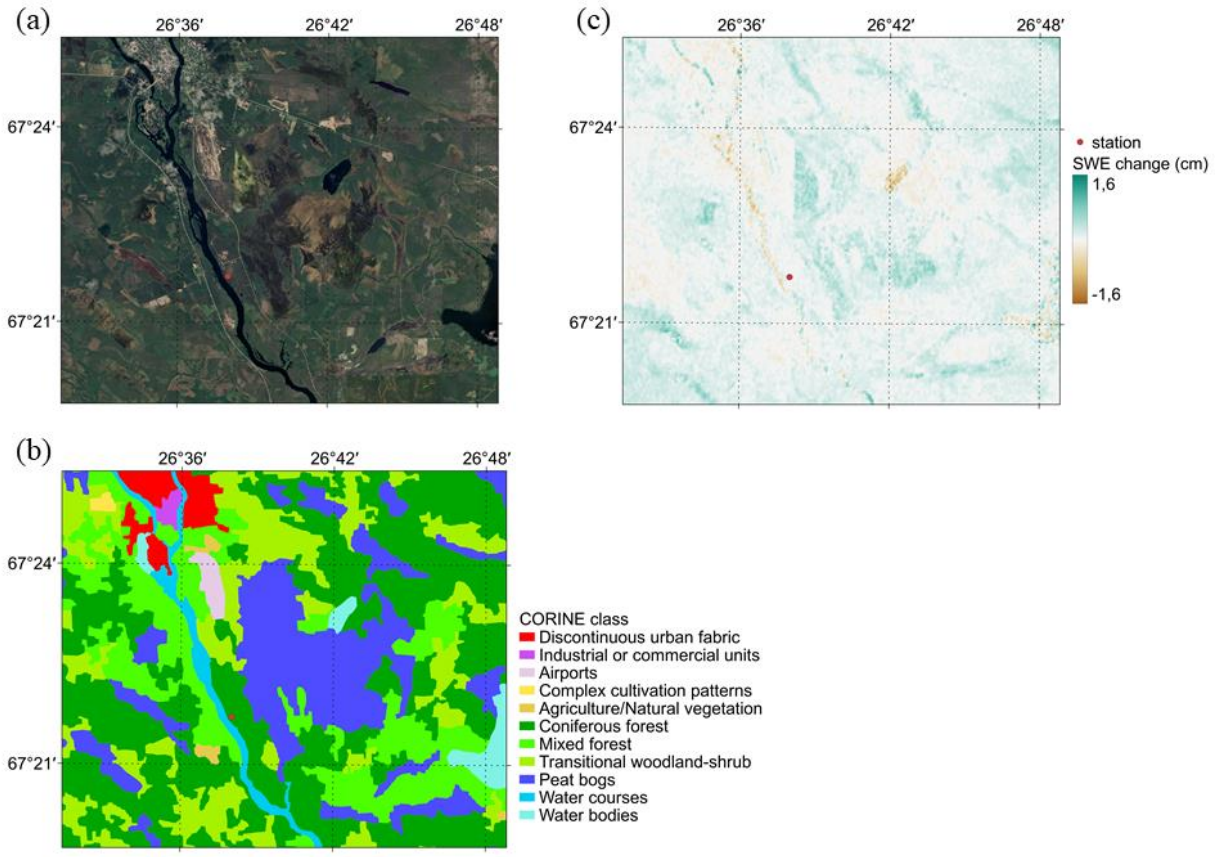

Fig. 17. Map of the area around the station. (a) Optical image. (b) CORINE landcover classes. (c) SWE change map from Sentinel-1 using the 28.02/05.03.20 interferogram. The red dot marks the location of the test site.

2.4.5 Spatial C-Band ΔSWE Estimation

For an assessment of the spatially distributed ΔSWE retrieval, with the potential for high spatial resolution and large-scale coverage with spaceborne SAR, the SWE change is estimated in the area around the in situ station. Fig. 17(a) shows an optical true-color image of the area and Fig. 17(b) displays the CORINE landcover information [39]. The area is mostly covered with forest and peat bogs, while the urban areas in the north belong to the town of Sodankylae. Fig. 17(c) displays the corresponding SWE change map of the area calculated from the Sentinel-1 interferogram between 28.03.20 and 05.03.20.

During this timeframe, the SWE remained stable at the in situ station. In the ΔSWE map, inland water bodies appear noisy as expected due to temporal decorrelation. Close to the in situ station, almost no SWE change is measured, which is in accordance with the ground measurements. The large peat bog in the center of the study area shows a noticeable positive ΔSWE. This may be due to the lower terrain which favors snow accumulation due to wind effects.

However, the phase signal which is measured might not only result from the SWE change, but also from the properties of the bogs. In the urban areas of Sodankylae, the SWE change has a tendency toward negative SWE change values with some variations. This may be the result from small-scale local SWE changes caused by anthropogenic structures. Further investigation is needed to analyze the influence of different land cover on the SWE change retrieval.

2.4.6 Multifrequency Phase Wrap Correction

Previously, ground measurements were used to correct the phase wraps of ΔSWE estimations in X-band (see Section 2.4.1) and C-band (see Section 2.4.2), as they suffer from phase wraps if the SWE change exceeds a certain threshold.

However, the goal is to correct the ΔSWE estimations without requiring ground measurements. This can be achieved using a multifrequency approach. In this study, the L-band data (see Section 2.4.3) are not affected by phase wraps because of its long wavelength. As the L- and C-bands data were acquired in the same winter, L-band ΔSWE estimates are used to detect and correct phase wraps in the C-band data. Due to the different acquisition dates and temporal baselines for the ALOS-2 and Sentinel-1 images, the retrieved SWE changes from ALOS-2 are linearly interpolated between the measurement dates. Fig. 12(b) shows that it is reasonable to assume a linear SWE change. Then, the interpolated SWE change from the L-band measurements is used to detect where a phase cycle needs to be added to the C-band ΔSWE estimations. By correcting the C-band values accordingly, the results in Fig. 18 are obtained with an RMSE after multifrequency phase wrap correction of $RMSE_{a,multi,C}$ = 10.09 mm, while the RMSE before correction for this interval was $RMSE_{b,multi,C}$ = 13.38 mm, which is the same as the single frequency $RMSE_{b,C}$ result, but only for the time span covered by the L-band data. Here, discrepancies can be observed with some clear overestimations in the middle of the time series, which are related to the L-band overestimations in Fig. 15. However, the error is only slightly larger than for the ground-based corrected C-band results in Fig. 14(b), which is $RMSE_{a,groundC,}$ = 9.66 mm, summarized in Table III. When comparing the ΔSWE results after phase wrap corrections from the multifrequency approach and the one from the ground measurements, seen in Fig. 14(b), 9 of the 13 ΔSWE estimates utilized for the multifrequency approach were corrected or not corrected in the same way. Furthermore, it has to be taken into consideration that the investigated winter was not optimal due to high temperatures and low coherences. However, this shows that L-band ΔSWE estimates can be used to correct phase wraps in smaller wavelength SAR measurements like C-band, because the L-band measurements are less likely to suffer from phase wraps. Even though the performance of this approach was not yet completely satisfying, due to the discrepancy of the L-band data to the ground measurements, this method is promising, because it enables the phase wraps correction without the need of additional ground measurements. This is essential for future large-scale space borne applications. Unfortunately, no winter exists where all three frequencies were acquired contemporaneously.

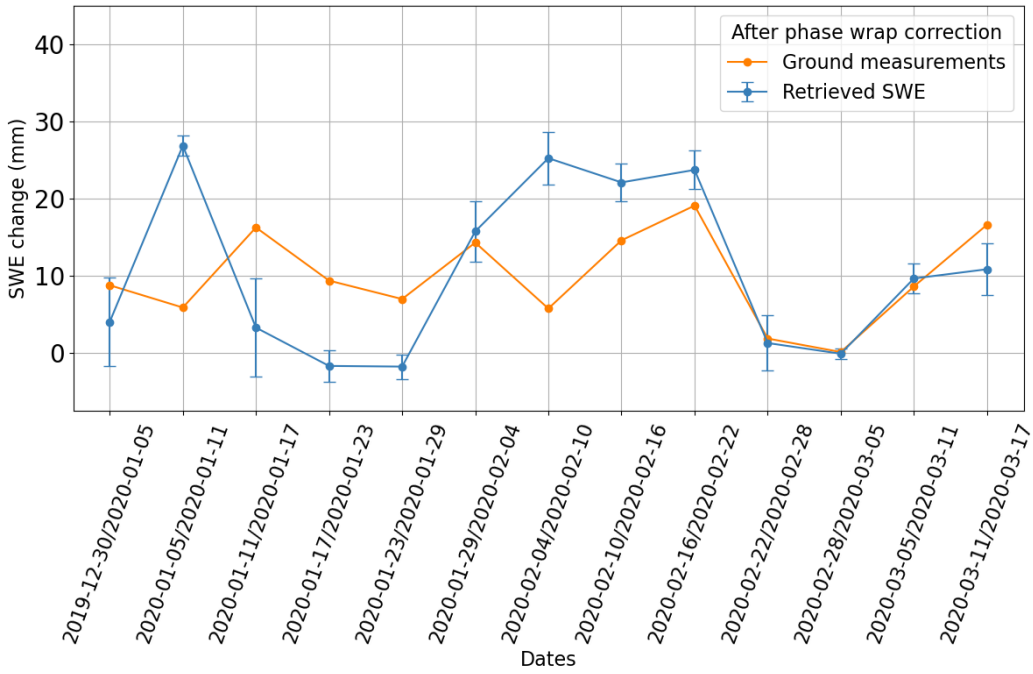

Fig. 18. Ground measured and from C-band data retrieved SWE change values. The phase wraps are corrected with the L-band SWE estimations.

TABLE III
RMSE MULTIFREQUENCY PHASE WRAP CORRECTION

Frequency	C band
$RMSE_{b,multi,C}$ (mm)	13.38
$RMSE_{a,multi,C}$ (mm)	10.09
$RMSE_{a,groundC}$ (mm)	9.66

2.5 Conclusion

The SWE change is retrieved using the DInSAR phase difference for X-, C- and L-bands. Since the interferometric phase lies in an interval between [-π, π], only a range of SWE change values can be retrieved unambiguously. For larger changes of SWE, phase wraps occur. To investigate the effect of the phase wrap errors, they are corrected with ground measurements in this study. Furthermore, a multifrequency approach is presented to overcome the necessity of ground measurements, which could pave the way towards a DInSAR SWE information product with spaceborne SAR.

At the X-band, the main limitation for the ΔSWE retrieval is the phase wrapping of the measured interferometric phase. Because of the short wavelength, the interval where the SWE change can be retrieved unambiguously is smaller compared to longer wavelengths, such as L-

band. This could be potentially overcome by using temporal baselines much shorter than 11 days in order to reduce the observed SWE change and in turn to minimize the occurrence of phase wraps.

For the C-band, with a temporal baseline of 6 days, the phase cycles also needed to be corrected, which improved the results. However, the remaining discrepancies result most likely from several short melt events during the observed winter.

When using L-band SAR data with a 14 days temporal baseline, the correction for lost phase cycles was not necessary, because the SWE change did not exceed the phase wrapping threshold. Here, the same winter was analyzed as for the C-band data, confirming the possible influence of high temperature gradients and melt events. Moreover, only a short time series was available, limiting the performance assessment. However, except for one distinct outlier, the general ΔSWE trend was reproduced by the L-band data.

Thus, when choosing a suitable frequency for ΔSWE estimations, it has to be considered that longer wavelengths can monitor higher SWE changes without the need to correct for phase cycles. However, if the phase wraps can be corrected, the ΔSWE estimation is more accurate at shorter wavelengths. This highlights the potential of multifrequency approaches.

In future studies, it would be advantageous to take simultaneous measurements at different frequencies, ensuring same weather and snow conditions. Also, identical temporal baselines between the measurements would increase the comparability of the results. Moreover, the choice of the test site is also very important. In this case, the test site was a small opening located in a forested area. Therefore, some trees in the multilooking window might have affected the resulting ΔSWE retrievals. Furthermore, also the weather conditions play an essential role. Here, especially in the winter analyzed in C and L-bands, the temperatures often exceeded zero degrees. This may have led to wet snow. Since the method relies on the fact that the radar wave propagates through the whole snow pack and wet snow may cause attenuation of the radar wave, this affects the estimation results. Therefore, areas with stable weather conditions below zero degrees would be preferable. The calibration of the interferometric phase also plays a crucial role for the ΔSWE estimation. In this study, a stable scatterer was found close to the test site. However, even if this stable scatterer had the highest backscatter and coherence in this region, it is not guaranteed that it was not covered by snow during the acquisition, which would also induce an effect on the interferometric phase. Therefore, a corner reflector close to the test field from which snow is regularly removed would be of advantage. Thinking about future spaceborne SAR applications, the phase calibration might be one of the most challenging points.

This study demonstrated the potential and limitations of SAR acquisitions with different frequencies to estimate SWE changes using the DInSAR phase. A promising multifrequency approach is presented to overcome some of the limitations. It combines ΔSWE estimates from two frequencies to correct the phase wraps without the need of ground measurements. This is particularly of interest for upcoming multifrequency SAR missions, like the dual-frequency L- and S-band NASA-ISRO SAR (NISAR) mission [40]. Another possibility will be the combination of Sentinel-1 with ROSE-L [41], allowing the combination of C- and L-bands measurements.

Further favorable aspects of ROSE-L and Sentinel-1 are the identical orbits and repeat-pass intervals and a short time interval between their acquisitions. These missions will enable the potential of multifrequency approaches for the estimation of SWE changes, exploiting the high sensitivity of high frequencies with the large non-ambiguous phase interval of smaller frequencies.

2.6 Acknowledgment

The authors would like to thank the Finnish Meteorological Institute for providing the ground-based measurements. They would also like to acknowledge Dr. Pau Prats (DLR) and Dr. Matteo Nannini (DLR) for their support with TAXI and the interferometric processing. Furthermore, they thank Andrea Pulella (DLR) for his help with providing the Sentinel-1 data.

2.7 References

[1] J. Cohen, "Snow cover and climate," *Weather*, vol. 49, no. 5, Art. no. 5, 1994, doi: 10.1002/j.1477-8696.1994.tb05997.x.

[2] S. Rahmstorf, "A new view on sea level rise," *Nat. Clim. Change*, vol. 1, no. 1004, pp. 44–45, Apr. 2010, doi: 10.1038/climate.2010.29.

[3] H.-O. Pförtner *et al.*, *IPCC, 2022: Climate Change 2022: Impacts, Adaptation, and Vulnerability. Contribution of Working Group II to the Sixth Assessment Report of the Intergovernmental Panel on Climate Change*. Cambridge, UK and New York, NY, USA: Cambridge University Press., 2022. [Online]. Available: doi:10.1017/9781009325844

[4] T. P. Barnett, J. C. Adam, and D. P. Lettenmaier, "Potential impacts of a warming climate on water availability in snow-dominated regions," *Nature*, vol. 438, no. 7066, pp. 303–309, Nov. 2005, doi: 10.1038/nature04141.

[5] S. Jörg-Hess, N. Griessinger, and M. Zappa, "Probabilistic Forecasts of Snow Water Equivalent and Runoff in Mountainous Areas*," *J. Hydrometeorol.*, vol. 16, no. 5, pp. 2169–2186, Oct. 2015, doi: 10.1175/JHM-D-14-0193.1.

[6] J. C. Comiso, "Satellite remote sensing of the Polar Oceans," *J. Mar. Syst.*, vol. 2, no. 3–4, pp. 395–434, Aug. 1991, doi: 10.1016/0924-7963(91)90044-U.

[7] A. Bartsch, J. Jansa, M. Schoner, and W. Wagner, "Monitoring of spring snowmelt with Envisat ASAR WS in the Eastern Alps by combination of ascending and descending orbits," in *Proc. Envisat Symposium 2007*, Montreux, Switzerland, Apr. 2007, pp. 23–27.

[8] R. Kelly, "The AMSR-E Snow Depth Algorithm: Description and Initial Results," *J. Remote Sens. Soc. Jpn.*, vol. 29, no. 1, pp. 307–317, 2009.

[9] M. Takala *et al.*, "Estimating northern hemisphere snow water equivalent for climate research through assimilation of space-borne radiometer data and ground-based measurements," *Remote Sens. Environ.*, vol. 115, no. 12, pp. 3517–3529, Dec. 2011, doi: 10.1016/j.rse.2011.08.014.

[10] R. L. Armstrong, A. Chang, A. Rango, and E. Josberger, "Snow depths and grain-size relationships with relevance for passive microwave studies," *Ann. Glaciol.*, vol. 17, pp. 171–176, 1993, doi: 10.3189/S0260305500012799.

[11] B. J. Vander Jagt, M. T. Durand, S. A. Margulis, E. J. Kim, and N. P. Molotch, "The effect of spatial variability on the sensitivity of passive microwave measurements to snow water equivalent," *Remote Sens. Environ.*, vol. 136, pp. 163–179, Sep. 2013, doi: 10.1016/j.rse.2013.05.002.

[12] D. Li, M. Durand, and S. A. Margulis, "Potential for hydrologic characterization of deep mountain snowpack via passive microwave remote sensing in the Kern River basin, Sierra Nevada, USA," *Remote Sens. Environ.*, vol. 125, pp. 34–48, Oct. 2012, doi: 10.1016/j.rse.2012.06.027.

[13] A. Moreira, P. Prats-Iraola, M. Younis, G. Krieger, I. Hajnsek, and K. P. Papathanassiou, "A tutorial on synthetic aperture radar," *IEEE Geosci. Remote Sens. Mag.*, vol. 1, no. 1, Art. no. 1, Mar. 2013, doi: 10.1109/MGRS.2013.2248301.

[14] H. Rott, "The analysis of backscattering properties from SAR data of mountain regions," *IEEE J. Ocean. Eng.*, vol. 9, no. 5, pp. 347–355, Dec. 1984, doi: 10.1109/JOE.1984.1145655.

[15] C. Màtzler, "Microwave sensors for measuring avalanche-critical snow parameters," *IAHS Publ*, vol. Avalanche Formation, Movement and Effects, no. 162, pp. 149–160, 1987.

[16] J. Zhu, S. Tan, J. King, C. Derksen, J. Lemmetyinen, and L. Tsang, "Forward and Inverse Radar Modeling of Terrestrial Snow Using SnowSAR Data," *IEEE Trans. Geosci. Remote Sens.*, vol. 56, no. 12, pp. 7122–7132, Dec. 2018, doi: 10.1109/TGRS.2018.2848642.

[17] L. D. Gregorio *et al.*, "SWE retrieval by exploiting COSMO-SkyMed X-band SAR imagery and ground data through a machine learning approach," in *Active and Passive Microwave Remote Sensing for Environmental Monitoring III*, F. Bovenga, C. Notarnicola, N. Pierdicca, and E. Santi, Eds., SPIE, 2019, pp. 38–48. doi: 10.1117/12.2550824.

[18] H. Rott *et al.*, "Development of Snow Retrieval Algorithms for CoReH2O– Graine Size Estimator," ESA ESTEC Contract 22830/09/NL/JC---CCN2, May 2013.

[19] S. Leinss, O. Antropov, J. Vehvilaeinen, J. Lemmetyinen, I. Hajnsek, and J. Praks, "Wet Snow Depth from Tandem-X Single-Pass Insar Dem Differencing," in *IGARSS 2018 - 2018 IEEE International Geoscience and Remote Sensing Symposium*, Jul. 2018, pp. 8500–8503. doi: 10.1109/IGARSS.2018.8518661.

[20] J. Shi and J. Dozier, "Estimation of snow water equivalence using SIR-C/X-SAR. I. Inferring snow density and subsurface properties," *IEEE Trans. Geosci. Remote Sens.*, vol. 38, no. 6, pp. 2465–2474, Nov. 2000, doi: 10.1109/36.885195.

[21] H. Lievens *et al.*, "Snow depth variability in the Northern Hemisphere mountains observed from space," *Nat. Commun.*, vol. 10, pp. 1–12, 2019, doi: 10.1038/s41467-019-12566-y.

[22] T. Guneriussen, K. A. Hogda, H. Johnsen, and I. Lauknes, "InSAR for estimation of changes in snow water equivalent of dry snow," *IEEE Trans. Geosci. Remote Sens.*, vol. 39, no. 10, pp. 2101–2108, Oct. 2001, doi: 10.1109/36.957273.

[23] S. Leinss, A. Wiesmann, J. Lemmetyinen, and I. Hajnsek, "Snow Water Equivalent of Dry Snow Measured by Differential Interferometry," *IEEE J. Sel. Top. Appl. Earth Obs. Remote Sens.*, vol. 8, no. 8, pp. 3773–3790, Aug. 2015, doi: 10.1109/JSTARS.2015.2432031.

[24] J. J. Ruiz *et al.*, "Investigation of Environmental Effects on Coherence Loss in SAR Interferometry for Snow Water Equivalent Retrieval," *IEEE Trans. Geosci. Remote Sens.*, vol. 60, pp. 1–15, 2022, doi: 10.1109/TGRS.2022.3223760.

[25] H. Li, Z. Wang, G. He, and W. Man, "Estimating Snow Depth and Snow Water Equivalence Using Repeat-Pass Interferometric SAR in the Northern Piedmont Region of the Tianshan Mountains," *J. Sens.*, vol. 2017, 2017, doi: https://doi.org/10.1155/2017/8739598.

[26] V. Conde, C. Nico, P. Mateus, J. Catalao, A. Kontu, and M. Gritsevich, "On the estimation of temporal changes of snow water equivalent by spaceborne SAR interferometry: a new

application for the Sentinel-1 mission," *J. Hydrol. Hydromech.*, vol. 67, no. 1, pp. 93–100, 2019, doi: 10.2478/johh-2018-0003.

[27] P. N. Dagurov, T. N. Chimitdorzhiev, A. V. Dmitriev, and S. I. Dobrynin, "Estimation of snow water equivalent from L-band radar interferometry: simulation and experiment," *Int. J. Remote Sens.*, vol. 41, no. 24, pp. 9328–9359, Dec. 2020, doi: 10.1080/01431161.2020.1798551.

[28] A. T. Torun and S. Ekercin, "Estimating snow density, depth, volume, and snow water equivalent with InSAR data in the Erciyes mountain/Turkey," *Arab. J. Geosci.*, vol. 14, no. 15, p. 1456, Aug. 2021, doi: 10.1007/s12517-021-07873-y.

[29] A. Wiesmann and C. Mätzler, "Microwave Emission Model of Layered Snowpacks," *Remote Sens. Environ.*, vol. 70, no. 3, pp. 307–316, 1999, doi: https://doi.org/10.1016/S0034-4257(99)00046-2.

[30] R. Bamler and P. Hartl, "Synthetic aperture radar interferometry," *Inverse Probl.*, vol. 14, no. 4, pp. R1–R54, Aug. 1998, doi: 10.1088/0266-5611/14/4/001.

[31] Finnish Meteorological Institute, "Data from the Artic Space Centre." Accessed: Oct. 30, 2020. [Online]. Available: https://litdb.fmi.fi/ioa_snow-water-equivalent.php

[32] Finnish Meteorological Institute, "Data from the Artic Space Centre." Accessed: Oct. 30, 2020. [Online]. Available: https://litdb.fmi.fi/ioa0003_data.php

[33] P. Prats *et al.*, "Taxi: A versatile processing chain for experimental TanDEM-X product evaluation," in *2010 IEEE International Geoscience and Remote Sensing Symposium*, Honolulu, HI, USA: IEEE, Jul. 2010, pp. 4059–4062. doi: 10.1109/IGARSS.2010.5651002.

[34] A. Ferretti, C. Prati, and F. Rocca, "Permanent scatterers in SAR interferometry," *IEEE Trans. Geosci. Remote Sens.*, vol. 39, no. 1, pp. 8–20, Jan. 2001, doi: 10.1109/36.898661.

[35] P. Berardino, G. Fornaro, R. Lanari, and E. Sansosti, "A new algorithm for surface deformation monitoring based on small baseline differential SAR interferograms," *IEEE Trans. Geosci. Remote Sens.*, vol. 40, no. 11, pp. 2375–2383, Nov. 2002, doi: 10.1109/TGRS.2002.803792.

[36] S. Leinss, G. Parrella, and I. Hajnsek, "Snow Height Determination by Polarimetric Phase Differences in X-Band SAR Data," *IEEE J. Sel. Top. Appl. Earth Obs. Remote Sens.*, vol. 7, no. 9, pp. 3794–3810, Sep. 2014, doi: 10.1109/JSTARS.2014.2323199.

[37] H. Rott, T. Nagler, and R. Scheiber, "Snow Mass Retrieval by Means of SAR Interferometry," in *Proc. of FRINGE 2003 Workshop*, Italy, 2003.

[38] M. Schwank, M. Stahli, H. Wydler, J. Leuenberger, C. Matzler, and H. Fluhler, "Microwave L-band emission of freezing soil," *IEEE Trans. Geosci. Remote Sens.*, vol. 42, no. 6, pp. 1252–1261, Jun. 2004, doi: 10.1109/TGRS.2004.825592.

[39] "Corine Land Cover, Copernicus land monitoring service," 2018. Accessed: May 22, 2023. [Online]. Available: https://doi.org/10.2909/960998c1-1870-4e82-8051-6485205ebbac

[40] K. Kellogg *et al.*, "NASA-ISRO Synthetic Aperture Radar (NISAR) Mission," in *2020 IEEE Aerospace Conference*, Big Sky, MT, USA: IEEE, Mar. 2020, pp. 1–21. doi: 10.1109/AERO47225.2020.9172638.

[41] M. W. J. Davidson and R. Furnell, "ROSE-L: Copernicus L-Band Sar Mission," in *2021 IEEE International Geoscience and Remote Sensing Symposium IGARSS*, Brussels, Belgium: IEEE, Jul. 2021, pp. 872–873. doi: 10.1109/IGARSS47720.2021.9554018.

3 Combining Differential SAR Interferometry and Copolar Phase Differences for Snow Water Equivalent Estimation

K. Belinska, G. Fischer, and I. Hajnsek

IEEE Geoscience and Remote Sensing Letters

Published in vol. 21, pp. 1 – 5, Art no. 2001505, September 2024, DOI: 10.1109/LGRS.2024.3461229

This chapter is a post-print, differing from the published paper only in terms of layout and formatting.

The author's contributions:

- Interferometric processing of the SAR data.
- Implementation of the SWE retrieval algorithm.
- Conceptualization and implementation of the CPD phase wrap correction.
- Analysis and interpretation of the results.
- Writing of the manuscript.

The co-authors' contributions:

- G. Fischer and I. Hajnsek supervised the research.
- G. Fischer and I. Hajnsek contributed to the main ideas, the discussion of the results, and reviewed the manuscript.

COMBINING DIFFERENTIAL SAR INTERFEROMETRY AND COPOLAR PHASE DIFFERENCES FOR SNOW WATER EQUIVALENT ESTIMATION

Kristina Belinska[1,2], Georg Fischer[1], and Irena Hajnsek[1,2]
[1] German Aerospace Center, Microwaves and Radar Institute, Wessling, Germany
[2] ETH Zurich, Institute of Environmental Engineering, Zurich, Switzerland

Abstract

The amount of water in a snow pack can be described by the snow water equivalent (SWE). SWE is a crucial parameter for hydrological models, for example, for flood predictions. Previous studies have shown that the interferometric phase between two repeat-pass synthetic aperture radar (SAR) measurements can be used to determine the change in SWE. However, a limitation of this method is phase wraps. To overcome this, the copolar phase difference (CPD) between the VV and HH channel can be used, which has been proven to be related to the depth of freshly accumulated snow.
This study proposes an approach to incorporate the information on the fresh snow accumulation from the CPD into the interferometric SWE retrieval algorithm. The aim is to detect and correct interferometric phase wraps. First results using airborne SAR data indicate that including the CPD improves the accuracy of the SWE retrieval.

3.1 Introduction

Snow water equivalent (SWE) refers to the amount of water in the snow pack and is required as an input parameter for hydrological models [1], for example, flood forecasting models [2]. With remote sensing, SWE measurements can be acquired on a global scale [3]. Passive microwave sensors are used to obtain large scale SWE products but suffer from low spatial resolution [4]. In contrast, active microwave sensors such as synthetic aperture radar (SAR) offer the possibility of monitoring the Earth at a meter scale [5].

Especially, repeat pass differential interferometric SAR (DInSAR) can be used to estimate the SWE change between two acquisitions as there is a clear physical relationship between the SWE change and the DInSAR phase. Microwaves are refracted in the snow pack because the snow has different dielectric properties than air. This causes a phase delay which can be measured using the interferometric phase [6], [7].

However, the 2π ambiguity of the interferometric phase introduces phase wraps, leading to wrong SWE change estimates. These phase wraps occur when the SWE change between two acquisitions is above (or below) a certain wavelength-dependent threshold.

Applying polarimetry, the copolar phase difference (CPD) between the vertical VV and horizontal HH copolarized channels can indicate the amount of freshly fallen snow [8],[9],[10]. A physical model has been presented in [11], that uses the CPD to invert the snow depth, by assuming the density and anisotropy of a snow pack.

Since the CPD measurements can be linked to the amount of fresh snow, this study aims to include the CPD measurements into the DInSAR retrieval in order to estimate phase wraps of the interferometric phase.

In this letter, we therefore propose to combine the DInSAR SWE estimation with the polarimetric information of the radar waves to improve the performance of the retrieval.

3.2 Methods

3.2.1 SWE Estimation Using DInSAR

The change in SWE ΔSWE_{Inf} between two temporally separated SAR measurements can be retrieved using the interferometric phase $\Delta\Phi_{Inf}$ between the acquisitions [6], [7]. The interferometric phase $\Delta\Phi_{Inf}$ can be obtained from the complex interferometric coherence γ_{Inf}, which describes the cross correlation between the signal at the first acquisition S_1 and at the second acquisition S_2 with

$$\Delta\Phi_{Inf} = \arg(\gamma_{Inf}) = \arg\left(\frac{\langle S_1 S_2^* \rangle}{\sqrt{\langle S_1 S_1^* \rangle \langle S_2 S_2^* \rangle}}\right). \quad (1)$$

Radar waves are refracted in a dry snow pack due to the difference in dielectric properties between snow and air. This causes a change in the optical path length of the radar wave, which depends on the amount of snow. The relation between the SWE change ΔSWE_{Inf} and interferometric phase $\Delta\Phi_{Inf}$ can be written as [7]

$$\Delta SWE_{Inf} = \frac{\Delta\Phi_{Inf}}{2k\frac{\alpha}{2}\left(1.59+\Theta^{\frac{5}{2}}\right)}. \quad (2)$$

In this case, $k = 2\pi/\lambda$ is the wavenumber that depends on the wavelength λ. α is a parameter around 1, which is used to reduce the root mean square error (RMSE) between the exact solution and the numerical approximation. For a fixed value of $\alpha = 1$, the maximum error for incidence angles smaller 40° lies below 3%, as has been shown in [7], therefore $\alpha = 1$ will be used. Θ is the incidence angle of the radar wave.

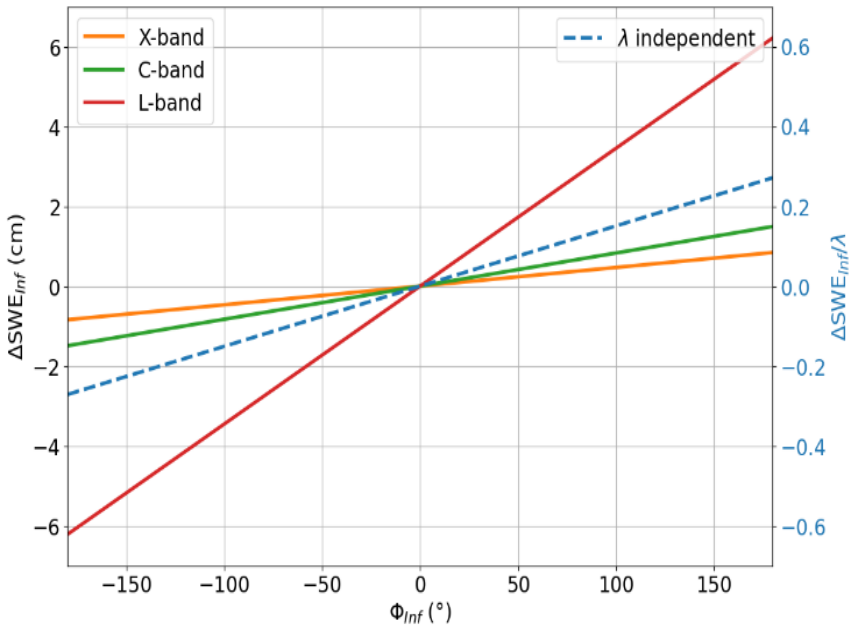

Fig. 1. SWE change ΔSWE_{Inf} in dependence of the interferometric phase for an incidence angle of 34°. The solid lines show the changes for X-, C- and L-band. The dashed line represents the SWE change divided by the wavelength.

One limitation of this method is that the interferometric phase can only be measured in the range [-180°, 180°]. As a result, only ΔSWE_{Inf} in a certain interval can be estimated. Fig. 1 shows $\Delta\text{SWE}_{\text{Inf}}$ in dependence of the interferometric phase assuming an exemplary incidence angle of 34° for X-, C- and L-band. Furthermore, the ratio between ΔSWE_{Inf} and λ is displayed to show the linear dependency independent of the wavelength. Longer wavelengths like L-band have the ability to measure higher ΔSWE_{Inf} while shorter wavelengths like X- and C-band have a higher sensitivity to smaller changes. SWE change values exceeding the interval, as shown by the SWE change values for +/-180° interferometric phase in Fig. 1, would result in phase wraps. These phase wraps have to be corrected for an accurate ΔSWE_{Inf} estimation.

3.2.2 Link Between CPD and Snow Parameters

The CPD Φ_{CPD} can be calculated from the complex polarimetric coherence γ_{CPD} between the vertical polarized signal S_{VV} and the horizontal polarized signal S_{HH}, and can be described by the difference between the phase Φ_{VV} and Φ_{HH}

$$\Phi_{CPD} = \arg(\gamma_{CPD}) = \arg\left(\frac{\langle S_{VV}S_{HH}^{*}\rangle}{\sqrt{\langle S_{VV}S_{HH}^{*}\rangle\langle S_{VV}S_{HH}^{*}\rangle}}\right) = \Phi_{VV} - \Phi_{HH}. \quad (3)$$

The delay of a signal in an anisotropic snowpack depends on its polarization. The anisotropy is caused by the horizontal alignment of freshly accumulated snow grains [11]. This results in a decrease of the propagation speed of horizontally polarized radar waves, increasing the Φ_{CPD}. After a few days or weeks, the snow structure becomes more vertically oriented due to the

temperature gradients that exist along the snow depth, which then can be associated with a slower propagation speed of the vertical polarized radar waves, decreasing the CPD [8].

The model proposed in [11] shows that the snow depth Z_s can be linked to the Φ_{CPD} as

$$\Phi_{CPD} = -\frac{4\pi}{\lambda} Z_s \left(\sqrt{n_V^2 - \sin^2(\Theta)} - \sqrt{n_H^2 - \sin^2(\Theta)}\right). \quad (4)$$

n_V and n_H are the refractive indices for the vertically and horizontally polarized radar waves and can be estimated by assuming a density ρ_s and anisotropy A of the snow pack [11]. For fresh snow, density values around $\rho_s = 0.2$ g/cm^3 can be measured with positive anisotropies [11].

3.2.3 Combination of DInSAR and CPD for SWE Estimation

The aim is to use (2) to estimate ΔSWE_{Inf}. In the next step, polarimetric information is included to check whether phase wraps occurred. For that, the CPD change $\Delta\Phi_{CPD}$ between the two images is calculated and linked to the snow depth change ΔZ_s according to (4), with

$$\Delta Z_s = -\frac{\Delta\Phi_{CPD}}{\frac{4\pi}{\lambda}\left(\sqrt{n_V^2 - \sin^2(\Theta)} - \sqrt{n_H^2 - \sin^2(\Theta)}\right)}. \quad (5)$$

Now, ΔZ_s can be linked to the ΔSWE_{CPD} by assuming the snow density using the approximation

$$\Delta SWE_{CPD} \approx \Delta Z_s * \rho_s/\rho_{water}. \quad (6)$$

The density of water is notated with ρ_{water}.

ΔSWE_{CPD} from (6) is now used to estimate the amount of phase cycles which need to be corrected in the ΔSWE_{Inf} estimate to obtain corrected SWE change values. The applied correction criterium is

$$|\Delta SWE_{Inf} - \Delta SWE_{CPD}| < \Delta SWE_{Inf}(\Phi = \pi). \quad (7)$$

With the criterium we check whether adding an interferometric phase cycle reduces the difference between ΔSWE_{Inf} and ΔSWE_{CPD} and if it applies then the missing phase cycle $[\Delta SWE_{Inf}(\Phi = 2\pi)]$ is added. This step is repeated until the correction criterium is not valid anymore. This approach is more robust than translating ΔSWE_{CPD} directly into interferometric phase cycles, because it ensures that no phase wrap is added if the actual ΔSWE_{Inf} is slightly below and ΔSWE_{CPD} is slightly above the phase wrap threshold, as adding the missing phase cycles would increase the difference between the two observables.

3.3 Data

In March 2021, the DLR's airborne radar system F-SAR performed fully polarimetric C-band (λ= 5.65 cm) and L-band (λ= 22.63 cm) measurements over a snow-covered area in the Austrian Alps. These acquisitions were part of the SARSimHT-NG study by ESA [12]. In the time frame of the F-SAR acquisitions, snow parameters like snow depth, density and SWE were measured by a ground team from ENVEO [13]. The first interferometric image pair is from measurements on the 02.03./06.03.2021 with a small snowfall event ($\Delta SWE_{Inf} \approx 10$ mm) below the phase wrap threshold. The second interferometric pair from 06.03./19.03.2021 contains a larger snow fall event ($\Delta SWE_{Inf} \approx 70$ mm), resulting in phase wraps. To calculate ΔSWE_{Inf}, the interferometric phase is calibrated with the closest corner reflector which was placed in the measured scene. Snow was removed from the corner reflectors during the measurements.

3.4 Results

3.4.1 Sensitivity of the Model

Fig. 1 shows that in the DInSAR model, the first phase wrap for Θ=34° occurs at $\Delta SWE_{Inf}/\lambda = 0.27$. This corresponds to a SWE change of $\Delta SWE_{Inf,Wrap,C} = 15.3$ mm at C-band and $\Delta SWE_{Inf,Wrap,L} = 61.1$ mm at L-Band, representing the need to correct phase wraps at small wavelengths.

When determining the ΔSWE_{CPD} from the polarimetric phase and comparing it to the phase wraps of ΔSWE_{Inf}, the results in Fig. 2 are obtained. The lines mark the SWE changes for three different densities at two different anisotropies in the figures. The red area above the first horizontal line represents the region where the SWE change would be high enough to observe one wrap of the DInSAR phase. The yellow marked area corresponds to SWE changes that result in two wraps in the DInSAR phase and so forth.

Phase wraps of the CPD phase are not expected even for large SWE changes. The sensitivity of the CPD phase to SWE changes (lines in Fig. 2) is significantly lower than when using the DInSAR phase (Fig. 1). Furthermore, ΔSWE_{CPD} depends on density and anisotropy assumptions. Therefore, the CPD model is only used to assess the number of interferometric phase wraps and the DInSAR model is used for the actual estimation of the SWE change.

The influence of phase noise affects the SWE change estimate and can be analyzed by means of the interferometric and polarimetric coherence. The estimation error for the phase can be calculated using the Cramer-Rao bounds [14]

$$\sigma_{\Phi} = \frac{1}{|\gamma|}\frac{\sqrt{1-|\gamma|^2}}{\sqrt{2N}}. \quad (8)$$

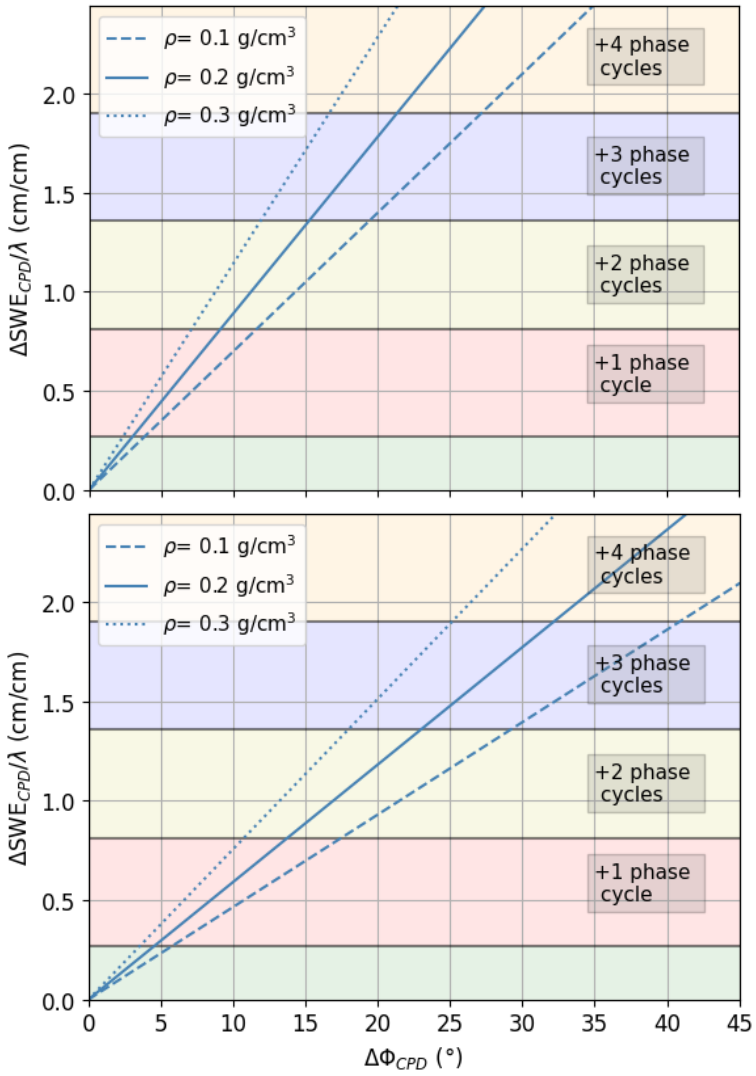

Fig. 2. Estimated SWE change $\Delta SWE_{CPD}/\lambda$ calculated from the CPD change for different snow densities for an incidence angle of 34°. The background colors indicate to which amount of missing phase cycles this would correspond in the DInSAR model for ΔSWE_{Inf}. The assumed anisotropies are: (top) A=0.2 (bottom) A=0.3.

$|\gamma|$ is the coherence amplitude and N are the number of looks. The error can be translated into a wavelength independent estimation error for the SWE change. For the DInSAR case, (2) is used and the results in dependence of the coherence are shown in Fig. 3. The estimation error decreases when a higher number of looks is used. For the data, a window size of 81 is used. The points correspond to F-SAR measurements at the in situ SWE locations. The L-band measurements have higher coherences, due to less temporal decorrelation, which leads to smaller ΔSWE_{Inf} errors relative to the wavelength.

The error due to the phase noise can be estimated also for the polarimetric case using the Cramer-Rao bounds. By propagating the phase error in (5), the following equation for the error is obtained:

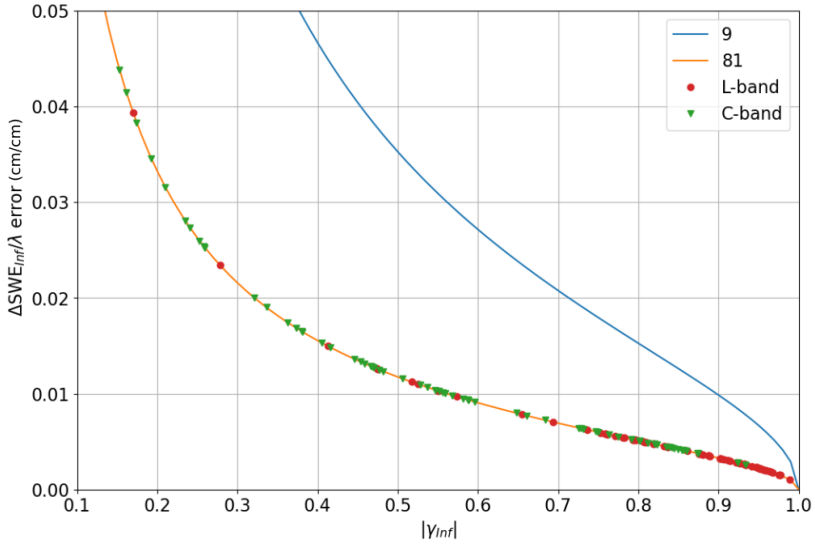

Fig. 3. Error for SWE change divided by wavelength due to phase noise in dependence of the interferometric coherence for 9 and 81 looks. The points are the C- and L-band measurements.

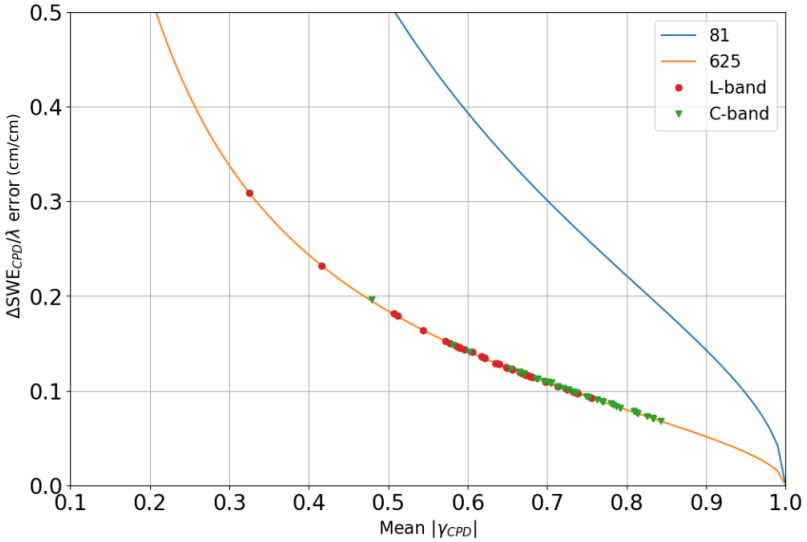

Fig. 4. Error for SWE change divided by wavelength due to phase noise in dependence of the polarimetric coherence for 81 and 625 looks for a snow density of $\rho_s = 0.1$ g/cm^3 and anisotropy of $A = 0.3$. The points are the C- and L-band measurements.

$$\sigma_{\Delta Z_s} = \sqrt{\left(\frac{\partial \Delta Z_s}{\partial \Phi_{\mathrm{CPD},1}}\right)^2 \sigma^2_{\Phi_{\mathrm{CPD},1}} + \left(\frac{\partial \Delta Z_s}{\partial \Phi_{\mathrm{CPD},2}}\right)^2 \sigma^2_{\Phi_{\mathrm{CPD},2}}}\,. \tag{9}$$

The error $\sigma_{\Delta Z_s}$ can be translated into a SWE change error using (6). As the relative SWE change errors are higher in the polarimetric case than in the DInSAR case, the number of looks has been increased as shown in Fig. 4. It is observed that C-band has higher mean polarimetric coherences than L-band, with associated smaller ΔSWE_{CPD} errors in C-band.

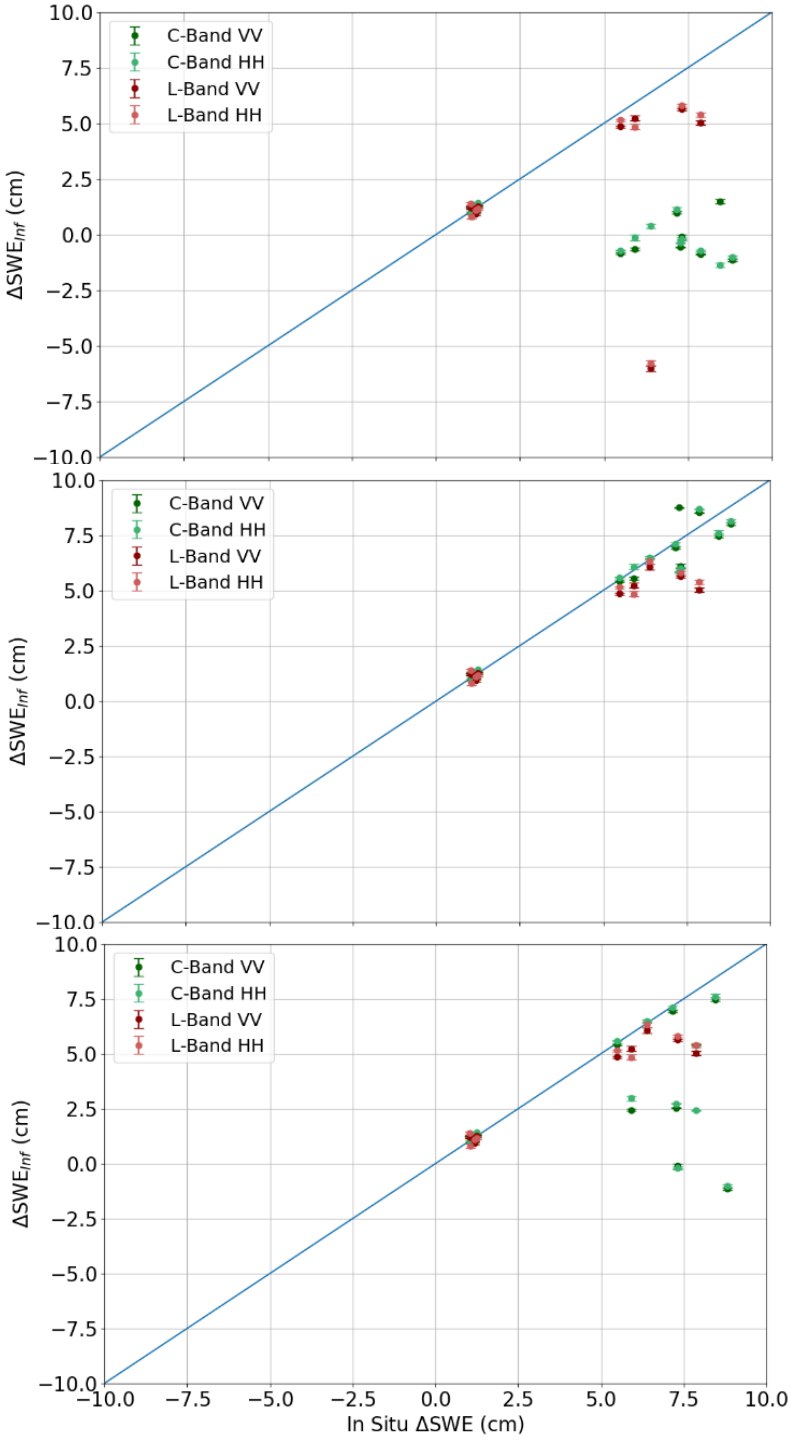

Fig. 5. Retrieved SWE values for C- and L-band in dependence of the in situ measurements. (Top) Before phase wrap correction. (Middle) After phase wrap correction based on the in situ measurements. (Bottom) After phase wrap correction based on the CPD model assuming a snow density of $\rho_s = 0.1 g/cm^3$ and anisotropy of A=0.2.

3.4.2 Examples Using F-SAR data

The F-SAR data can be utilized to calculate ΔSWE_{Inf} with (2). The comparison between the estimation results and the in situ measurements are presented in Fig. 5 (top) for both wavelengths and both polarizations. Here it has to be pointed out that interferometric coherences below 0.25

were masked out to keep the error below 10% of the phase wrap threshold, as well as incidence angles below 20° and slopes higher than 25%. Moreover, as the CPD change will be used for phase wrap corrections later, pixels with polarimetric coherences below 0.6 are also masked out, so that the ΔSWE_{CPD} error does not exceed half of the DInSAR phase wrap threshold. It can be seen that especially for higher in situ changes, the C-band estimations are clearly underestimated, indicating phase wraps due to the SWE change.

For validation of the phase wrap correction, in situ measurements are used to check if the actual SWE change was above the phase wrap threshold and to correct the SWE estimates accordingly. This results in Fig. 5 (middle). The C-band and L-band SWE estimates have been clearly improved with the in situ based phase wrap correction. This step shows the importance of accurate phase wraps estimations, especially for shorter wavelengths.

To test the proposed method, the CPD change between the images is calculated and used with (5) and (6) to estimate the occurrence of phase wraps. One example is shown in Fig. 5 (bottom) assuming a snow density of $\rho_s = 0.1$ g/cm^3 and anisotropy of A=0.2. It can be seen that some phase wraps are correctly predicted, while some are not identified or not sufficiently corrected.

For a better comparison between the frequencies, the relative RMSE ($RMSE_{rel}$) between the measurements and the retrieved SWE changes is calculated and set in relation to the wavelength with

$$RMSE_{rel} = RMSE/\lambda\,. \tag{10}$$

The results of which are displayed in Table I. In general, the L-band retrieval has a smaller $RMSE_{rel}$ compared to the C-band results. After performing the in situ correction, the C-band results show a higher improvement. This results from the fact that C-band estimations suffer more from phase wraps than the L-band estimations due to the shorter wavelength. Therefore, it is more likely that phase wraps in C-band have to be

TABLE I
$RMSE_{REL}$ OF THE SWE CHANGE ESTIMATES

	$RMSE_{rel}$			
Wavelength	C-band		L-band	
Polarization	VV	HH	VV	HH
No Correction	1.10	1.13	0.19	0.19
In Situ Correction	0.13	0.12	0.05	0.05
CPD Correction				
$A = 0.2, \rho_s = 0.1$ g/cm^3	0.72	0.72	0.05	0.05
$\rho_s = 0.2$ g/cm^3	0.74	0.72	0.05	0.05
$\rho_s = 0.3$ g/cm^3	0.72	0.71	0.14	0.15
$A = 0.3, \rho_s = 0.1$ g/cm^3	0.86	0.82	0.05	0.05
$\rho_s = 0.2$ g/cm^3	0.78	0.81	0.05	0.05
$\rho_s = 0.3$ g/cm^3	0.73	0.69	0.05	0.05

corrected. When performing the correction based on the CPD change, the results depend on the assumptions of snow density and anisotropy. For both wavelengths, the results improve compared to the uncorrected as some phase wraps can be reconstructed. However, the accuracy depends on the assumptions. As only the fresh snow change between the measurements is considered, assuming a small snow density and a rather high anisotropy seems appropriate. However, the preferred assumptions might depend on the snow conditions and the time span between the acquisitions.

The insufficient phase wrap detections in the CPD correction may result from the fact that snow metamorphism can occur between the acquisition dates. Due to the change in particle orientation, the measured CPD change does not solely represent the depth of fresh snow. This may improve for shorter temporal baselines.

However, the overall performance of the SWE retrieval improves compared to no correction and should be considered, when in situ data is unavailable.

3.5 Conclusions

The combination of DInSAR and PolSAR can help to identify and correct for phase wraps of the DInSAR SWE change estimates and can therefore improve the retrieval. However, the correction has still a lower accuracy than when in situ data is used for phase wrap correction. One reason could be snow metamorphism which occurs between the measurements. Over time, the snow becomes more vertically orientated, leading to a CPD change that is not solely related to fresh snow. Another difficulty with the CPD model is that it requires assumptions on the snow density and anisotropy, which have an impact on its accuracy. However, the CPD correction improves the estimation in comparison to no correction, particularly for shorter wavelengths such as C-band. Therefore, the CPD model can contribute to efforts deriving SWE change directly from remote sensing SAR data without the need to incorporate in situ data, towards accurate large-scale measurements of SWE changes.

3.6 Acknowledgement

The authors would like to thank the DLR F-SAR team for the acquisition of the airborne SAR data and the ground team from ENVEO for the collection of in situ measurements.

3.7 References

[1] M. P. Clark *et al.*, “Representing spatial variability of snow water equivalent in hydrologic and land-surface models: A review,” *Water Resour. Res.*, vol. 47, no. 7, Jul. 2011, doi: 10.1029/2011WR010745.

[2] T. Nester, R. Kirnbauer, J. Parajka, and G. Blöschl, “Evaluating the snow component of a flood forecasting model,” *Hydrol. Res.*, vol. 43, no. 6, pp. 762–779, May 2012, doi: 10.2166/nh.2012.041.

[3] J. Shi, C. Xiong, and L. Jiang, “Review of snow water equivalent microwave remote sensing,” *Sci. China Earth Sci.*, vol. 59, no. 4, Art. no. 4, Apr. 2016, doi: 10.1007/s11430-015-5225-0.

[4] N. Saberi, R. Kelly, M. Flemming, and Q. Li, “Review of snow water equivalent retrieval methods using spaceborne passive microwave radiometry,” *Int. J. Remote Sens.*, vol. 41, no. 3, pp. 996–1018, Feb. 2020, doi: 10.1080/01431161.2019.1654144.

[5] A. Moreira, P. Prats-Iraola, M. Younis, G. Krieger, I. Hajnsek, and K. P. Papathanassiou, “A tutorial on synthetic aperture radar,” *IEEE Geosci. Remote Sens. Mag.*, vol. 1, no. 1, Art. no. 1, Mar. 2013, doi: 10.1109/MGRS.2013.2248301.

[6] T. Guneriussen, K. A. Hogda, H. Johnsen, and I. Lauknes, “InSAR for estimation of changes in snow water equivalent of dry snow,” *IEEE Trans. Geosci. Remote Sens.*, vol. 39, no. 10, pp. 2101–2108, Oct. 2001, doi: 10.1109/36.957273.

[7] S. Leinss, A. Wiesmann, J. Lemmetyinen, and I. Hajnsek, “Snow Water Equivalent of Dry Snow Measured by Differential Interferometry,” *IEEE J. Sel. Top. Appl. Earth Obs. Remote Sens.*, vol. 8, no. 8, pp. 3773–3790, Aug. 2015, doi: 10.1109/JSTARS.2015.2432031.

[8] S. Leinss, G. Parrella, and I. Hajnsek, “Snow Height Determination by Polarimetric Phase Differences in X-Band SAR Data,” *IEEE J. Sel. Top. Appl. Earth Obs. Remote Sens.*, vol. 7, no. 9, pp. 3794–3810, Sep. 2014, doi: 10.1109/JSTARS.2014.2323199.

[9] A. Patil, G. Singh, and C. Rüdiger, “Retrieval of Snow Depth and Snow Water Equivalent Using Dual Polarization SAR Data,” *Remote Sens.*, vol. 12, no. 7, Art. no. 7, Apr. 2020, doi: 10.3390/rs12071183.

[10] J. Voglimacci-Stephanopoli *et al.*, “Potential of X-band polarimetric synthetic aperture radar co-polar phase difference for arctic snow depth estimation,” *The Cryosphere*, vol. 16, pp. 2163–2181, 2022, doi: 10.5194/tc-16-2163-2022.

[11] S. Leinss, H. Löwe, M. Proksch, J. Lemmetyinen, A. Wiesmann, and I. Hajnsek, “Anisotropy of seasonal snow measured by polarimetric phase differences in radar time series,” *The Cryosphere*, vol. 10, no. 4, pp. 1771–1797, Aug. 2016, doi: 10.5194/tc-10-1771-2016.

[12] V. Grachea, R. Horn, T. Nagler, and J. Fischer, “SARSimHT-NG – Simulation of Hydroterra SAR System Performance in the Mediterranean and the Alps Based on Experimental Airborne SAR Data,” DLR, Enveo, ESA Airborne Campaign 2021-2022.

[13] T. Nagler *et al.*, “Field Campaigns on InSAR retrieval of snow mass in preparation of Copernicus ROSE-L,” presented at the Submitted to Living Planet Symposium, 2022.

[14] S. M. Kay, *Fundamentals of statistical signal processing: estimation theory*. Prentice-Hall, Inc., 1993.

4 Exploring DPolInSAR Coherence Regions for Snow Water Equivalent Estimation

K. Belinska, G. Fischer, K. Papathanassiou and I. Hajnsek

IEEE Transactions on Geoscience and Remote Sensing

Submitted October 2024.

This chapter is a pre-print of the submitted paper.

The author's contributions:

- Interferometric processing of the SAR data.
- Conceptualization and implementation of the DPolInSAR model and retrieval.
- Analysis and interpretation of the results.
- Writing of the manuscript.

The co-authors' contributions:

- G. Fischer and I. Hajnsek supervised the research.
- K. Papathanassiou provided the initial idea of DPolInSAR.
- G. Fischer, K. Papathanassiou and I. Hajnsek contributed to the main ideas, the discussion of the results, and reviewed the manuscript.

EXPLORING DPOLINSAR COHERENCE REGIONS FOR SNOW WATER EQUIVALENT ESTIMATION

Kristina Belinska[1,2], Georg Fischer[1], Konstantinos Papathanassiou[1], and Irena Hajnsek[1,2]
[1] German Aerospace Center, Microwaves and Radar Institute, Wessling, Germany
[2] ETH Zurich, Institute of Environmental Engineering, Zurich, Switzerland

Abstract

Snow Water Equivalent (SWE) is an important parameter in hydrology. The interferometric phase measured with Differential Interferometric Synthetic Aperture Radar (DInSAR) can be used to estimate the SWE change between two SAR acquisitions. However, only a limited interval of SWE changes can be retrieved unambiguously due to phase wraps depending on the wavelength. Furthermore, the polarization of the radar wave affects the SWE change estimates. In this study, interferometric and polarimetric observables are combined. A Differential Polarimetric Interferometric SAR (DPolInSAR) approach is proposed to model PolInSAR coherences that can potentially contribute to overcome limitations in SWE change estimations. The effect of snow changes on the PolInSAR coherence regions are investigated, revealing differences for changes in snow depth and anisotropy. Based on the DPolInSAR model, a SWE change retrieval is proposed, that tries to find the parameters for snow depth, density and anisotropy which minimize the difference between modelled and measured coherence regions. The RMSE between the DPolInSAR estimates and ground measurements improves compared to using only one polarization.

4.1 Introduction

Snow melt plays a crucial role for runoff predictions and flood protection. Due to increasing temperatures, the amount of melt water and timing of the runoff are changing. This has a huge impact on regions where people are relying on snow melt for their water supply [1].

A key observable combining the information on depth and density of the snow pack is the Snow Water Equivalent (SWE) and is therefore important as an input parameter for hydrological models [2].

Different remote sensing methods can be used to measure SWE [3], [4], but operational methods suffer from coarse resolution and saturation effects. Widely used are active radar sensors like Synthetic Aperture Radars (SARs), because they offer the possibility to monitor the Earth's

surface on a meter-scale [5]. Moreover, SAR sensors are capable of performing measurements that are not affected by weather and illumination conditions [6]. Given that SAR signals are able to penetrate into snow, they are sensitive to snow parameters [7].

It has been shown in [8] that repeat-pass interferometric SAR measurements (DInSAR) can be used to estimate SWE changes in dry snow. This method relies on the fact that snow has a different permittivity than air, which causes a refraction of the radar waves. The corresponding path delay depends on the SWE change between the acquisitions and can be measured with the interferometric phase. The method has been first demonstrated using ERS-1/2 tandem data [8].

Dedicated tower experiments were used to exploit the relationship between the DInSAR phase and SWE change in [9], where the authors presented a modification to the density related part of the model in [8]. They established a linear relation between interferometric phase and SWE change, obtaining results with a high accuracy. Here, a dense time series was used to overcome the effect of temporal decorrelation, which affects the accuracy of the SWE change estimates. Reasons for decorrelation of interferometric coherence in different frequencies were analyzed in [10], showing that snow melt is one of the main factors of decorrelation and that higher frequencies are more affected, decreasing the performance of the SWE retrieval. Meanwhile, for low frequencies the SWE accumulation profile showed good agreements with in situ measurements.

Compared to tower-based measurements, airborne SAR measurements can achieve a higher spatial coverage. Campaigns evaluating the potential of the interferometric phase for SWE retrieval where conducted, e.g. with the Uninhabited Aerial Vehicle SAR (UAVSAR) over North America [11], [12], [13], [14], [15], presenting good results over non forested areas and mentioning the need of reference phase and an approximation of the density as a limitation. Another airborne campaign was conducted over the Alps using the DLRs airborne system F-SAR [16]. Data from the latter will be also used in this study.

Several studies have used the interferometric phase of repeat-pass space borne SAR measurements to estimate the SWE change, showing a good agreement with ground-based measurements. Sensors with different frequencies were used, for example C band (wavelength $\lambda = 5.65\ cm$) [17], [18], [19], [20], [21], [22] and L band ($\lambda = 22.62\ cm$) [23], [24]. It was demonstrated using Sentinel-1 C band data that it is important to correct for the atmospheric phase delay [21]. Additionally, it was shown that low temporal coherence is one of the main reasons for a lower accuracy of the SWE change retrieval [17], [18], [19], [21] as well as the presence of wet snow [19], [20]. Furthermore, the vegetation inside the estimation window affects the SWE estimation results [22]. A wider coverage for validation was achieved by comparing the results from L band data from ALOS-2 to SWE change estimates from a snow model, showing a high agreement except for forested areas with temperatures close to zero degrees [24]. Furthermore, decorrelation due to permittivity changes of snow has been reported [25]. Another limitation of the retrieval is the 2π interval of the interferometric phase, resulting in a limited range of unambiguous SWE change values that can be retrieved before interferometric phase wraps occur [9]. One possibility of solving the phase wraps without additional ground measurements was

proposed in [26] by using a multifrequency approach to use the SWE change estimates of lower frequencies to correct for phase wraps of higher frequencies. This improves the accuracy retrieval, but the method is also limited due to phase calibration challenges and the availability of multifrequency measurements.

In addition to DInSAR, there are also methods that use polarimetric SAR (PolSAR) for the estimation of snow properties. In [27], [28] the backscatter of the cross polarized channels in VV and VH was used to retrieve the snow depth having the highest agreement at 500m and 1km resolution. It has been also demonstrated that the Copolar Phase Difference (CPD) between the VV and HH channel can be related to snow depth [29], [30], [31]. A model has been developed, where the CPD depends on the snow anisotropy, density and depth [29], [32]. The model has been successfully applied in studies using X band ($\lambda = 3.1\ cm$) data for example in [33] relying on density assumptions and in [34], having SWE errors up to 45%. In C and L band, the CPD model was applied to correct interferometric phase wraps in the DInSAR SWE retrieval [35], relying as well on density and anisotropy assumptions. Furthermore, it has been shown that for shorter wavelengths, inversions using the CPD are challenging due to phase wraps [36]. Nevertheless, these studies have demonstrated the potential for retrieving information on the snow pack from polarimetric measurements.

The objective of this study is to improve the accuracy of SWE change retrieval by not only using interferometric SAR measurements, but by also incorporating polarimetric information. To achieve this, they are combined by forming differential polarimetric interferometric SAR (DPolInSAR) coherences. A model is established to simulate DPolInSAR coherence regions and the effects of different snow changes on the coherence region parameters are investigated. The goal is to advance the theoretical understanding of temporal coherence regions influenced by snow accumulation and snow anisotropy. Based on this, a retrieval of snow changes from coherence regions is demonstrated by finding the parameters for snow depth, density and anisotropy which minimize the difference between modelled and measured coherence regions.

In Section 4.2, the data utilized in this study are described. Section 4.3 presents the model of [9] for SWE change retrieval and introduces the polarization dependence of the estimates. A PolInSAR SWE change framework is established in Section 4.4 followed by the DPolInSAR SWE change retrieval in Section 4.5. The results are discussed in Section 4.6 and concluded in Section 4.7.

4.2 Data

In the frame of ESA's SARSimHT-NG study [37] DLR conducted an airborne SAR campaign over an alpine site located in the Woergetal valley in the Austrian Alps. A time series of eight flights from the 2nd to the 19th of March 2021 was acquired including fully polarimetric SAR data at C band and L band. A polarimetric Pauli RGB color composite at C band is shown in Fig. 1.

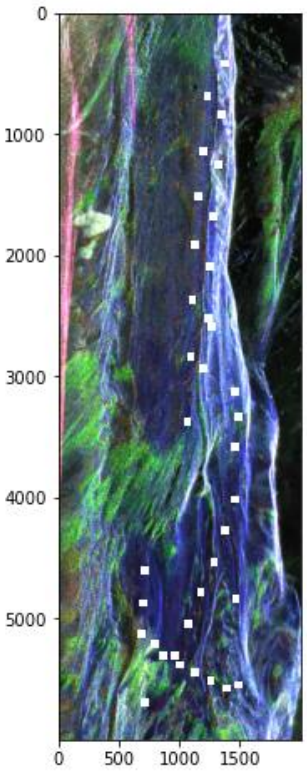

Fig. 1. Polarimetric Pauli RGB color composite at C band of the test site in the Woergetal. The white points mark the locations of the ground measurement.

TABLE I
FSAR ACQUISITIONS

Interferogram	Dates (Primary/Secondary)	Frequency	SWE change (cm)
Inf1	03.03.2021/ 06.03.2021	C, L band	≈ 1.15
Inf2	06.03.2021/ 19.03.2021	C, L band	≈ 6.75

There were two snowfall events during the campaign that are investigated in this study. The first (referred to in this paper as Inf1) occurred at the beginning of the campaign on the 5th of March followed by a more significant snowfall event (Inf2) which occurred between the 14th and the 18th of March. The interferograms used in this study are shown in Table I. The campaign was accompanied by ground measurements of snow depth and density at different locations in the valley performed by ENVEO [16].

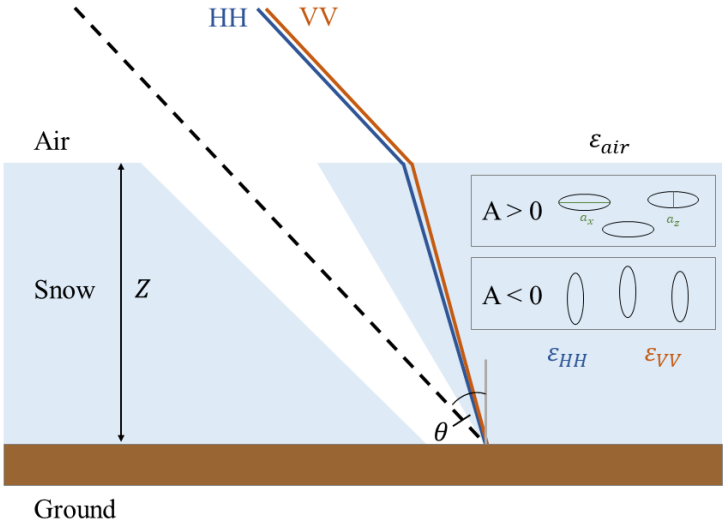

Fig. 2. Refraction of radar waves inside a snow pack compared to the optical path length of snow free conditions (dashed line). The refractions are different for HH and VV due to the anisotropy of the snow pack.

4.3 Single-Pol DInSAR *ΔSWE* Estimation

4.3.1 Relationship between DInSAR phase and *ΔSWE*

SWE expresses the amount of liquid water in the snow pack and can be described as the theoretical depth of water that would be obtained if the snowpack were to melt completely. Accordingly, SWE depends on the snow density ρ and snow depth Z using:

$$SWE = \frac{1}{\rho_w} \int_0^Z \rho(Z)\, dZ \approx Z\rho/\rho_w \tag{1}$$

where ρ_w is the density of water.

The change of SWE ΔSWE, caused by a change of snow density and/or depth, is attempted to be measured by exploring differential interferometric phase measurements, as first proposed in [8]. As snow has different dielectric properties than air, radar waves when propagating through snow pack are refracted and change their propagation velocity, as shown in Fig. 2.

Accordingly, any SWE change can be associated with an optical path length difference that can be measured by means of a differential phase. It is assumed that in dry snow the main scattering contribution comes from the underlying ground and volume scattering can be neglected for frequencies below 20GHz [38]. So, it is assumed that the radar waves can travel through the entire snow volume. By taking into account the geometry in Fig. 2, the interferometric phase difference $\Delta\Phi$ can be related to the snow depth change with [8]:

$$\Delta\Phi = -2\,k\Delta Z\left(\cos\Theta - \sqrt{\varepsilon(\rho) - \sin\Theta^2}\right), \quad (2)$$

where $k = 2\pi/\lambda$ is the wavenumber depending on the wavelength λ, Θ the incidence angle of the radar wave and $\varepsilon(\rho)$ the permittivity of the snow, which depends on the snow density ρ. Based on a numerical approximation for the density related part of the equation it has been attempted to model a linear relation between the interferometric phase difference and the ΔSWE, which can be calculated with [9]:

$$\Delta\Phi = 2\,k\frac{\alpha}{2}\left(1.59 + \Theta^{\frac{5}{2}}\right)\Delta SWE. \quad (3)$$

The parameter α is close to 1 and minimizes the Root Mean Square Error (RMSE) between the numerical approximation and the exact solution for different ρ and Θ values. When the parameter α is fixed to $\alpha = 1$ then the error lies below 3% for incidence angles smaller than 40°. In our study $\alpha = 1$ is used in the following.

An important issue when estimating the SWE change using the DInSAR phase are phase wraps. They result from the fact that the interferometric phase can only be measured in a range between [-π, π] until a phase wrap occurs, therefore only a limited range of SWE change values can be retrieved unambiguously.

The advantage of (3) is that the ΔSWE can be directly estimated from the interferometric phase. In (2) a relation between the permittivity and density of the snow is needed, as shown in [39], for example. However, this offers the possibility to incorporate different permittivities for different polarizations, in order to have a more precise description of the polarimetric observations.

4.3.2 Polarization dependence of ΔSWE estimation

In order to assess the effect of the radar polarization on ΔSWE estimation, ΔSWE is estimated by means of (3) using vertically polarized (VV) and horizontally polarized (HH) channels separately. Fig. 3 shows the difference between the two ΔSWE estimates ΔSWE_{VV} and ΔSWE_{HH} at C band for the first and second interferogram. Areas with local slopes higher than 50% are masked out.

In both images, considerable differences can be observed. Both the difference between ΔSWE_{VV} and ΔSWE_{HH} and its standard deviation increase in the second interferogram, associated to the bigger snowfall event (Table II). A 0.14 cm SWE difference between HH and VV is about 12% of the total SWE change for the snowfall event in Inf1.

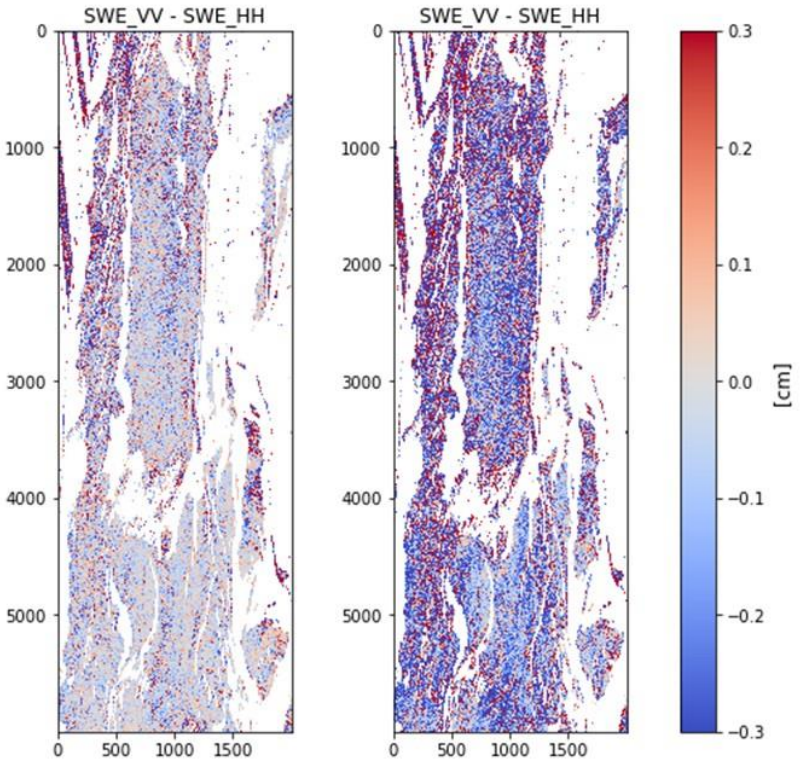

Fig. 3. Difference between the SWE change estimates in C band using the DInSAR VV and DInSAR HH phase. The left side is corresponding to Inf1 and the right side to Inf2. White areas are masked out due to local slopes higher than 50%.

TABLE II
DIFFERENCE BETWEEN SWE CHANGE ESTIMATES IN VV AND HH

C-band	Inf 1	Inf 2
Abs $\Delta SWE_{VV} - \Delta SWE_{HH}$ Difference (cm)	0.140 +/- 0.197	0.328 +/- 0. 33

The discrepancy between the SWE change estimates in VV and HH indicates a dependency of the SWE change estimates on the used polarization. This highlights the importance of including polarimetric information in the SWE change retrieval, as it is necessary to account for polarization effects. Furthermore, it allows to gain additional information that can be incorporated in the SWE change algorithm. The reason for the discrepancy between the ΔSWE_{VV} and ΔSWE_{HH} estimates lies in the anisotropic nature of the snow that is discussed in the following.

4.3.3 The Structural Anisotropy of Snow

Snow packs appear anisotropic in the context of microwave propagation [32]. This is when non-spherical ice particles distribute with a preferential orientation. This anisotropic shape of spheroidal ice particles is described by the (structural) anisotropy A defined as the normalized difference of the x and z dimension of the ice particles a_x and a_z

$$\mathrm{A} = \frac{a_x - a_z}{0.5 * (a_x + a_z)}. \tag{4}$$

When snow settles, it forms rather horizontally aligned ice particles and the anisotropy becomes positive (see Fig. 2). Over the time, temperature gradients between atmosphere and the underlying soil force the ice particles to grow increasingly vertically imposing a negative anisotropy (see Fig. 2).

The preferential orientation of non-spherical ice particles leads to an anisotropic (i.e. directionally different) permittivity in the snow pack, which makes the vertically and horizontally polarized radar waves propagate differently.

To calculate the directional permittivities, the model described in [32] is used. In that, the snow is described as ice particles inside air. The effective permittivity for each dimension $n = x, y, z$ for the ice-air mixture is calculated using the Maxwell Garnett formula [40]:

$$\varepsilon_{eff,n} = \varepsilon_{air} + f\varepsilon_{air} \frac{\varepsilon_{ice} - \varepsilon_{air}}{\varepsilon_{air} + (1 - f)N_n(\varepsilon_{ice} - \varepsilon_{air})}. \tag{5}$$

ε_{air} is the permittivity for air and ε_{ice} for the ice particles. The ice volume fraction f is defined by the snow density. For each dimension of the particle, the depolarization factors N_n are calculated with:

$$N_n = \frac{a_x a_y a_z}{2} \int_0^\infty \frac{ds}{(s + a_n^2)\sqrt{(s + a_x^2)(s + a_y^2)(s + a_z^2)}}. \tag{6}$$

For oblate spheroids, as in the case of fresh snow, the condition $a_x = a_y > a_z$ holds. The solution of the integral in (6) is then given by [40]:

$$N_x = N_y = \frac{1}{2}(1 - N_z), \tag{7}$$

$$N_z = \frac{1 + e^2}{e^3}(e - arctan\, e), \tag{8}$$

where e is a parameter that depends on the anisotropy:

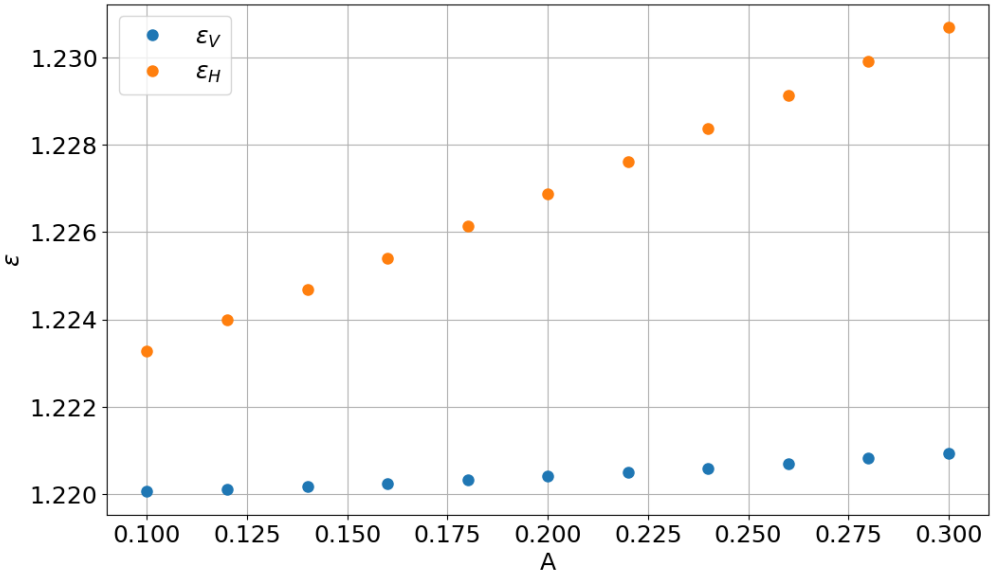

Fig. 4. Permittivity of the VV channel (blue) and the HH channel (orange) in dependence of the anisotropy. ($\rho = 0.15\ g/cm^3$, Θ = 39°)

$$e = \sqrt{\left(\frac{2+A}{2-A}\right)^2 - 1}. \tag{9}$$

The depolarization factors from (7) and (8) are then used to calculate the effective permittivity for a mixture of air and ice using (5). In the last step, the effective permittivities in x,y,z dimension have to be translated to the horizontal and vertical polarization of the radar waves.

$$\varepsilon_H = \varepsilon_{eff,x;y}, \tag{10}$$

$$\varepsilon_V = \varepsilon_{eff,x;y} + \left(1 - \frac{\varepsilon_{eff,x;y}}{\varepsilon_{eff,z}}\right) \varepsilon_{air}\, sin^2\, \Theta. \tag{11}$$

Therefore, the effective permittivity ε_H for the horizontal and ε_V for the vertical polarization depend on the anisotropy and density of the snow pack, as well as on the local incidence angle [29], [32].

The obtained permittivities ε_H and ε_V are plotted for different anisotropies setting a fixed density and incidence angle in Fig. 4. A difference between the permittivities ε_V and ε_H can be observed, which is increasing for higher anisotropies because the difference of the refraction for the vertical and horizontal polarization increases. These permittivities can be used in (2) to calculate the polarization dependent interferometric phase for VV and HH. The difference between the phases in VV and HH will increase with the snow depth, since the length of the path through the anisotropic medium expands.

4.4 A PolInSAR *ΔSWE* Framework

4.4.1 PolInSAR framework

The starting point for establishing a PolInSAR framework for ΔSWE estimation are two scattering matrices $[S_1]$ and $[S_2]$ measured by an interferometric configuration. These two matrices can be vectorized in order to obtain the two associated scattering vectors $\vec{k}_{L1}$ and $\vec{k}_{L2}$:

$$\vec{k}_{Li} = vec([S_i]) = [s^i_{HH}, s^i_{VH}, s^i_{HV}, s^i_{VV}]^T, \tag{12}$$

where $i \in [1,2]$ indicates the two interferometric measurements. The interferogram formed using a polarization state expressed by the unitary vector $\vec{w}$ is:

$$s(\vec{w})_1 s(\vec{w})^*_2 = (\vec{w}^+ \cdot \vec{k}_{L1})\,(\vec{w}^+ \cdot \vec{k}_{L2})^* = \vec{w}^+ [\Omega_L] \vec{w}, \tag{13}$$

and the associated (complex) interferometric coherence follows as

$$\gamma(\vec{w}) = \frac{\vec{w}^+ \langle [\Omega_L] \rangle \vec{w}}{\sqrt{(\vec{w}^+ \langle [C_1] \rangle \vec{w})(\vec{w}^+ \langle [C_2] \rangle \vec{w})}}, \tag{14}$$

where $\vec{k}_{L1} \cdot \vec{k}^+_{L1} = [C_1]$, $\vec{k}_{L2} \cdot \vec{k}^+_{L2} = [C_2]$ and $\vec{\mathrm{k}}_{\mathrm{L1}} \cdot \vec{\mathrm{k}}^+_{\mathrm{L2}} = [\Omega_L]$. The two measured scattering matrices $[S_1]$ and $[S_2]$ include the polarimetric propagation and scattering effects as

$$[S_i] = [P^i_2][S_{0i}][P^i_2]^T \tag{15}$$

and

$$\vec{k}_{Li} = [P^i_4]\vec{k}_{0Li} = [P^i_4]\,\mathrm{vec}([S_{0i}]). \tag{16}$$

$[\mathrm{S_{0i}}]$ is the scattering matrix and $\vec{k}_{0Li}$ the scattering vector of the underlying scattering mechanism. The unitary propagation matrix $[P^i_2]$ characterizes completely the propagation medium in terms of two orthogonal eigen-polarizations with

$$\left[P_2^i\right] = \begin{bmatrix} cos\,\alpha_i & sin\,\alpha_i\, e^{j\delta_i} \\ -\,sin\,\alpha_i\, e^{j\delta_i} & cos\,\alpha_i \end{bmatrix} \begin{bmatrix} e^{j\kappa_{Ai}r_i} & 0 \\ 0 & e^{j\kappa_{Bi}r_i} \end{bmatrix} \tag{17}$$

The two eigen-polarizations are those polarizations that do not change when propagating through the medium. They are described by the Deschamps angles α_i and δ_i while their propagation through the medium is described by the (complex) wavenumbers κ_{Ai}, κ_{Bi} that include both attenuation and phase shifts (e.g. wavelength change). r_i is the distance traveled in the medium.

Since the preferred orientation of the non-spherical ice particles is often in the vertical or horizontal direction, the eigen-polarizations can be assumed to be given by the linear H and V polarizations. Accordingly, $\alpha_i = 0$ and $\delta_i = 0$ and $\left[P_2^i\right]$ reduces to:

$$\left[P_2^i\right] = \begin{bmatrix} e^{j\kappa_{Hi}r_i} & 0 \\ 0 & e^{j\kappa_{Vi}r_i} \end{bmatrix}. \tag{18}$$

κ_{Hi} is the wavenumber of the horizontal polarization and κ_{Vi} the one of the vertical. $\left[P_4^i\right]$ is obtained with:

$$[P_4^i] = [P_2^i] \otimes [P_2^i]^T = exp(j2\kappa_i r_i) \begin{bmatrix} exp(j\Delta\kappa_i r_i) & 0 & 0 & 0 \\ 0 & 1 & 0 & 0 \\ 0 & 0 & 1 & 0 \\ 0 & 0 & 0 & exp(-j\Delta\kappa_i r_i) \end{bmatrix} \tag{19}$$

where $\otimes$ denotes the Kronecker product, κ_i the mean and $\Delta\kappa_i$ the differential wavenumber of the two eigen-polarizations:

$$\Delta\kappa_i = \kappa_{Hi} - \kappa_{Vi}, \qquad \kappa_i = \frac{\kappa_{Hi} + \kappa_{Vi}}{2}. \tag{20}$$

The interferogram formed using the polarization state $\vec{w}$ is

$$s(\vec{w})_1 s(\vec{w})_2^* = (\vec{w}^+[P_4^1]\vec{k}_{0L1})\,(\vec{w}^+[P_4^2]\vec{k}_{0L2})^* = \vec{w}^+[P_4^1][\Omega_{0L}][P_4^2]^+ \tag{21}$$

and the associated interferometric coherence becomes:

$$\gamma(\vec{w}) = \frac{\vec{w}^+\langle[P_4^1][\Omega_{0L}]\,[P_4^2]^+\rangle\vec{w}}{\sqrt{(\vec{w}^+\langle[P_4^1][C_{01}][P_4^1]^+\rangle\vec{w})(\vec{w}^+\langle[P_4^2][C_{02}][P_4^2]^+\rangle\vec{w})}}.. \tag{22}$$

Assuming a homogeneous snow pack within the coherence estimation window, the following expression is obtained:

$$\gamma(\vec{w}) = \frac{\vec{w}^{+}[P_4^1]\langle[\Omega_{0L}]\rangle\,[P_4^2]^{+}\vec{w}}{\sqrt{(\vec{w}^{+}\,[P_4^1]\langle[C_0]\rangle[P_4^1]^{+}\vec{w}\,)(\,\vec{w}^{+}[P_4^2]\langle[C_0]\rangle[P_4^2]^{+}\,\vec{w}\,)}}. \tag{23}$$

4.4.2 The DPolInSAR Case

While the PolInSAR framework discussed in the previous section is general in terms of being valid for non-zero and zero spatial/temporal baselines, a closer look in the case of differential, e.g. repeat-pass with zero spatial baseline interferometry, is attempted in order to address the ΔSWE estimation. As the focus is put on interpreting the polarimetric and interferometric phase differences induced by the snow pack, the underlying scattering process is assumed to be not changing for the moment so that

$$[S_{01}] = [S_{02}] = [S_0] \rightarrow \vec{k}_{0L1} = \vec{k}_{0L2} = \vec{k}_{0L}, \quad \vec{k}_{0L} \cdot \vec{k}_{0L}^{+} = [C_0], \quad [\Omega_{0L}] = [C_0] \tag{24}$$

The interferogram formed using $\vec{w}$ polarization becomes

$$s_1 s_2^{*} = \vec{w}^{+}[P_4^1][C_0][P_4^2]^{+}\vec{w} = \vec{w}^{+}[A_{12}]\,\vec{w} \tag{25}$$

where

$$[A_{12}] = \exp(2j(\kappa_1 r_1 - \kappa_2 r_2)\begin{bmatrix} a_{11} & a_{12} & a_{13} & a_{14} \\ a_{21} & a_{22} & a_{23} & a_{24} \\ a_{31} & a_{32} & a_{33} & a_{34} \\ a_{41} & a_{42} & a_{43} & a_{44} \end{bmatrix}, \tag{26}$$

with

$$a_{11} = c_{11}\exp(j\Delta\kappa_1 r_1)\exp(-j\Delta\kappa_2 r_2), \quad a_{22} = c_{22},$$
$$a_{44} = c_{44}\exp(-j\Delta\kappa_1 r_1)\exp(j\Delta\kappa_2 r_2), \quad a_{33} = c_{33},$$
$$a_{14} = a_{41}^{*} = \mathrm{c}_{14}\exp(j\Delta\kappa_1 r_1)\exp(j\Delta\kappa_2 r_2), \quad a_{23} = a_{32}^{*} = c_{23},$$
$$a_{12} = a_{21}^{*} = \mathrm{c}_{12}\exp(j\Delta\kappa_1 r_1), \quad a_{13} = a_{31}^{*} = c_{13}\exp(j\Delta\kappa_1 r_1),$$
$$a_{24} = a_{42}^{*} = \mathrm{c}_{24}\exp(j\Delta\kappa_2 r_2), \quad a_{34} = a_{43}^{*} = c_{34}\exp(j\Delta\kappa_2 r_2),$$

where c_{ij} are the elements of the underlying covariance matrix $[C_0]$.

Since the snow depth change is one focus of this study, the wavenumber is replaced with a wavenumber that projects the change in range direction to the actual snow depth change with:

$$\kappa_i r_i = \tilde{\kappa}_i Z_i = \frac{\tilde{\kappa}_{Hi} + \tilde{\kappa}_{Vi}}{2} Z_i, \tag{27}$$

with

$$\tilde{\kappa}_{H\,or\,V} = \frac{2\pi}{\lambda}\left(cos\,\Theta\ - \sqrt{\varepsilon_{H\,or\,V} - sin^2\,\Theta}\ \right). \tag{28}$$

Accordingly, the interferogram in the HH polarization is obtained for $\vec{w}_{HH} = [\,1, 0, 0, 0]^T$

$$s_1(\vec{w}_{HH})s_2^*(\vec{w}_{HH}) = |s_{HH}|^2\, exp\left(j2(\tilde{\kappa}_{H1}Z_1 - \tilde{\kappa}_{H2}Z_2)\right), \tag{29}$$

while the interferogram for the VV polarization is obtained for $\vec{\mathrm{w}}_{\mathrm{VV}} = [\,0, 0, 0, 1]^{\mathrm{T}}$

$$s_1(\vec{w}_{VV})s_2^*(\vec{w}_{VV}) = |s_{VV}|^2\, \exp\left(j2(\tilde{\kappa}_{V1}Z_1 - \tilde{\kappa}_{V2}Z_2)\right). \tag{30}$$

The (complex) interferometric coherence can be calculated for all polarization states with:

$$\gamma(\vec{w}) = \frac{\vec{\mathrm{w}}^{+}[\mathrm{P}_4^1]\langle[\mathrm{C}_0]\rangle\,[\mathrm{P}_4^2]^{+}\vec{\mathrm{w}}}{\sqrt{(\vec{w}^{+}\,[P_4^1]\langle[C_0]\rangle[P_4^1]^{+}\vec{w}\,)(\,\vec{w}^{+}[P_4^2]\langle[C_0]\rangle[P_4^2]^{+}\,\vec{w}\,)}}. \tag{31}$$

The absolute value of the coherence is $|\gamma(\vec{w})| = 1$, which results as a direct consequence of the assumption of an invariant underlying scattering process and a homogeneous snow pack within the coherence estimation window. The set of interferometric coherences $\gamma(\vec{w})$ obtained for all the possible polarization states $\vec{w}$ plotted on the complex plane defines the so-called coherence region.

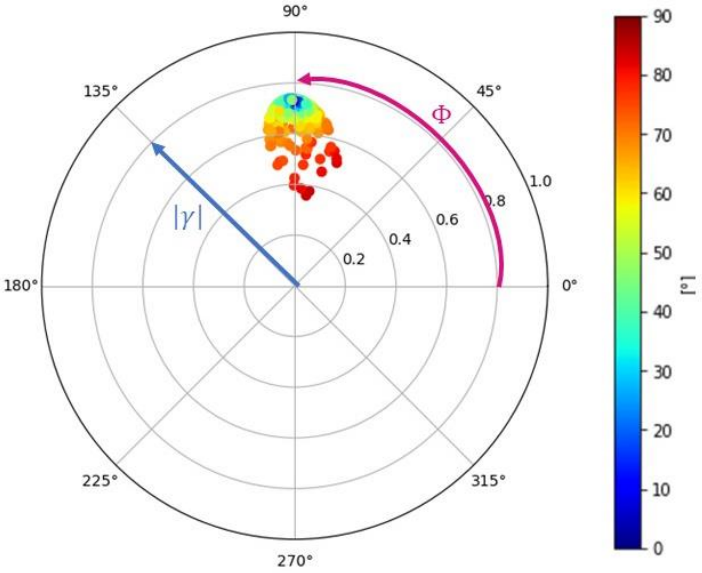

Fig. 5. DPolInSAR coherence for 500 random polarization states (dots) for one location in Inf1 (C band). Colours indicate the α angle of the scattering vector.

Fig. 5 shows such a coherence region for a snow-covered area of Inf1 in C band. It is generated by using 500 randomly sampled polarizations states $\vec{w}$. The interferometric phase is calibrated using a corner reflector in the scene. The radial location of each coherence locus corresponds to the absolute coherence value (blue arrow in Fig. 5), indicating the correlation between the two acquisitions of the interferogram. Its angular location is given by the phase (pink arrow in Fig. 5) of the interferogram formed using the associated polarization. Accordingly, it is related to the SWE change occurring between two acquisitions. It can be observed that there is a certain phase extent of the coherence regions, meaning the interferometric phases at different polarizations are not the same, which is expected after the results in Section 4.3.2.

The color coding of the coherence loci is according to their polarimetric scattering angle alpha, α, expressing the scattering type interpretation of the associated polarization states $\vec{w}$ [41].

$$\alpha = arccos\left(\frac{|s_{HH} + s_{VV}|}{\sqrt{2}\sqrt{|s_{HH}|^2 + |s_{HV}|^2 + |s_{VH}|^2 + |s_{VV}|^2}}\right), \qquad 0° \leq \alpha \leq 90°. \tag{32}$$

Polarization states with α angles close to zero (blueish dots) have high coherence amplitudes, indicating a dominant surface-like underlying scattering, while α angles close to 90° (red dots) have lower coherence values due to a higher Signal to Noise Ratio (SNR) decorrelation contribution.

4.5 DPolInSAR Retrieval

4.5.1 DPolInSAR Coherence Modelling

The DPolInSAR coherence region is modelled according to (31). The underlying scatterer is represented by its covariance matrix $[C_0]$. The propagation matrices $[P_4^i]$ describe the propagation through the snow pack and are defined in (19). The corresponding H and V wavenumbers projected onto snow depth Z are given by (28) and can be modeled in terms of the anisotropy A and density ρ as described in Section 4.3.3. However, (31) does not consider any decorrelation effects that need to be introduced for a realistic modelling of the DPolInSAR coherence region.

Temporal decorrelation due to a non-uniform snow accumulation inside the resolution cell is taken into account, as described in [17] with:

$$\gamma_T = exp\left(-\frac{1}{2}\left(\frac{4\pi}{\lambda}\right)^2 \sigma_s^2 \left(cos\,\Theta - \sqrt{\varepsilon - sin\,\Theta^2}\right)^2\right), \tag{33}$$

where σ_s is the standard deviation of the snow depth inside the resolution cell. Accordingly, γ_T may show a polarization dependency due to the different H and V wavenumbers. However, for small σ_s the effect is nearly the same for all polarizations. Therefore, this yields a constant shift of the absolute coherence values.

The additive noise decorrelation due to low SNR levels [42] is:

$$\gamma_{SNR} = \frac{1}{\sqrt{\left(1+SNR_1^{-1}\right)\left(1+SNR_2^{-1}\right)}}. \tag{34}$$

Since the different polarization states have different signal levels, the SNR decorrelation is not the same for all polarization states, which leads to possibly large variations in absolute coherence within one coherence region, see Fig. 5.

4.5.1.1 Snow Depth Change

First, the effect of a change in snow depth with fixed snow density is discussed for two different anisotropy scenarios. In the first case the anisotropy is set to A=0 (for both acquisitions), corresponding to isotropic snow. In the second case, the anisotropy is set to A=0.2 (for both acquisitions) corresponding to a freshly fallen snow scenario. The snow depth change is set in both cases to $\Delta Z = 9\,cm$. Fig. 6 shows the modelled coherence region for 500 random polarization states $\vec{w}$. The temporal decorrelation is set to $\gamma_T = 0.925$, assuming a $\sigma_s = 1\,cm$, and the SNR decorrelation for a noise level of -20dB is computed. The underlying scattering process was assumed to be a Bragg-like scatterer.

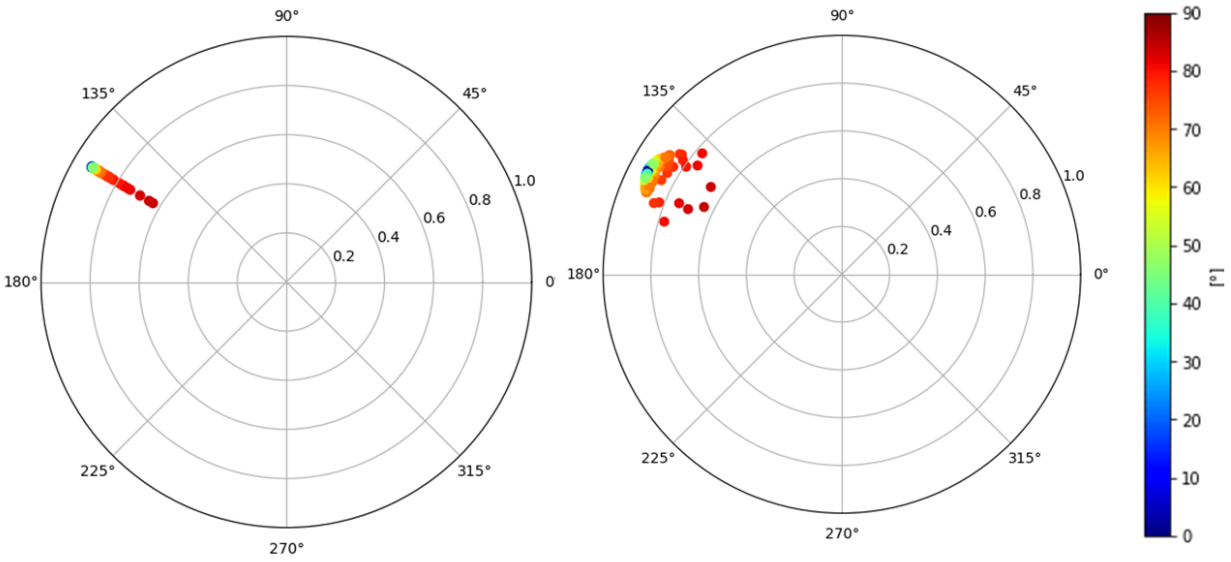

Fig. 6. DPolInSAR coherence region at C band for a snow depth change of $\Delta Z = 9\ cm$ at Θ = 39°. Left: isotropic snow A=0, right: anisotropic snow A=*0.2*. The snow density is assumed $\rho = 0.15\ g/cm^3$. The color coding is according to their polarimetric scattering angle alpha, α.

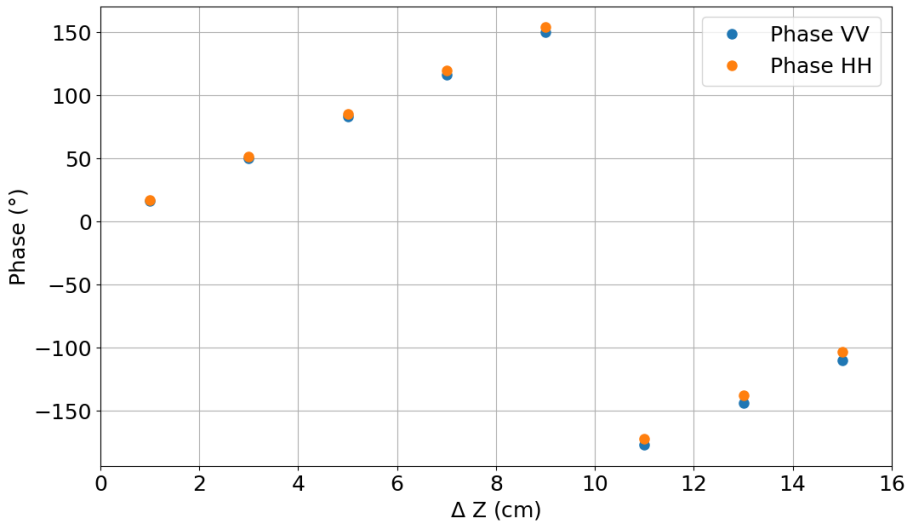

Fig. 7. Interferometric phase of the VV channel (blue) and the HH channel (orange) in dependence of the snow depth change. (C band, $\rho = 0.15\ g/cm^3$, Θ = 39°, A=0.2)

Fig. 6 (left) shows that for the case of isotropic snow, all polarization states have the same phase values. Only the coherence amplitude is decreasing for higher alpha angles due to the SNR decorrelation. The introduction of anisotropy Fig. 6 (right) results in a wider spread of the phase values since the anisotropic structure of the snow is affecting the polarization states differently. The absolute interferometric phase of VV and HH for the second case is shown for different snow depth changes in Fig. 7.

It can be seen that the interferometric phase increases for higher snow depth changes. It wraps at a snow depth change for the HH polarization at $\Delta Z_{HH} = 10.5\ cm$ and for VV at $\Delta Z_{VV} = 10.8\ cm$ for the assumed parameters and then continues to increase. Furthermore, the difference

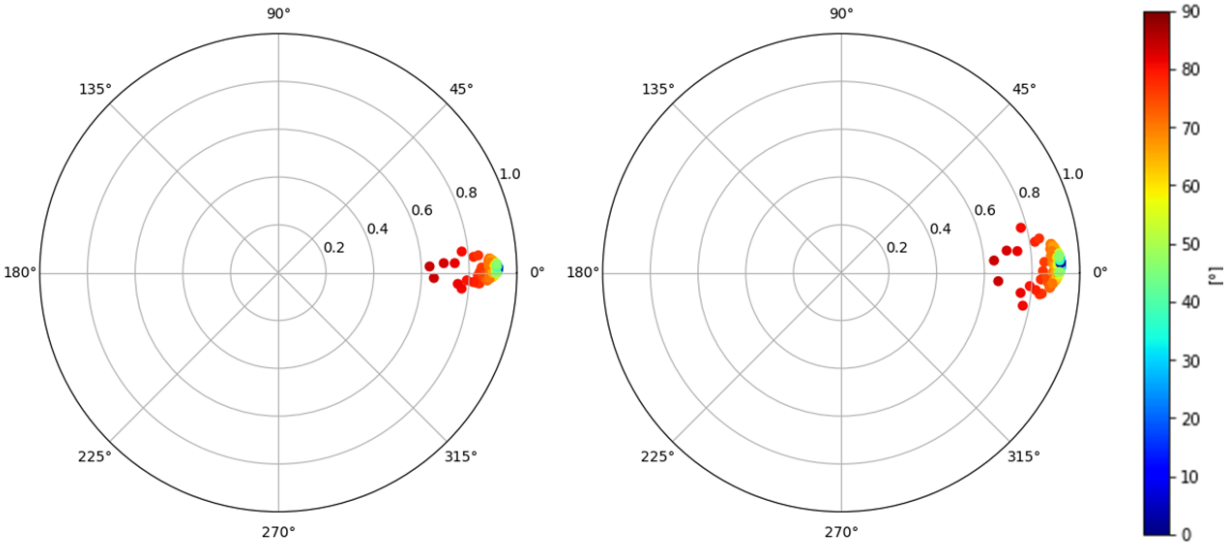

Fig. 8. DPolInSAR coherence region at C band for an anisotropy change for $Z = 9\ cm$ at Θ = 39°. Left: $\Delta A = 0.1$, right: $\Delta A = 0.2$. The snow density is assumed $\rho = 0.15\ g/cm^3$. The color coding is according to their polarimetric scattering angle alpha, α.

between the phases of the HH and VV channel increases with higher snow depth changes. This is due to the fact that for higher snow depths, the radar wave's path delay through the anisotropic snow increases, which also causes a greater path length difference between VV and HH. This is similar to the results presented in Section 4.3.2, where also a discrepancy between VV and HH is observed, which increased for the bigger snow fall event, see Fig. 3. Here, it can be seen again that different SWE change estimates are obtained from the phases of the VV and HH channels when using the conventional single-pol DInSAR retrieval in (3).

4.5.1.2 Anisotropy Change

The influence of a change in the snow microstructure is modelled assuming an anisotropy change between the two acquisitions of $\Delta A = 0.1$ (left) and $\Delta A = 0.2$ in (right) and with a snow depth of $Z = 9\ cm$ in Fig. 8.

An increased anisotropy change mainly results in a larger phase variation within the coherence region, which results from the fact that with higher anisotropies the propagation differs increasingly for the different polarization states. The interferometric phases are shown in more detail in Fig. 9 which also demonstrates a small increase in the absolute phase with increasing phase differences between the VV and HH channel.

The effect on the absolute phase can be explained by the fact, that along with the anisotropy increase also the average permittivity of the whole snow pack increases (see Fig. 4). As a result, so does the DInSAR phase of the VV and HH channels. The increasing difference between the VV and HH channels would again result in different SWE change estimates using (3) depending on the used polarization, showing the importance of considering the polarization information during SWE change retrieval.

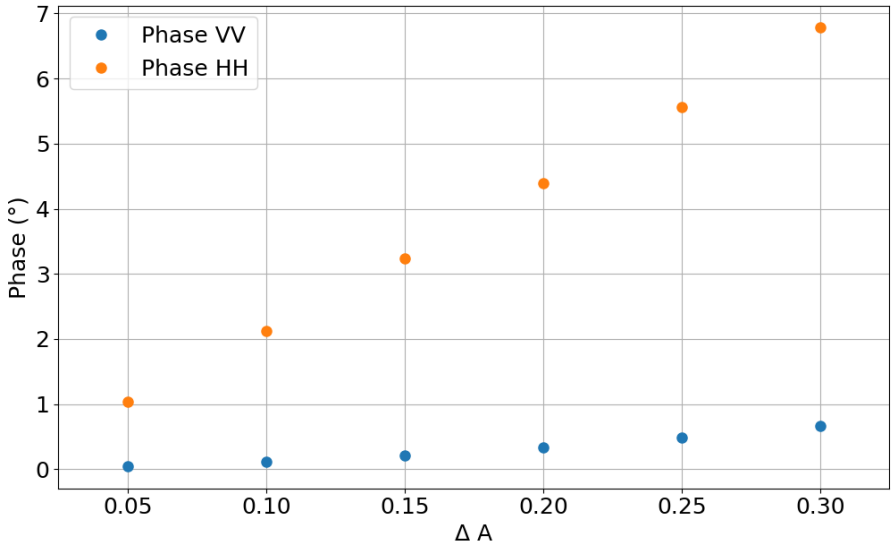

Fig 9. Interferometric phase of the VV channel (blue) and the HH channel (orange) in dependence of the anisotropy change. (C band, $\rho = 0.15\ g/cm^3$, Θ = 39°, Z=9cm)

4.5.2 Retrieval Results

The aim of this study is to use the DPolInSAR coherence regions to retrieve the SWE change between the two measurements. For that, the depth, density and anisotropy changes for the snow change are retrieved. For each pixel, the coherence region using (14) for the data is computed for random polarization states. Then the proposed DPolInSAR model is used to model the DPolInSAR coherences for different combinations of snow depth, density, and anisotropy changes. Here again, the coherence regions for the random polarization states are calculated. Now, the difference between the phases of the n polarization states from the data and the model is computed for all combinations of snow depth, density, and anisotropy changes with the cost function $C(Z, \rho, A)$:

$$C(Z, \rho, A) = \sum_{i=0}^{n} |(\Delta\Phi_{data,i} - \Delta\Phi_{model,i}(Z, \rho, A))|. \quad (35)$$

The goal is to find the minimal difference between the phases of the polarization states from the data and the model. The parameters of this minimum of $C(Z, \rho, A)$ are then the depth, density and anisotropy estimate for the pixel.

In Fig. 10 (top), an example for the 3D cost function $C(Z, \rho, A)$ is visualized. The cost function is ranging from low to high values, with low values having a higher agreement between the data and the model. Different density-depth combinations, which correspond to the same SWE, lead to a line shaped minimum in the density-depth plane, as expected. The 2π phase wrap of the interferometric phase leads to further minima at the corresponding SWE interval. Fig. 10 (bottom)

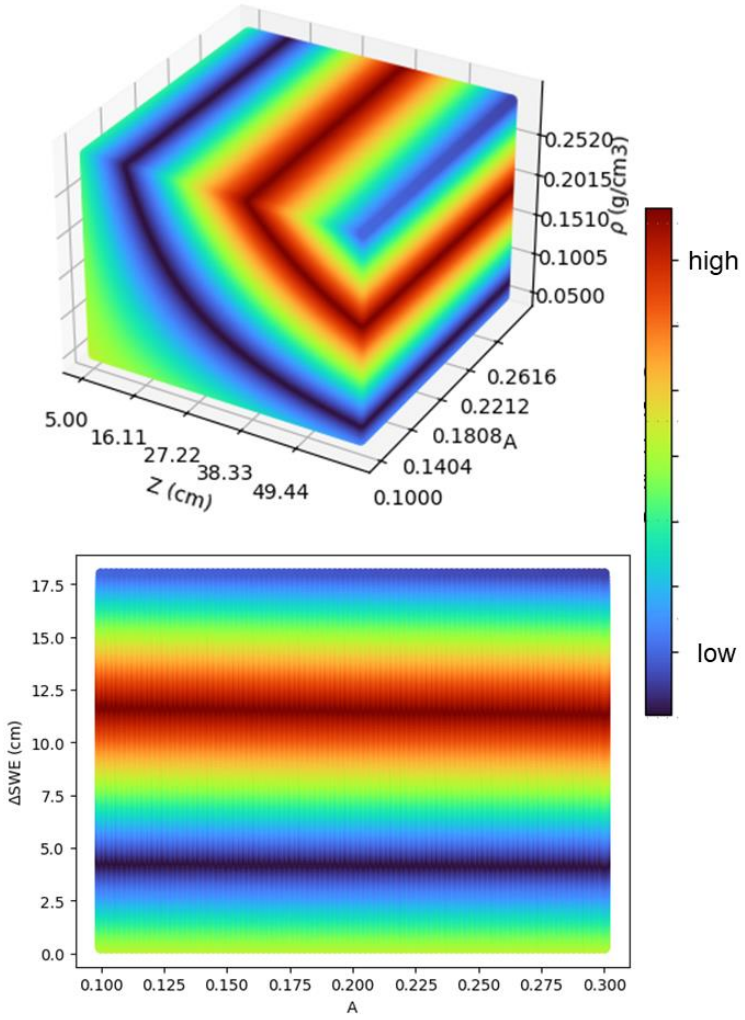

Fig. 10. Cost function for one location in Inf2 using L band. TOP: 3D plot of the cost function in dependence of Z, ρ, A. Bottom: 2D plot of the cost function for ΔSWE and A. Color scale is ranging from low to high values of the cost function.

shows a 2D plot of the cost function in dependence of the SWE and anisotropy. It can be seen more in detail here, that the influence of SWE is much more prominent in the result than the anisotropy estimate. This is also expected after the results in Section 4.5.1, as the snow depth change or SWE change has a bigger effect on the absolute phase than the anisotropy change. Still, also a small effect of the anisotropy is present, which even allows to partly solve the 2π phase ambiguity for larger SWE changes.

The depth and density corresponding to the minima of the cost functions are used to compute the SWE change estimate. Fig. 11 for Inf1 and Fig. 12 for Inf2 show the comparison between the ground measurements and the corresponding estimated SWE change values. Here, the results from the DPolInSAR model inversion (blue) and the SWE changes, which would be obtained from just using the single-pol DInSAR phase in VV (green) and HH (orange) and (3), are displayed in the top for C band and in the bottom for L band.

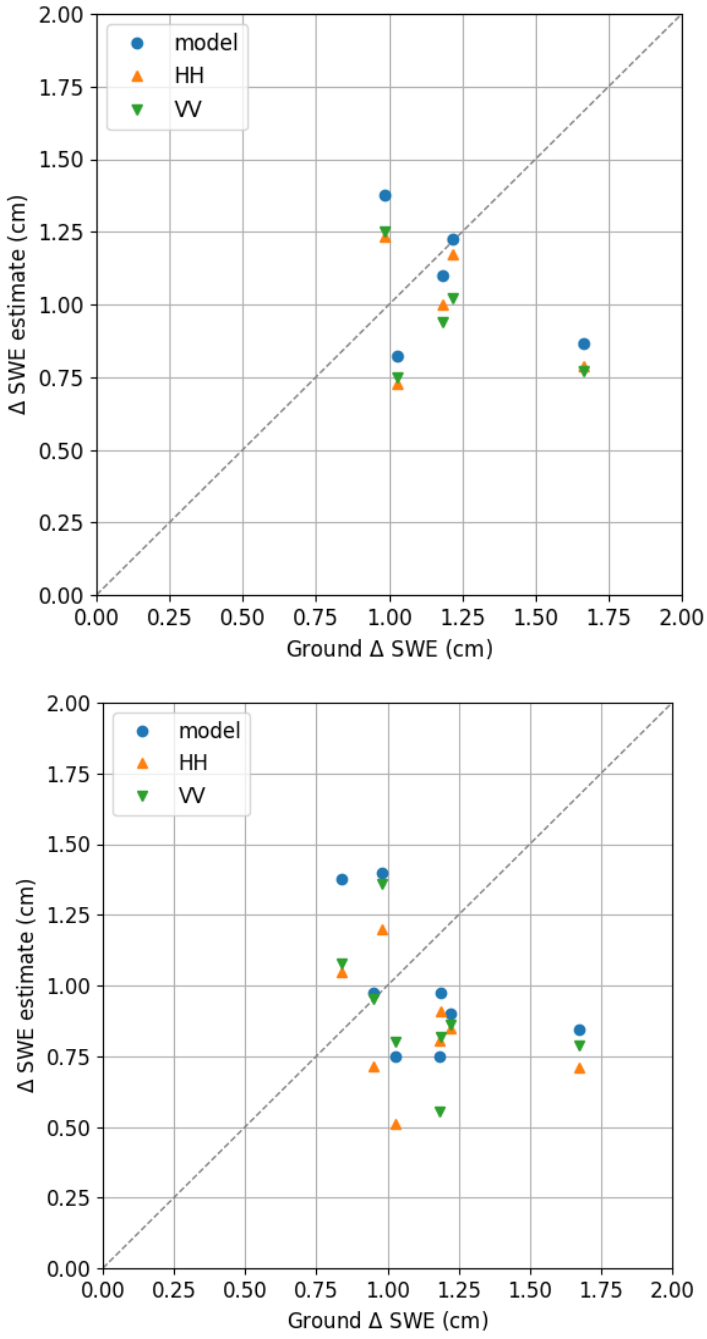

Fig. 11. SWE change estimates of the PolInSAR model (blue), the DInSAR approach using the HH phase (orange), and the DInSAR approach using the VV phase (green) compared to ground based SWE change measurements for Inf1. Top: C band. Bottom: L band.

Note here, that in regions with local slopes, the ground measurements do not align with the local normal. In order to compare them to the retrieved SAR measurements, a factor of $\cos\beta$ is included, with β being the local slope angle [22].

For the small snow fall event in Fig. 11, the results between the different methods do not deviate much for neither C band nor L band. This indicates that both approaches, either using DPolInSAR or a single polarization and (3), agree. Still, the DPolInSAR estimates are slightly better. In the case of the bigger snow fall event, a clear difference between the DPolInSAR

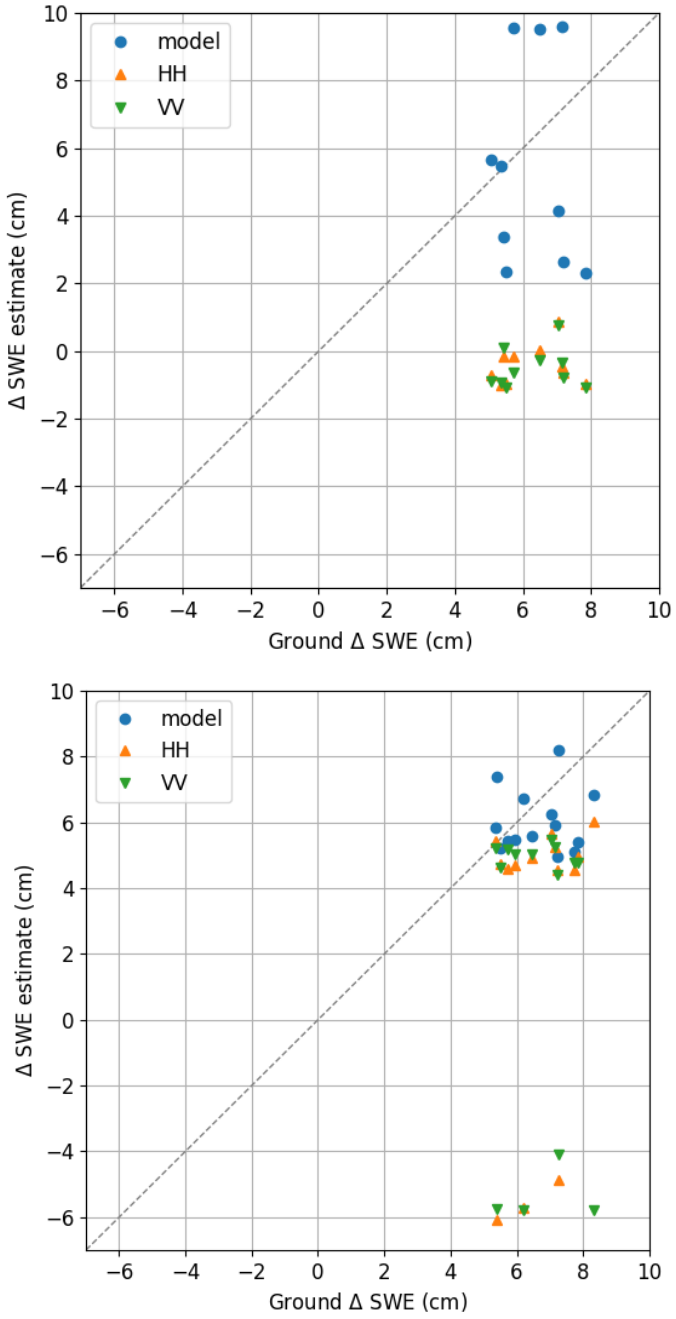

Fig. 12. SWE change estimates of the DPolInSAR model (blue), the DInSAR approach using the HH phase (orange), and the DInSAR approach using the VV phase (green) compared to ground based SWE change measurements for Inf2. Top: C band. Bottom: L band.

estimates and the DInSAR SWE change estimates can be observed (Fig. 12). The DInSAR SWE change estimates are clearly affected by the phase wrap problem. In L band, the DPolInSAR model is able to solve all phase wraps which occur in the DInSAR retrieval (Fig. 12 (bottom)). Also, those estimates which are not affected by a phase wrap are more accurate for the DPolInSAR retrieval. Even though not all phase wraps are resolved correctly for C band using the DPolInSAR approach (Fig. 12 (top)), it is still possible to resolve some phase wraps, improving the accuracy of the SWE change estimates.

TABLE III
RMSE SWE CHANGE ESTIMATES

Frequency	C band		L band	
Interferogram	Inf1	Inf2	Inf1	Inf2
RMSE Model (cm)	0.41	3.22	0.44	1.43
RMSE SWEVV (cm)	0.46	6.86	0.46	6.72
RMSE SWEHH (cm)	0.44	6.76	0.46	5.75

Additionally, Table III shows the RMSEs for the SWE change estimates. In all cases, the SWE change retrieval from the DPolInSAR model inversion performs better than the basic DInSAR model using only one polarization. For the small SWE change event in Inf1, the difference between the RMSEs is quite low. However, for the bigger SWE change event in Inf2, the accuracy improves significantly when using the DPolInSAR model. This indicates that in case of big snow fall events, the model is able to significantly improve the accuracy of the SWE change estimates.

4.6 Discussion

The proposed DPolInSAR model has demonstrated the potential to improve the SWE change estimation compared to the conventional single-pol DInSAR model. However, it is still not possible to completely resolve the phase wrap problem, mentioned in Section 4.3.1. One reason for that is that there is partly an ambiguity between a snow depth change (see Section 4.5.1.1) and an anisotropy change (see Section 4.5.1.2). While for a snow depth change mainly an increase in absolute phase can be observed, in both cases also the phase extent of the coherence region increases. This increase in the phase extent results in an ambiguity, which cannot be solved so far. Nevertheless, using the DPolInSAR model it is still possible to correct for some phase wraps, which is an improvement compared to the DInSAR model, see Fig. 12.

Similar to the conventional DInSAR approach, a limitation is the need of an absolute phase calibration in order to retrieve SWE changes [17]. Therefore, a reference phase is required, which in this study is a corner reflector.

Compared to the conventional DInSAR approach, the DPolInSAR model requires at least copolar measurements in HH and VV. As a consequence, a number of satellites are not suitable for this approach, for example Sentinel-1, because it only performs co-cross polarized measurements [43]. However, the proposed method has potential for spaceborne sensors such as TanDEM-X [44], PAZ [45] and ALOS-2 [46] where dual polarimetric measurements in VV and HH are available, as well as for airborne SAR measurements. Also, upcoming copolar dual polarimetric SAR missions like NISAR [47] could exploit this method.

4.7 Conclusions

This study demonstrates the potential of combining DInSAR and PolSAR into a DPolInSAR model to estimate SWE changes. Depending on whether the interferometric phase of horizontally or vertically polarized channels is used for the single-pol SWE change retrieval, different SWE change estimates are obtained. The difference between the HH and VV estimates increases for higher SWE changes between the interferometric acquisitions. This shows that it is important to include the polarimetric information for a more accurate SWE change retrieval.

In order to not only include, but also to use the additional information of the polarimetric measurements, a DPolInSAR model is introduced. This is achieved by combining existing interferometric and polarimetric snow models to derive DPolInSAR coherence regions. This combined model can be used to simulate temporal coherence regions for varying changes in snow depth and anisotropy, with the goal to understand the influence of snow changes on the coherence region parameters such as absolute phase and phase extent. An increase in snow depth results in an absolute phase change, as well as in an increase in phase extent of the coherence region. Meanwhile, a change in anisotropy primarily results in an increase of the phase extent. By exploiting these features, additional information can be retrieved, compared to the conventional single-pol DInSAR approach.

The PolInSAR model is used to estimate snow changes from airborne SAR measurements by retrieving the parameters for snow depth, density and anisotropy which minimize the difference between measured and modeled coherence regions. In all cases the RMSE between the retrieved and in-situ measured SWE changes improves compared to only using a single polarization. In addition, the proposed DPolInSAR retrieval is able to partly solve the 2π phase wrap issue. Therefore, the proposed approach has potential for application in future dual-pol SAR missions.

4.8 Acknowledgment

The authors would like to thank the F-SAR campaign team for the acquisition of the data and the ground team from ENVEO for collecting in-situ measurements.

4.9 References

[1] T. P. Barnett, J. C. Adam, and D. P. Lettenmaier, “Potential impacts of a warming climate on water availability in snow-dominated regions,” *Nature*, vol. 438, no. 7066, Art. no. 7066, Nov. 2005, doi: 10.1038/nature04141.

[2] S. Jörg-Hess, N. Griessinger, and M. Zappa, “Probabilistic Forecasts of Snow Water Equivalent and Runoff in Mountainous Areas,” *J. Hydrometeorol.*, vol. 16, no. 5, Art. no. 5, Oct. 2015, doi: 10.1175/JHM-D-14-0193.1.

[3] L. Tsang *et al.*, “Review article: Global monitoring of snow water equivalent using high-frequency radar remote sensing,” *The Cryosphere*, vol. 16, no. 9, pp. 3531–3573, Sep. 2022, doi: 10.5194/tc-16-3531-2022.

[4] S. Schilling, A. Dietz, and C. Kuenzer, “Snow Water Equivalent Monitoring—A Review of Large-Scale Remote Sensing Applications,” *Remote Sens.*, vol. 16, no. 6, p. 1085, 2024, doi: 10.3390/rs16061085.

[5] A. Moreira, P. Prats-Iraola, M. Younis, G. Krieger, I. Hajnsek, and K. P. Papathanassiou, “A tutorial on synthetic aperture radar,” *IEEE Geosci. Remote Sens. Mag.*, vol. 1, no. 1, Art. no. 1, Mar. 2013, doi: 10.1109/MGRS.2013.2248301.

[6] J. Koskinen, S. Metsämäki, J. Grandell, S. Jänne, and M. Hallikainen, “Snow Monitoring Using Radar and Optical Satellite Data,” *Remote Sens. Environ.*, vol. 69, no. 1, pp. 16–29, 1999, doi: 10.1016/S0034-4257(99)00010-3.

[7] E. Rignot, K. Echelmeyer, and W. Krabill, “Penetration depth of interferometric synthetic-aperture radar signals in snow and ice,” *Geophys Res Lett*, vol. 28, pp. 3501–3504, Sep. 2001, doi: https://doi.org/10.1029/2000GL012484.

[8] T. Guneriussen, K. A. Hogda, H. Johnsen, and I. Lauknes, “InSAR for estimation of changes in snow water equivalent of dry snow,” *IEEE Trans. Geosci. Remote Sens.*, vol. 39, no. 10, pp. 2101–2108, Oct. 2001, doi: 10.1109/36.957273.

[9] S. Leinss, A. Wiesmann, J. Lemmetyinen, and I. Hajnsek, “Snow Water Equivalent of Dry Snow Measured by Differential Interferometry,” *IEEE J. Sel. Top. Appl. Earth Obs. Remote Sens.*, vol. 8, no. 8, pp. 3773–3790, Aug. 2015, doi: 10.1109/JSTARS.2015.2432031.

[10] J. J. Ruiz *et al.*, “Investigation of Environmental Effects on Coherence Loss in SAR Interferometry for Snow Water Equivalent Retrieval,” *IEEE Trans. Geosci. Remote Sens.*, vol. 60, pp. 1–15, 2022, doi: 10.1109/TGRS.2022.3223760.

[11] H. P. Marshall *et al.*, “L-Band InSAR Depth Retrieval During the NASA SnowEx 2020 Campaign: Grand Mesa, Colorado,” in *2021 IEEE International Geoscience and Remote Sensing Symposium IGARSS*, Brussels, Belgium: IEEE, Jul. 2021, pp. 625–627. doi: 10.1109/IGARSS47720.2021.9553852.

[12] J. Tarricone, R. W. Webb, H.-P. Marshall, A. W. Nolin, and F. J. Meyer, “Estimating snow accumulation and ablation with L-band interferometric synthetic aperture radar (InSAR),” *The Cryosphere*, vol. 17, pp. 1997–2019, 2023, doi: 10.5194/tc-17-1997-2023.

[13] R. T. Palomaki and E. A. Sproles, “Assessment of L-band InSAR snow estimation techniques over a shallow, heterogeneous prairie snowpack,” *Remote Sens. Environ.*, vol. 296, no. 113744, pp. 1–17, 2023, doi: 10.1016/j.rse.2023.113744.

[14] Z. Hoppinen, S. Oveisgharan, H.-P. Marshall, R. Mower, K. Elder, and C. Vuyovich, “Snow water equivalent retrieval over Idaho – Part 2: Using L-band UAVSAR repeat-pass interferometry,” *The Cryosphere*, vol. 18, pp. 575–592, 2024, doi: 10.5194/tc-18-575-2024.

[15] R. Bonnell *et al.*, “Evaluating L-band InSAR snow water equivalent retrievals with repeat ground-penetrating radar and terrestrial lidar surveys in northern Colorado,” *The Cryosphere*, vol. 18, no. 8, pp. 3765–3785, 2024, doi: 10.5194/tc-18-3765-2024.

[16] T. Nagler *et al.*, "Airborne Experiment on Insar Snow Mass Retrieval in Alpine Environment," *IGARSS 2022-2022 IEEE Int. Geosci. Remote Sens. Symp.*, pp. 4549–4552, Jul. 2022, doi: 10.1109/IGARSS46834.2022.9883809.

[17] H. Rott, T. Nagler, and R. Scheiber, "Snow Mass Retrieval by Means of SAR Interferometry," in *Proc. of FRINGE 2003 Workshop*, Italy, 2003, pp. 1–6.

[18] H. Li, Z. Wang, G. He, and W. Man, "Estimating Snow Depth and Snow Water Equivalence Using Repeat-Pass Interferometric SAR in the Northern Piedmont Region of the Tianshan Mountains," *J. Sens.*, vol. 2017, pp. 1–17, 2017, doi: 10.1155/2017/8739598.

[19] V. Conde, C. Nico, P. Mateus, J. Catalao, A. Kontu, and M. Gritsevich, "On the estimation of temporal changes of snow water equivalent by spaceborne SAR interferometry: a new application for the Sentinel-1 mission," *J. Hydrol. Hydromech.*, vol. 67, no. 1, Art. no. 1, 2019, doi: 10.2478/johh-2018-0003.

[20] A. B. Mahmoodzada, "Capability assessment of Sentinel-1 data for estimation of snow hydrological potential in the Khanabad watershed in the Hindu Kush Himalayas of Afghanistan," *Remote Sens. Appl. Soc. Environ.*, vol. 26, no. 100758, pp. 1–11, 2022, doi: 10.1016/j.rsase.2022.100758.

[21] S. Oveisgharan, R. Zinke, Z. Hoppinen, and H. P. Marshall, "Snow water equivalent retrieval over Idaho – Part 1: Using Sentinel-1 repeat-pass interferometry," *The Cryosphere*, vol. 18, no. 2, pp. 559–574, 2024, doi: 10.5194/tc-18-559-2024.

[22] J. Eppler, B. Rabus, and P. Morse, "Snow water equivalent change mapping from slope-correlated synthetic aperture radar interferometry (InSAR) phase variations," *The Cryosphere*, vol. 16, no. 4, pp. 1497–1521, 2022, doi: 10.5194/tc-16-1497-2022.

[23] P. N. Dagurov, T. N. Chimitdorzhiev, A. V. Dmitriev, and S. I. Dobrynin, "Estimation of snow water equivalent from L-band radar interferometry: simulation and experiment," *Int. J. Remote Sens.*, vol. 41, no. 24, pp. 9328–9359, Dec. 2020, doi: 10.1080/01431161.2020.1798551.

[24] J. J. Ruiz, J. Lemmetyinen, J. Cohen, A. Kontu, T. Nagler, and J. Pulliainen, "Comparing InSAR Snow Water Equivalent Retrieval Using ALOS2 With In Situ Observations and SnowModel Over the Boreal Forest Area," *IEEE Trans. Geosci. Remote Sens.*, vol. 62, pp. 1–14, 2024, doi: 10.1109/TGRS.2024.3439855.

[25] A. Benedikter, M. Rodriguez-Cassola, P. Prats-Iraola, K. Belinska, and G. Krieger, "On the Decorrelation Effect of Dry Snow in Differential SAR Interferometry," *IGARSS 2023-2023 IEEE Int. Geosci. Remote Sens. Symp.*, pp. 8323–8326, 2023, doi: 10.1109/IGARSS52108.2023.10282149.

[26] K. Belinska, G. Fischer, G. Parrella, and I. Hajnsek, "The Potential of Multifrequency Spaceborne DInSAR Measurements for the Retrieval of Snow Water Equivalent," *IEEE J. Sel. Top. Appl. Earth Obs. Remote Sens.*, vol. 17, pp. 2950–2962, 2023, doi: 10.1109/JSTARS.2023.3345139.

[27] H. Lievens *et al.*, "Snow depth variability in the Northern Hemisphere mountains observed from space," *Nat. Commun.*, vol. 10, pp. 1–12, 2019, doi: 10.1038/s41467-019-12566-y.

[28] H. Lievens, I. Brangers, H.-P. Marshall, T. Jonas, M. Olefs, and G. D. Lannoy, "Sentinel-1 snow depth retrieval at sub-kilometer resolution over the European Alps," *The Cryosphere*, vol. 16, no. 1, pp. 159–177, 2022, doi: 10.5194/tc-16-159-2022.

[29] S. Leinss, G. Parrella, and I. Hajnsek, "Snow Height Determination by Polarimetric Phase Differences in X-Band SAR Data," *IEEE J. Sel. Top. Appl. Earth Obs. Remote Sens.*, vol. 7, no. 9, Art. no. 9, Sep. 2014, doi: 10.1109/JSTARS.2014.2323199.

[30] JP. Dedieu *et al.*, "Improvement of snow physical parameters retrieval using SAR data in the Arctic (Svalbard)," ISSW, Oct. 2018.

[31] J. Voglimacci-Stephanopoli *et al.*, “Potential of X-band polarimetric synthetic aperture radar co-polar phase difference for arctic snow depth estimation,” *The Cryosphere*, vol. 16, pp. 2163–2181, 2022, doi: 10.5194/tc-16-2163-2022.

[32] S. Leinss, H. Löwe, M. Proksch, J. Lemmetyinen, A. Wiesmann, and I. Hajnsek, “Anisotropy of seasonal snow measured by polarimetric phase differences in radar time series,” *The Cryosphere*, vol. 10, no. 4, Art. no. 4, Aug. 2016, doi: 10.5194/tc-10-1771-2016.

[33] S. Majumdar, P. K. Thakur, L. Chang, and S. Kumar, “X-Band Polarimetric Sar Copolar Phase Difference for Fresh Snow Depth Estimation in the Northwestern Himalayan Watershed,” in *IGARSS 2019 - 2019 IEEE International Geoscience and Remote Sensing Symposium*, Yokohama, Japan: IEEE, Jul. 2019, pp. 4102–4105. doi: 10.1109/IGARSS.2019.8898884.

[34] A. Patil, G. Singh, and C. Rüdiger, “Retrieval of Snow Depth and Snow Water Equivalent Using Dual Polarization SAR Data,” *Remote Sens.*, vol. 12, no. 7, Art. no. 7, Apr. 2020, doi: 10.3390/rs12071183.

[35] K. Belinska, G. Fischer, and I. Hajnsek, “Combining Differential SAR Interferometry and Copolar Phase Differences for Snow Water Equivalent Estimation,” *IEEE Geosci. Remote Sens. Lett.*, vol. 21, no. 2001505, 2024, doi: 10.1109/LGRS.2024.3461229.

[36] M. Stefko, P. Bernhard, O. Frey, and I. Hajnsek, “Polarimetric Analysis of Biseasonal Monostatic and Bistatic Radar Observations of a Glacier Accumulation Zone at Ku-Band,” *IEEE J. Sel. Top. Appl. Earth Obs. Remote Sens.*, vol. 17, pp. 9706–9727, 2024, doi: 10.1109/JSTARS.2024.3374051.

[37] V. Grachea, R. Horn, T. Nagler, and J. Fischer, “SARSimHT-NG – Simulation of Hydroterra SAR System Performance in the Mediterranean and the Alps Based on Experimental Airborne SAR Data,” DLR, Enveo, ESA Airborne Campaign 2021-2022.

[38] A. Wiesmann and C. Mätzler, “Microwave Emission Model of Layered Snowpacks,” *Remote Sens. Environ.*, vol. 70, no. 3, pp. 307–316, 1999, doi: https://doi.org/10.1016/S0034-4257(99)00046-2.

[39] C. Mätzler, “Microwave sensors for measuring avalanche-critical snow parameters,” *IAHS Publ*, vol. Avalanche Formation, Movement and Effects, no. 162, Art. no. 162, 1987.

[40] A. Sihvola, “Mixing Rules with Complex Dielectric Coefficients,” *Subsurf. Sens. Technol. Appl.*, vol. 1, no. 4, pp. 393–415, 2000, doi: https://doi.org/10.1023/A:1026511515005.

[41] S. Cloude, *Polarisation: applications in remote sensing*, 1st ed. Oxford ; New York: Oxford University Press, 2010.

[42] D. Just and R. Bamler, “Phase statistics of interferograms with applications to synthetic aperture radar,” *Appl. Opt.*, vol. 33, no. 20, pp. 4361–4368, 1994.

[43] P. Potin, P. Bargellini, H. Laur, B. Rosich, and S. Schmuck, “Sentinel-1 mission operations concept,” *2012 IEEE Int. Geosci. Remote Sens. Symp.*, pp. 1745–1748, 2012, doi: 10.1109/IGARSS.2012.6351183.

[44] G. Krieger *et al.*, “TanDEM-X: A Satellite Formation for High-Resolution SAR Interferometry,” *IEEE Trans. Geosci. Remote Sens.*, vol. 45, no. 11, pp. 3317–3341, 2007, doi: 10.1109/TGRS.2007.900693.

[45] A. Alonso-González *et al.*, “Joint PAZ & TanDEM-X Mission Interferometric Experiments: Interoperability and Products,” *IEEE J. Sel. Top. Appl. Earth Obs. Remote Sens.*, vol. 14, pp. 6069–6082, 2021, doi: 10.1109/JSTARS.2021.3084401.

[46] Y. Kankaku, S. Suzuki, and Y. Osawa, “ALOS-2 mission and development status,” *2013 IEEE Int. Geosci. Remote Sens. Symp. - IGARSS*, pp. 2396–2399, 2013, doi: 10.1109/IGARSS.2013.6723302.

[47] K. Kellogg *et al.*, “NASA-ISRO Synthetic Aperture Radar (NISAR) Mission,” in *2020 IEEE Aerospace Conference*, Big Sky, MT, USA: IEEE, Mar. 2020, pp. 1–21. doi: 10.1109/AERO47225.2020.9172638.

5 Conclusions

The main goal of this thesis is to analyze and improve the accuracy of interferometric SWE change retrieval by exploiting multifrequency data as well as polarimetric SAR measurements. The relevant studies, which were described in Chapters 2 to 4, are summarized and discussed with respect to the research goals of this thesis in the following sections.

Firstly, Section 5.1 summarizes the applied methods and the conducted analyses. In Section 5.2, the results and conclusions are outlined by answering the research questions of this thesis. Finally, Section 5.3 gives an outlook, which puts a focus on the possible use cases of the proposed approaches, remaining limitations, and potential research objectives in the future.

5.1 Summary

Chapter 1 *'Introduction'* introduces the topic and presents the background for the SAR techniques utilized in this thesis. The main focus lies on interferometric and polarimetric SAR methods. The microwave interaction with the snow pack is governed by its dielectric properties. This is used in a DInSAR SWE change retrieval, which utilizes the snow-induced phase difference to estimate the SWE change. Polarimetric measurements can be linked to the amount of snow by exploiting the phase difference between vertical and horizontal polarizations, the CPD. This chapter also introduces the research objectives and questions of this thesis, which aim at the improvement of the SWE change retrieval combining both DInSAR and polarimetric information.

In Chapter 2 *'The Potential of Multifrequency Spaceborne DInSAR Measurements for the Retrieval of Snow Water Equivalent'*, an existing SWE change retrieval method is applied to spaceborne SAR measurements with different frequencies over a test site in Finland in order to assess their respective potentials and limitations. For that, three different SAR sensors are investigated. For X-band, TanDEM-X data is used, while the Sentinel-1 dataset contains C-band SAR measurements and, ALOS-2 provides L-band acquisitions. Interferometric processing of the data is performed and the coherence and phase are calculated for short time series, which are then used to estimate the SWE changes between the measurements. The analysis highlights the known issues of the temporal decorrelation, which are related to snow melt, high frequencies, long revisit times, and the frequency-dependent appearance of phase wrap issues. In order to investigate phase wraps, ground-based measurements are used for their detection and to quantify the number of missing phase cycles. In the first step, this ground-based information is used to correct the DInSAR SWE change retrieval results by addition of missing phase cycles. In a second step, SWE estimates from different frequencies are combined. Here, frequencies which are less affected by phase wraps (i.e. longer wavelengths) are used to detect and correct phase wraps of frequencies that have a lower phase wrap threshold (i.e. shorter wavelengths).

Chapter 3 *'Combining Differential SAR Interferometry and Copolar Phase Differences for Snow Water Equivalent Estimation'* combines the DInSAR SWE change retrieval with CPD

measurements of the two SAR acquisitions. For that, polarimetric C- and L-band data from DLR's airborne radar system F-SAR are used. The flight campaign took place in Austria and was accompanied by ground-based measurements of snow properties, as well as the set-up of corner reflectors, which were used to create a reference phase. The differential interferometric phase is used to estimate the SWE change. Due to the fact, that the CPD can be related to the depth of fresh snow using an established model, an approach is presented that includes the CPD changes between two acquisitions to check whether the SWE change exceeded the phase wrap threshold and to reconstruct the missing phase cycles. The missing phase cycles are then corrected in the DInSAR SWE change estimate to achieve an improved SWE retrieval performance.

Chapter 4 *'Exploring DPolInSAR Coherence Regions for Snow Water Equivalent Estimation'* proposes a combination of interferometric and polarimetric measurements in a DPolInSAR approach. Here, the data from the same airborne campaign as described in Chapter 3 was used. By establishing a unified polarimetric interferometric model, the temporal polarimetric coherence for different polarization states can be simulated and displayed as coherence regions. This allows taking into account that the propagation of radar waves inside the snow pack depends on the polarization, and different snow changes and their effects on the temporal coherence region are analyzed. The temporal coherence regions of the data are calculated and compared to the model. The parameters for snow depth, density and anisotropy are estimated by minimizing the phase differences between model and data.

5.2 Main Findings

In the following, the results and conclusions will be summarized by addressing the research questions formulated in Chapter 1.6:

- **What are the performance tradeoffs of the DInSAR SWE change retrieval algorithm between different spaceborne SAR sensors with different frequencies?**

  An existing DInSAR SWE change retrieval was analyzed for spaceborne SAR measurements in X-, C- and L-band in Chapter 2. The coherence amplitudes were low for X-band, due to the 11 day repeat cycle, but had particularly low values for interferograms measured around dates with high temperature gradients. Especially the winter for which the C- and L-band data was analyzed was often affected by temperatures above 0 degrees and melt events likely occurred between the acquisition dates. This prevents the radar wave to penetrate through the entire snowpack and might have introduced errors in the SWE change estimation. This can also be a reason for low coherences. As the coherence amplitude can be used as a measure for phase noise, this increases also the phase standard deviation.

  An important issue which affects the performance of the SWE change retrieval for all spaceborne SAR measurements is the calibration of the interferometric phase.

Errors in the reference phase directly affect the estimation results. In the presented study, the phase was calibrated using a stable scatterer close to the test site. However, it cannot be guaranteed that the stable scatterer was snow free in this case. Therefore, the presence of snow might have influenced the reference phase.

For short wavelengths, such as X-band, one of the main limitations are the wraps of the interferometric phase. The interval in which SWE change can be retrieved unambiguously, i.e. before a phase wrap occurs, depends on the wavelength and is smaller for shorter wavelengths. In the investigated winter, this threshold was exceeded many times, partly due to the long temporal baseline of 11 days. Even the C-band measurements with a shorter 6 days temporal baseline were affected. On the other hand, the L-band measurements with a 14 days temporal baseline did not exceed the phase wrap threshold indicating the usefulness of lower frequencies for unambiguous SWE change retrievals. However, a longer wavelength comes at the cost of a lower SWE change accuracy.

The above-mentioned temporal baselines not only affect the likelihood of phase wraps, but severely impact the temporal decorrelation with the associated coherence loss. The 11 days baseline at X-band often led to very low coherences with barely useable phase information. However, under very stable conditions some interferograms showed coherences above 0.6. Even though 6 days at C-band and 14 days at L-band theoretically favor higher coherences and thus more reliable phase information, the particular warm winter with many melt events often led to very low coherences as well. While it is known that shorter temporal baselines and longer wavelengths are favorable, these results demonstrate that also the opposite settings can yield useful information and that the overall DInSAR SWE retrieval depends on the stability of the snow conditions.

When ground measurements are used to correct the missing phase cycles in X- and C-band, the RMSE between the X- and C-band estimates and the ground measurements improves significantly. In absolute terms, the RMSE is smallest for the X-band SWE change estimates after correction and has therefore the sensitivity to retrieve small changes. However, the dependence on the phase wrap corrections is the highest in this case. With respect to the RMSE relative to the phase wrap interval for each frequency, L-band has the best performance.

In conclusion, longer wavelengths can be used to retrieve greater SWE changes without the need to compensate missing phase cycles and have the best performance relative to the phase wrap interval. However, when it is possible to correct the missing phase cycles, the accuracy increases for shorter wavelengths, indicating the potential for a multifrequency SWE change estimation approach.

- **Are there ways to solve the interferometric phase wrap problem in the DInSAR SWE retrieval and which data dimensions are required for this?**

Two approaches to solve the interferometric phase wraps are presented in this thesis. The first exploits measurements at different frequencies and the second at different polarizations. For comparison, interferometric phase wraps were also corrected using ground measurements.

The phase wraps of the interferometric phase, which affect the performance of the SWE change retrieval, depend on the amount of SWE change and on the frequency of the radar wave. The multifrequency approach presented in Chapter 2 combines the SWE change estimates from two different frequencies. It exploits the fact that ΔSWE estimates retrieved from measurements with longer wavelengths are less affected by phase wraps than shorter wavelengths.

The results of the SWE change retrieval using the multifrequency approach improved compared to the case when no correction of the phase wraps was applied. This means that the retrieval based on a longer wavelength was able to detect phase wraps that occurred in the shorter-wavelength retrieval.

However, using ground measurements for phase wrap correction yielded an even higher accuracy than using the multifrequency approach. One limitation in this study was that the C- and L-band measurements were acquired in the same winter, but not at the same dates and at the same temporal baseline. To compensate for this, SWE values were approximated by linear interpolation between the measurement dates, which may have introduced some discrepancies. Another reason for the lower accuracy may have been temperatures above zero degrees and associated melt events.

Nevertheless, the multifrequency approach increased the accuracy compared to not correcting the phase wraps at all. This demonstrates that it is possible to solve phase wraps and thus to exploit the high sensitivity of short wavelengths in combination with the increased unambiguous phase interval of longer wavelengths.

Polarimetry is an alternative approach to address the issue of phase wraps during SWE change retrieval. A method is presented in Chapter 3 that includes CPD differences in the SWE change retrieval. The difference between the CPD at the first acquisition and the CPD at the second acquisition can be linked to the snow depth change between them, if the snow density and anisotropy parameter are assumed. This snow depth change in combination with the density assumption is used to check whether phase wraps have to be corrected in the DInSAR SWE change estimates. The advantage of the CPD is that CPD phase wraps are not expected even for large changes in snow depth. However, the sensitivity of the CPD phase to SWE changes is lower than in the DInSAR case, which is why it is only used as a proxy to detect potential phase wraps in the DInSAR SWE change estimates.

The experiments demonstrated that the accuracy of the DInSAR SWE change retrieval can be improved using the CPD. This underlines that the CPD change between the measurements can be used as an approximation for the phase wrap correction without the need of using ground measurements.

Again, when ground measurements are used for phase wrap correction, a higher accuracy is achieved compared to the CPD-based correction. Obviously, the underlying CPD model is a strong approximation of the real snow microstructure and does not account for all natural changes. Bulk assumptions on the snow density and anisotropy are required, which affects the accuracy of the retrieval. Furthermore, due to the temporal baseline between the measurements, snow metamorphism may occur, which affects the CPD but is not accounted for in the model. This and a SWE change both have an impact on the CPD change between the measurements, which leads to ambiguous CPD information.

Nevertheless, the phase wrap correction using the CPD change partly enables the detection and correction of phase wraps and is therefore able to improve the accuracy of the SWE change retrieval compared to the conventional DInSAR approach without correction. The polarimetric information contained in the CPD is also used implicitly in the DPolInSAR retrieval in Chapter 4 where it also allows to account for phase wraps.

- **How can interferometric and polarimetric SAR measurements be combined in a unified DPolInSAR model?**

Interferometric and polarimetric measurements are combined in a DPolInSAR model as presented in Chapter 4. This is done by modeling polarimetric scattering matrices for two SAR images acquired at different times. The influence of the snow is included using propagation matrices, which take into account the different permittivities for vertically and horizontally polarized radar waves. This has the advantage that polarimetry is directly included and potentially allows to correctly model the polarization dependency of the radar wave traveling through the snow pack. The model requires snow depth, density, anisotropy and the underlying scattering mechanism of the surface below the snow pack as input parameters. This makes the model applicable to a wide range of snow change scenarios. The modeled scattering matrices are used to calculate the DPolInSAR coherences for different polarization states, which contain polarimetric as well as interferometric information. The absolute values of the DInSAR coherence correspond to the absolute coherence of a specific polarization state. Depending on how decorrelation effects affect the different polarization states, differences between the polarization states can be observed, revealing information that would not have been available using only one polarization. The phase contains the interferometric phase information for each polarization state,

which can be related to the snow change parameters. Since the polarimetric information is included in the model, the phase of all polarization states can be related to the same snow parameters, making it consistent compared to using the single polarization approach for different polarizations.

- **What is the added value of polarimetric phase information in the DInSAR SWE change algorithm?**

In the conventional DInSAR SWE change retrieval, no polarization dependency is taken into account. Therefore, the estimated SWE changes can differ for the same scene depending on whether, e.g., vertical or horizontal polarization was used for the estimation. The analysis of the polarization dependence in Chapter 4 reveals that the difference of the SWE change estimates of the vertical or horizontal polarization can potentially be neglected for small SWE changes. Here, a difference of 0.14 cm was detected for a SWE change event of approximately 1.15 cm. However, this discrepancy between the SWE change estimates of the vertical or horizontal polarization increases with higher SWE changes and needs to be considered for a more accurate SWE change retrieval.

The approach presented in Chapter 3 takes advantage of the phase difference between the horizontal and vertical polarization. The CPD difference between two SAR acquisitions contains information about the snow change between them. This information can be used as an estimation for missing DInSAR phase cycles and therefore adds additional information to the retrieval.

In order to further exploit polarimetric information, the DPolInSAR model is introduced in Chapter 4, which can be employed to simulate temporal coherences for different polarization states. A snow depth increase results in an absolute phase increase for all polarization states, but also in an increase of the phase extent of the coherence region for anisotropic snow. This reveals the phase differences for different polarizations states, which would not be accounted for in the single polarization DInSAR SWE change retrieval. When the anisotropy is increased, primarily the phase extent is increasing, while the effect on the absolute phase is rather small. However, this effect of an anisotropy change on the absolute phase would be misinterpreted as a SWE change in the DInSAR retrieval.

As different snow parameter changes and underlying surfaces have an, although partly ambiguous, effect on the coherence region, its parameters may be used to retrieve them. These can then add information to the SWE change retrieval making it more robust.

- **Can the DPolInSAR model improve the SWE change retrieval?**

  The DPolInSAR model from Chapter 4 can be used to retrieve the SWE change. This is done by finding the parameters for snow depth, density and anisotropy that minimize the phase differences for the investigated polarization states between the model and the data. The snow depth and density estimates provide the SWE change estimate. In a direct comparison with the two DInSAR models using vertical and horizontal polarization, respectively, the DPolInSAR model achieves the highest accuracy.

  One advantage of the DPolInSAR model is that the polarization dependence of the DInSAR phase is not an error source as in the single-polarization case, but is explicitly considered as an information source. Furthermore, consistent SWE values can be retrieved for all polarizations as the polarization dependency of the radar wave is included. However, the model relies on assumptions, which might not describe a real snowpack completely accurately. Moreover, the DPolInSAR retrieval is able to partly solve the phase wraps of the measured phase as snow depth and anisotropy are considered jointly. However, it is not possible to solve all phase wraps. This may be due to the fact that both snow depth and anisotropy change have a partly ambiguous effect on the absolute phase and the phase extent of the coherence region, which is an error source in the retrieval.

5.3 Outlook

Although it was possible to present methods that address some limitations of SAR-based SWE change estimation, the investigations in this thesis also highlighted some important issues and open questions pertaining to SWE change retrieval.

SWE change estimation requires consideration on which SAR data is suitable for which test site. TanDEM-X [1] X-band data with an 11 day repeat cycle might be not suitable for regions with very high SWE changes, as this would cause many phase wraps and a decorrelation of the signal. Here ALOS-2 [2] data with a temporal baseline of 14 days in L-band might be a better choice or Sentinel-1 [3] C-band data with a 12 day repeat cycle. A possibility for X-band data might be the combination of TanDEM-X and PAZ [4], as here temporal baselines of 7 and 4 days can be achieved. In the future, large SWE changes could be also measured with the upcoming NISAR [5] mission, which will acquire measurements at L-band and S-band every 12 days. A further opportunity will be L-band measurements from ROSE-L [6] with a repeat cycle of 12 days.

In order to further investigate the multifrequency phase wrap correction approach, multifrequency measurements acquired at the same time would be immensely beneficial. This will ensure consistency in weather and snow conditions. Furthermore, the use of identical temporal baselines would enhance the comparability of the results. For airborne SAR

measurements, the DLR's system FSAR would be a suitable candidate, which is able to acquire measurements at X-, C- and L-band simultaneously [7]. In the spaceborne case, the upcoming NISAR mission would be suitable. In this case, L-band measurements can be used to correct the more sensitive S-band SWE change estimates. An additional opportunity in the future will be the combination of Sentinel-1 C-band measurements with L-band acquisitions from ROSE-L. The orbits of both satellite systems are identical and have only a small temporal separation. The combination of these missions could benefit from the multifrequency phase wrap correction to provide the sensitivity of shorter wavelengths for SWE change estimation while being more robust to phase wraps that occur due to high SWE changes. Also, more direct combinations or data fusion of multifrequency measurements are worth investigating, by not only considering it for a phase wrap correction, but by exploring ways of exploiting the full information of the measurements at all frequencies while carefully considering their different sensitivities and inaccuracies.

In order to exploit CPD changes for phase wrap correction, dual polarimetric measurements in VV and HH are needed. Therefore, this approach may be applied for airborne sensors, such as F-SAR, but also in current spaceborne missions such as TanDEM-X, PAZ, and ALOS-2, as well as for NISAR data in the future. Here, the results will depend on assumptions on the snowpack, and this approach might be more suitable for regions where the snow properties are approximately known. For the general assumptions used in this thesis, an improvement of the accuracy of the SWE change estimates was observed. Therefore, this approach may still be used as a proxy for phase wrap correction with low computational effort when no ground measurements are available.

A more complex approach is the DPolInSAR model. Here, a next step will be the analysis of which polarization states or coherence region parameters of the DPolInSAR model are needed in order to successfully retrieve the SWE change for computational efficiency. So far, only the phase information between the data and model was compared. In the future, a potential approach can be to focus also on the absolute coherence values for the retrieval in order to have a larger observation space and achieve a higher accuracy. Furthermore, studies have shown that scattering inside the snow pack might occur even for C-band frequencies [8], which is not yet considered in the DPolInSAR model. This can be investigated by including models that describe scattering inside the snow pack [9] in the DPolInSAR model and by analyzing how the coherence region parameters are changing accordingly. Finally, a more robust SWE change retrieval could potentially be achieved by also including multifrequency information in the DPolInSAR model.

One of the main limitations affecting the SWE change retrieval is the calibration of the interferometric phase. In Chapter 3 and Chapter 4 the phase of a corner reflector located in the scene was utilized to this end. It was ensured that the corner reflector was not covered with snow during the measurements, making it suitable for phase calibration. Due to the fact that no corner reflector was available in the study presented in Chapter 2, a stable scatterer was used. In future SAR applications for SWE change estimations, the phase calibration is a major limitation, particularly in areas where no reference phase can be measured.

In future experiments, the characteristics of the test site need to be considered, although this aspect was not the focus of this thesis. The presence of trees inside the resolution cell may affect

the SWE change estimates and is an important factor when choosing the multilooking-window size. Here, a forest mask may be used to mark the location of trees [10].

Additionally, meteorological conditions are affecting the SWE change retrieval. At temperatures above zero degrees melting of the snow surface may occur. This may result in wet snow or the formation of an ice layer by the time the second acquisition is made for the interferogram. This would prevent the radar wave to penetrate through the entire snowpack which is a prerequisite for the SWE change retrieval using the interferometric phase change. Therefore, it is important for future applications to take temperature conditions into account and to generate a wet snow map to differentiate dry and wet snow [11].

The investigations in this thesis aim to enable a more accurate SWE change retrieval using SAR data. Remotely-sensed SWE from SAR data has the potential to provide information of this important parameter continuously at large spatial scales and high temporal and spatial resolution. This would reduce the dependency on ground-based measurements, the spatial interpolation of which can introduce significant errors in regions with a low density of measurement sites. Remotely-sensed SWE estimates can then be used as an input parameter to improve climate and hydrological models, for example to enable more accurate runoff predictions. These will be invaluable for water resource management and planning, particularly in the context of a changing climate.

5.4 References

[1] G. Krieger *et al.*, "TanDEM-X: A Satellite Formation for High-Resolution SAR Interferometry," *IEEE Trans. Geosci. Remote Sens.*, vol. 45, no. 11, pp. 3317–3341, 2007, doi: 10.1109/TGRS.2007.900693.

[2] Y. Kankaku, S. Suzuki, and Y. Osawa, "ALOS-2 mission and development status," *2013 IEEE Int. Geosci. Remote Sens. Symp. - IGARSS*, pp. 2396–2399, 2013, doi: 10.1109/IGARSS.2013.6723302.

[3] P. Potin, P. Bargellini, H. Laur, B. Rosich, and S. Schmuck, "Sentinel-1 mission operations concept," *2012 IEEE Int. Geosci. Remote Sens. Symp.*, pp. 1745–1748, 2012, doi: 10.1109/IGARSS.2012.6351183.

[4] A. Alonso-González *et al.*, "Joint PAZ & TanDEM-X Mission Interferometric Experiments: Interoperability and Products," *IEEE J. Sel. Top. Appl. Earth Obs. Remote Sens.*, vol. 14, pp. 6069–6082, 2021, doi: 10.1109/JSTARS.2021.3084401.

[5] K. Kellogg *et al.*, "NASA-ISRO Synthetic Aperture Radar (NISAR) Mission," in *2020 IEEE Aerospace Conference*, Big Sky, MT, USA: IEEE, Mar. 2020, pp. 1–21. doi: 10.1109/AERO47225.2020.9172638.

[6] M. W. J. Davidson and R. Furnell, "ROSE-L: Copernicus L-Band Sar Mission," in *2021 IEEE International Geoscience and Remote Sensing Symposium IGARSS*, Brussels, Belgium: IEEE, Jul. 2021, pp. 872–873. doi: 10.1109/IGARSS47720.2021.9554018.

[7] R. Horn, A. Nottensteiner, A. Reigber, J. Fischer, and R. Scheiber, "F-SAR - DLR's new multifrequency polarimetric airborne SAR," *2009 IEEE Int. Geosci. Remote Sens. Symp.*, vol. 2, pp. 902–905, 2009, doi: 10.1109/IGARSS.2009.5418244.

[8] Z. Hoppinen *et al.*, "Evaluating Snow Depth Retrievals from Sentinel-1 Volume Scattering over NASA SnowEx Sites," *EGUsphere*, pp. 1–35, 2024, doi: 10.5194/egusphere-2024-1018.

[9] J. R. Kendra, K. Sarabandi, and F. T. Ulaby, "Radar measurements of snow: experiment and analysis," *IEEE Trans. Geosci. Remote Sens.*, vol. 36, no. 3, pp. 864–879, 1998, doi: 10.1109/36.673679.

[10] M. Martone *et al.*, "The global forest/non-forest map from TanDEM-X interferometric SAR data," *Remote Sens. Environ.*, vol. 205, pp. 352–373, 2018, doi: 10.1016/j.rse.2017.12.002.

[11] D. Varade, O. Dikshit, and S. Manickam, "Dry/wet snow mapping based on the synergistic use of dual polarimetric SAR and multispectral data," *J. Mt. Sci.*, vol. 16, no. 6, pp. 1435–1451, 2019, doi: 10.1007/s11629-019-5373-3.